

# **Upgradation of Local Beach Sand Titania and Synthesis of Nanocrystalline Titania Thin Film for Solar Cell Application**

by

Oishy Roy

Student ID: 1018112019

MASTER OF SCIENCE IN MATERIALS AND METALLURGICAL  
ENGINEERING



Department of Materials and Metallurgical Engineering





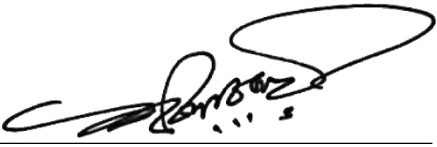
BANGLADESH UNIVERSITY OF ENGINEERING AND TECHNOLOGY (BUET)

Dhaka-1000, Bangladesh

May, 2022

The thesis titled “Upgradation of Local Beach Sand Titania and Synthesis of Nanocrystalline Titania Thin Film for Solar Cell Application” Submitted by Oishy Roy, Student ID: 1018112019 and Session: October 2018 has been accepted as satisfactory as a partial fulfilment of the requirement for the degree of M.Sc. Engg. in Materials and Metallurgical Engineering on May 17, 2022.

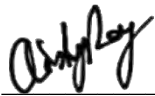
## BOARD OF EXAMINERS

1.   
Chairman  
(Supervisor)  
**Dr. Fahmida Gulshan**  
Professor  
Department of Materials and Metallurgical Engineering, BUET
2.   
Member  
(Ex-Officio)  
**Dr. Mahbub Hasan**  
Professor and Head  
Department of Materials and Metallurgical Engineering, BUET
3.   
Member  
**Dr. Kazi Mohammad Shorowordi**  
Professor  
Department of Materials and Metallurgical Engineering, BUET
4.   
Member  
**Dr. Hossain Mohammad Mamun Al Rashed**  
Associate Professor  
Department of Materials and Metallurgical Engineering, BUET
5.   
Member  
(External)  
**Dr. Muhammad Shahriar Bashar**  
Principal Scientific Officer  
Institute of Fuel Research and Development, BCSIR

## CANDIDATE'S DECLARATION

Declared that except where specified by reference to other works, the experimental studies embodied in thesis is the result of investigation carried out by the author. Neither the thesis nor any part has been submitted to or is being submitted elsewhere for any other purposes.

Signature of the student

A handwritten signature in black ink, appearing to read 'Oishy Roy', written over a horizontal line.

Oishy Roy

## ACKNOWLEDGEMENT

I would like to express my sincerest gratitude and thanks to Professor **Dr. Fahmida Gulshan**, Department of Materials and Metallurgical Engineering (MME) for her valuable suggestions and guidance from the very beginning of the thesis work. Her patience, encouragement helped me to complete this work. I am grateful for her constant support and inspiration, comments on various points of the work and the lesson about preparing and presenting the work and the book.

It is my great pleasure to express my indebtedness to **Dr. Muhammad Shahriar Bashar**, Principal Scientific Officer, Institute of Fuel Research and Development (IFRD), Bangladesh Council of Scientific and Industrial Research (BCSIR), for providing me with laboratory facilities required to conduct the thesis work. His continuous motivation and guidance kept me enthusiastic throughout the work. His valuable suggestions have raised the quality of the thesis. Sincere thanks to him for the help in carrying out the tests i.e., scanning electron microscopy, hall effect measurement, UV-Vis response of the film samples etc.

I would like to express gratefulness to **Dr. Muktadir Billah** for his sharing his knowledge and experience and for helping with conduction of UV-Vis test of powder samples.

I would like to acknowledge the cooperation of Beach Sand Minerals Exploitation Center (BSMEC), Cox's Bazar, Bangladesh for providing the sand sample of this work for free.

## ABSTRACT

In this work, investigations have been carried out to upgrade titanium dioxide from local beach sand of Cox's Bazar Bangladesh, to prepare mesoporous film using the upgraded titanium dioxide so that its potential in solar cell applications could be examined. Raw sand was collected from Beach Sand Minerals Exploitation Center in Cox's Bazar, upgraded into titanium dioxide, among which, selected samples were used to prepare mesoporous films to be used in Dye sensitized Solar Cell. Mineral and phase identification of the raw sand was performed by analyzing it via X-Ray Diffraction, X-Ray Fluorescence and Polarizing Microscopy; and the upgraded titania samples were analyzed based on the structure, composition, morphology and optical property via X-Ray Diffraction, Scanning Electron Microscopy, UV-Vis spectroscopy, respectively. The upgradation was carried out through the route of HCl leaching - H<sub>2</sub>SO<sub>4</sub> decomposition - water leaching – condensation dilution - calcination route with varying decomposition time. In this route, upgradation up to 98% TiO<sub>2</sub> was obtained though the yield was inconsistent. Modified route of HCl leaching - H<sub>2</sub>SO<sub>4</sub> decomposition - water leaching – hydrolysis - calcination resulted in consistent yield and upgradation up to 98.4% TiO<sub>2</sub> for the 900°C calcined samples and up to 87.8% for 500°C calcined samples. S, P, Si, Fe etc. were identified in the upgraded titania as impurities and the optical band gap energy was in the range of 2.99 to 3.13eV, while the carrier density was about 10<sup>12</sup>/cm<sup>3</sup>. In the later mentioned route, acid concentration of decomposition was varied and obtained titanium dioxide was used to prepare mesoporous films using screen printing method and then films were used as anode in assembled dye sensitized solar cell. Compared to the photon conversion efficiency of the solar cell prepared with commercial titanium dioxide, efficiency up to 52.3% was obtained using the films of upgraded titanium dioxide.

## TABLE OF CONTENTS

CANDIDATE'S DECLARATION.....	iii
ACKNOWLEDGEMENT .....	iv
ABSTRACT .....	v
LIST OF TABLES .....	x
LIST OF FIGURES.....	xi
1. INTRODUCTION .....	1
1.1 Background and Research Significance .....	1
1.2 Objectives of Present Study.....	3
1.3 Possible Outcome of the Study.....	3
1.4 Methodology Followed in this Work.....	3
1.5 Organization of the Thesis.....	4
2. LITERATURE REVIEW .....	6
2.1 Resources and Production of Titanium.....	6
2.2 Resources in Bangladesh .....	8
2.3 Properties of Titanium dioxide .....	9
2.4 Applications of Titanium and Titania.....	11
2.5 Traditional Methods of Titania Production .....	14
2.5.1 Chlorination process.....	14
2.5.2 Sulfate process.....	15
2.5 Pretreatment Methods of Ilmenite .....	16
2.5.1 Oxidation and reduction (redox) .....	16
2.5.2 Mechanical activation.....	17
2.5.3 Hydrothermal conversion (roasting) .....	17
2.5.4 Smelting .....	18
2.6 Leaching after Pretreatment.....	18

2.7 Commercial Processes of Synthetic Rutile Production from Ilmenite .....	19
2.7.1 Commercial processes with pyro-pretreatment: .....	19
2.7.2 Direct hydrometallurgical processes .....	22
2.8 Preparation Methods of Mesoporous TiO <sub>2</sub> Film .....	30
2.8.1 Doctor's Blade process .....	30
2.8.2 Screen printing .....	31
2.8.3 Spin coating .....	32
2.9 Calcination .....	32
2.10 Dye Sensitized Solar Cell (DSSC) .....	33
2.10.1 Components of a DSSC .....	33
2.10.2 Working principle of a DSSC .....	35
2.10.3 Factors influencing performance of a DSSC .....	36
3. EXPERIMENTAL OVERVIEW .....	37
3.1 Sample Collection .....	37
3.2 Particle Size Reduction .....	38
3.3 As received Sand Characterization .....	38
3.3.1 Particle size distribution .....	39
3.3.2 Materials composition .....	39
3.4 Upgradation of TiO <sub>2</sub> .....	39
3.4.1 Leaching with HCl solution .....	40
3.4.2 Sulfuric acid decomposition .....	42
3.4.3 Water leaching .....	42
3.4.4 Separation of titanium from solution .....	42
3.4.5 Drying and calcination .....	44
3.5 Characterization of the Upgraded TiO <sub>2</sub> Powder .....	44
3.5.1 Morphology and composition .....	45
3.5.2 Structural property .....	45

3.5.3 Optical property .....	45
3.6 Film Preparation .....	45
3.6.1 Paste preparation .....	45
3.6.2 Film preparation .....	46
3.6.3 Drying and annealing .....	46
3.7 Characterization of Film .....	46
3.7.1 Morphology .....	46
3.7.2 Thickness and uniformity of thickness .....	47
3.7.3 Optical property .....	47
3.7.4 Electrical property .....	47
3.8 Solar Cell Fabrication .....	47
3.8.1 Counter electrode preparation .....	47
3.8.2 $TiCl_4$ treatment .....	47
3.8.3 Dye solution preparation .....	48
3.8.4 Film annealing and dye absorption .....	48
3.8.5 Electrolyte preparation .....	48
3.8.6 Cell assembling .....	49
3.9 Testing photoconversion .....	49
3.10 Valorization of the Process Followed .....	50
4. RESULTS AND DISCUSSION .....	51
4.1 Introduction .....	51
4.2 Characterization of the As-received Sand (Structural and Mineralogical) .....	52
4.2.1 Particle size distribution of as-received sand .....	52
4.2.2 Morphology and mineralogy of as-received sand .....	54
4.2.3 Phase identification of as-received sand .....	56
4.2.4 Composition of as-received sand .....	58



4.2.5 Comparison of composition obtained from XRF, XRD and polarizing microscope (PM).....	60
4.3 Characterization of the upgraded <b>TiO<sub>2</sub></b> powder (Structural, optical, and morphological).....	60
4.3.1 Structural properties and composition .....	61
4.3.2 Yield.....	65
4.4 Characterization of Titania Film (Morphology, thickness, electrical, optical)..	75
4.4.1 Morphology.....	75
4.4.2 Thickness Profile .....	79
4.4.3 Hall effect Measurement.....	81
4.4.4 Optical Property .....	83
4.5 Characterization of Assembled Solar Cell.....	85
5. CONCLUSION.....	88
5.1 Findings of this Work .....	88
5.1.1 Characterization and upgradation of sand.....	88
5.1.2 Preparation of mesoporous film with upgraded and purchased anatase .....	89
5.1.3 Fabrication of dye sensitized solar cell .....	89
5.2 Scope for Further Investigation .....	89
REFERENCES.....	91

## LIST OF TABLES

Table 2-1: Reserves of individual economic minerals in total heavy mineral deposits	8
Table 2-2: Structural Characteristics of TiO <sub>2</sub>	9
Table 2-3: Literature studies about titania upgradation from ilmenite	29
Table 4-1: Size Distribution of As-received Sand and Ball milled Sand	53
Table 4-2: Relative Percentage of the minerals present in As-received sand	56
Table 4-3: Phases Identified by peak position of dried and heat-treated sand	58
Table 4-4: XRF composition of as-received sand	59
Table 4-5: Comparative analysis of sand composition	60
Table 4-6: Crystallographic data obtained from XRD plot	65
Table 4-7: Weight of upgraded titania powder after annealing and quality of precipitation	65
Table 4-8: Elemental composition of upgraded samples (varying time)	68
Table 4-9: Elemental composition of upgraded titania samples (varying acid concentrations)	71
Table 4-10 : Titania powder (annealed at 900°C) obtained through 60min decomposition time and [left] 75% H <sub>2</sub> SO <sub>4</sub> (150°C) and [right] 80% H <sub>2</sub> SO <sub>4</sub> (160°C) following Hydrolysis	72
Table 4-11: Material composition of upgraded titania powder (varying acid concentrations)	72
Table 4-12: Thickness range of screen-printed film prepared by upgraded titania powders	80
Table 4-13: Comparison of Electrical properties of sample with reference works	82
Table 4-14: Average transmittance comparison of films of upgraded (S1, S2, S3, S4, S5) and commercial titania >99.5% TiO <sub>2</sub> P21nm (C)	83
Table 4-15: Average absorbance comparison of upgraded titania films	85
Table 4-16: Experimental parameters of DSSC prepared using sample 1, 2, 3, 4, 5, commercial anatase film as photoanode and lab-prepared electrolyte, under AM 1.5 G Class AAA Solar Simulator	86
Table 4-17: Experimental parameters of DSSC prepared using sample 1, 2, 3, 4, 5, commercial anatase film as photoanode and commercial electrolyte, under AM 1.5 G Class AAA Solar Simulator	87

## LIST OF FIGURES

Figure 2-1: Structures of TiO <sub>2</sub> (a) Rutile, (b) Anatase, and (c) Brookite phases .....	10
Figure 2-2: Titania in different layers of PSC .....	13
Figure 2-3: Existing Commercial processes for upgrading ilmenite to synthetic rutile .....	19
Figure 2-4: Flowsheet of Becher Process .....	20
Figure 2-5: Hydrometallurgical processes of TiO <sub>2</sub> Extraction .....	22
Figure 2-6: Improved sulphate process .....	24
Figure 2-7: BHP Billiton developed updated process .....	25
Figure 2-8: Flowsheet of Altair process .....	27
Figure 2-9: Flowsheet of alkaline leaching .....	28
Figure 2-10: Principle of Doctor Blade Method .....	30
Figure 2-11: Screen printing process .....	31
Figure 2-12: Spin coating process .....	32
Figure 2-13: Components of a Dye-Sensitized Solar Cell .....	34
Figure 3-1: Brief Flowchart of Experimental Outline .....	37
Figure 3-2: As-Received Sand .....	38
Figure 3-3: (a) Planetary Ball Mill (b) Laboratory Test Sieve .....	39
Figure 3-4: Flowsheet of upgradation of titania from sand sample .....	40
Figure 3-5: Leaching procedure (a) weighed dried sand, (b, c) sand poured in heated liquid inside 3-neck flask with condenser, (d) after completion rapid cooling and separation through centrifuge (e) filtration .....	41
Figure 3-6: Repeated dilution and condensation to separate titanium from solution, (a) condensation (b) near end of condensation (c) dilution .....	43
Figure 3-7: (a) Hydrolysis in three neck flask (b) solution poured in beaker after hydrolysis (c) dried and calcined powder in crucible (d) titania powder prepared with varying decomposition acid concentration .....	44
Figure 3-8: Paste preparation steps (a) powder of upgraded titania, (b) binder sol preparation, (c) paste preparation by mixing with hand grinding .....	45
Figure 3-9: Flowsheet of DSSC Fabrication .....	48
Figure 3-10: Assembling DSSC (a) dye solution preparation, (b) joining two electrodes with spacer, (c) assembled DSSC .....	49
Figure 4-1: Beneficiation history of as-received sand .....	52

Figure 4-2: Size distribution of sand .....	53
Figure 4-3: Microscopic image of as-received sand (100X).....	54
Figure 4-4: Polarizing Microscopic Image of As-received sand before (a-d) and after particle size reduction (e-f).....	55
Figure 4-5: XRD plot of (a) as received sand and (b) 750°C heat treated sand.....	57
Figure 4-6: Titania powder (annealed at 900°C) obtained through varying H <sub>2</sub> SO <sub>4</sub> decomposition time (90min, 60min, 45min) during upgradation .....	61
Figure 4-7: Titania powder (annealed at 900°C) obtained through 60min decomposition time and 75% H <sub>2</sub> SO <sub>4</sub> (150°C) and 80% H <sub>2</sub> SO <sub>4</sub> (160°C) following Hydrolysis .....	62
Figure 4-8: Titania powder (annealed at 500°C) obtained through 60min-150°C decomposition condition with varying acid concentration (1. 70%, 2. 75%, 3. 80%, 4. 85%, 5. 90%) following Hydrolysis.....	63
Figure 4-9: SEM image of Titania (annealed at 900°C) extracted using HCl 80% H <sub>2</sub> SO <sub>4</sub> , 150°C for (a) 45min, (b) 60min, (c) 90min, (d) 135min.....	66
Figure 4-10: EDS patterns of samples with a. 45 min b. 60min c. 90min d. 135 min decomposition time .....	67
Figure 4-11: SEM image of powders extracted with varying decomposition H <sub>2</sub> SO <sub>4</sub> solution concentration a. 70%, b. 75%, c. 80%, d. 85%, e. 90% and annealed at 500°C after hydrolysis.....	69
Figure 4-12: EDS patterns of a. Sample 1 (70%) b. Sample 2 (75%) c. Sample 3 (80%) d. Sample 4 (85%) e. Sample 5 (90%) .....	70
Figure 4-13: UV-Vis reflectance plot of powder sample 1,2,3,4,5 for 300-850nm wavelength range.....	73
Figure 4-14: Transformed Reflectance Spectrum plot for Sample 1,2,3,4,5 using the Kubelka-Munk function .....	74
Figure 4-15: Influence of paste preparation method on film quality (Used powder sample's decomposition condition while upgrading-75%acid-150°C; hydrolysis; Method: screen printed; films annealed with 2.5°C/min) .....	76
Figure 4-16: Effect of hand grinding time on film morphology (Method: Doctor blade).....	76

Figure 4-17: Influence of film preparation method on film quality (Used powder sample's decomposition condition while upgrading-75%acid-150°C-60min; hydrolysis; hand grinding time-2h, films annealed with 2.5°C/min) .....	77
Figure 4-18: Influence of film thickness on film quality in spin coating (Used powder sample's decomposition condition while upgrading-80%acid-150°C; hydrolysis; hand grinding time-2h, films annealed with 2.5°C/min).....	77
Figure 4-19: Influence of film thickness on film quality in screen printing (Used powder sample's decomposition condition while upgrading-80%acid-150°C-60min; hydrolysis; hand grinding time-2h, films annealed with 2.5°C/min) .....	78
Figure 4-20: SEM image of Screen printed (single layered, slowly dried) and annealed films, paste prepared from powder samples 1, 2, 3, 4, 5 after 2h hand grinding .....	79
Figure 4-21: 3D mapping of screen-printed films prepared from sample 1, 2, 3, 4, 5	81
Figure 4-22: R-I curve of films from sample 1, 2, 3, 4, 5 and commercial powder....	82
Figure 4-23: %Transmittance vs wavelength plot of film sample 1,2,3,4,5 and purchased anatase (C).....	83
Figure 4-24: (a)The UV-vis absorbance vs wavelength plot. (b) absorption coefficient vs wavelength of sample 1,2,3,4,5 and commercial anatase film (C).....	84
Figure 4-25: Performance variation of assembled DSSC (a,b) with self-prepared and (c,d) commercial electrolyte.....	86

# 1. INTRODUCTION

## 1.1 Background and Research Significance

Titanium dioxide has wide varieties of applications throughout the world. Industries of paint, plastics, paper consumes about 85% of total produced pigment grade titania. Titania also has applications in cosmetics, porcelain, ceramics as welding rod coating, textiles and fabric coating, roofing granule, printing inks, floor covering, production of carbides and other chemicals, photocatalysis and photoelectrochemical device production.

Source of titania, i.e., anatase, rutile, ilmenite mineral resources in whole world sum more than 2 billion tons [1]. Our country also has reserves of titania minerals in our beach sand and sand bars of rivers among which, 1,025,000 tons of ilmenite, 97,000 tons of leucoxene and 70,000 tons of rutile have already been discovered through systemic minerals exploitation [2]. The ilmenite contains about 43%  $\text{TiO}_2$ , leucoxene has about 65%  $\text{TiO}_2$  and rutile has about 90%  $\text{TiO}_2$  in it [2]. This huge resource is not being utilized in any application, for which it needs to be upgraded into titania, so that, the name of Bangladesh can be included in the world's contribution in production of titania or metallic titanium. In this work, the upgradation of titania in the local beach sand has been conducted to investigate its potential in solar cell application.

For production of titania, industries use natural rutile, synthetic rutile, or high titanium slag as feedstock, among which, synthetic rutile and titanium slag are derived from ilmenite or other minerals through numerous upgradation routes. Upgradation of titania from minerals can be conducted by original and conventional processes named chloride and sulfate process. There are other modified, proposed or commercially followed process including the Becher sulfate process [3], Benelite process, Murso process [4], Laporte process [5], Austpac process [6], Dunn process [7], Kataoka process [8] etc. Variation of pretreatment steps [9] including roasting, smelting, decomposition, mechanical activation etc. also gave rise to many promising upgradation processes. Generally, those processes involving multiple steps of thermo reductive conversion and leaching become energy intensive and costly. But improved sulphate process, caustic leach process or other direct hydrometallurgical processes (BHP Billiton process

[10][11][12], Atlair Process [13][14], alkaline leaching [15][16]etc.) involving leaching and solvent extraction require lower energy compared to the previously mentioned thermo and electrochemical processes.

In this work, a lower energy intensive upgradation route has been followed to produce titanium dioxide from the as-received local beach sand. In this route, no energy intensive pretreatment was carried out except for the particle size reduction of ball milling. Then the ball-milled sand has been leached sequentially with hydrochloric acid, sulfuric acid, and water, followed by repeated condensation- dilution to precipitate titanium rich product to be dried and calcined into anhydrous titanium dioxide. In the modified route, after the water leaching, hydrolysis was followed instead of repeated condensing-diluting step.

Thin films of titania have been used to photocatalytically oxidize organic pollutants, bacteria, virus, and cancer cells, so that being commercially used in self-cleaning glass window, tiles, air purification system and water purification systems etc., also in gas sensing, antireflective coating, dielectric films for new generation field effect transistors.

In recent years, various deposition methods of TiO<sub>2</sub> films have been reported. Among the physical methods, DC/RF magnetron sputtering [17], Electron/ion beam evaporation, pulsed laser deposition (PLD) [18], thermal evaporation methods [19], cathode arc plasma deposition/ion-plasma sputtering [19] have been explored. The chemical methods include the chemical bath deposition (CVD), atomic layer deposition (ALD) [20][21], spray pyrolysis, anodic oxidation, spin coating, dip coating [21], solgel method [22], screen print [23][24], doctor blade [25][26] etc.

Among all these methods, screen printing method of film preparation has been used in this work to prepare mesoporous titanium dioxide films to be used as photoanode. In third generation solar cells, pure and doped titania in various morphology have been reported to be used successfully as photoanode [24][27][28][29]. Also, compact layer of titania is used in the blocking layer and scattering layer of the high efficiency solar cell [30]. Investigations about the different controlling parameters including the structure and contribution of titania in those high efficiency solar cells are numerous.

In this study, the prepared titania thin film was incorporated in the fabricated dye sensitized solar cell to find out its performance as a photoanode.

### **1.2 Objectives of Present Study**

The objective of this work is to utilize local beach sand as source of titanium dioxide and study its feasibility for solar cell application.

Thus, the specific aims of this work are

- i. Upgradation of natural rutile sand and extraction of titanium dioxide from it.
- ii. Fabrication of nanocrystalline titania thin film using this extracted titania.
- iii. Studying the suitability of the prepared thin film for solar cell application.

### **1.3 Possible Outcome of the Study**

In present study, local beach sand will be used as source of raw material for production of nanocrystalline thin film of titania and its effectiveness as photoanode in solar cell will be explored. Any positive outcome can be considered as a triumph for our renewable energy industry.

### **1.4 Methodology Followed in this Work**

The outline of the methodology is mentioned below.

- The sand sample, originally from Cox's Bazar Beach Sand was collected from Beach Sand Minerals Exploitation Center (**BSMEC**), Cox's Bazar, Bangladesh.
- The mineralogical and phase composition of the sample was determined by polarizing microscopy (**PM**), x-ray diffractometer (**XRD**) and x-ray fluorescence (**XRF**) analysis.
- The morphology and particle size distribution were studied via optical microscopy and sieve-analysis, respectively.
- Based on the characterization, suitable upgradation routes were selected for initial trials.



- Upgraded titania powder samples were analyzed with scanning electron microscopy (**SEM**) to study the morphology, electron dispersive spectrometry (**EDS**) to measure the elemental composition.
- Based on the characterization of the titania powder collected from initial trials, suitable upgradation route was selected keeping yield, consistency, and lower energy cost as primary concerns.
- The titania samples prepared with the selected upgradation route were characterized by XRF to study the composition. The morphological study was performed by SEM.
- After characterization, the trial powder powders were used to prepare mesoporous thin films using several methods. Based on the morphology and thickness of the films, studied by SEM and thickness profilometer, respectively, suitable method of film preparation was selected for final titania samples.
- The phase composition, strain on the films were studied with XRD. and elemental composition were measured via EDS.
- The optical properties of the films were studied by UV-Vis spectroscopy. Electrical properties were measured via Hall-effect measurement.
- To find the applicability of the prepared titania thin films as photo-anode, dye sensitized solar cells were prepared using laboratory prepared electrolyte and commercially available electrolyte. Films prepared with commercially available titania powder were used for the same assemble to compare.
- The light conversion efficiency of the assembled cells was measured using solar simulator.
- Based on the characterization and plausible upgradation, a suitable route of utilizing locally available sand in titania and renewable energy industry was proposed.

### **1.5 Organization of the Thesis**

The thesis is broken up into five chapters, which include, Chapter 1-Introduction, Chapter 2- Literature Review, Chapter 3- Experimental Overview, Chapter 4- Results and Discussion, Chapter 5- Conclusion, Chapter 6- Recommendation for Future Works.

In **Chapter 1**, the background and motivation of the thesis is described, along with the objective, specific aims, and probable outcome of this work. This chapter also contains the detail breakdown of the methodology approached in this thesis.

In **Chapter 2**, the relevant literature is presented in concise and informative approach. This chapter includes discussion about the resources and applications of titanium in metallic or oxide state, the conventional, commercial, and other promising upgradation processes, the mesoporous film fabrication processes, use of titania in photovoltaic device along with the mechanism, different parts and function of a dye sensitized solar cell. The reference to the existing literature is also given in this chapter.

In **Chapter 3**, the experimental detail is described in three main parts of upgradation process, film fabrication process and solar cell assemble process along with the characterization required.

In **Chapter 4**, the detailed results are presented and discussed with the possible explanations and comparison with other similar works.

In **Chapter 5**, a summary of the findings is presented. A conclusion focusing on the novelties of this work is also presented here. Some future work scopes are also recommended in this chapter.

## 2. LITERATURE REVIEW

### 2.1 Resources and Production of Titanium

As an element, titanium ranks ninth in the earth's crust (0.6%), making up 0.93% of all elements. Titanium occurs as oxides, titanates, silicotitanates, iron titanates. Ilmenite ( $\text{FeTiO}_3$ ) and rutile ( $\text{TiO}_2$ ) are the most economic minerals of titanium. Other less common, subeconomic minerals include pseudobrookite ( $\text{Fe}_2\text{TiO}_5$ ), perovskite ( $\text{CaTiO}_3$ ), titanite or sphene ( $\text{CaTiSiO}_5$ ), geikielite ( $\text{Mg, FeTiO}_3$ ), pyrophanite ( $\text{MnTiO}_3$ ) [31]. World resources of anatase, rutile, ilmenite is in total more than 2 billion tons [1].

Ilmenite is a heavy mineral with a metallic luster, crystallizes in the rhombohedral class of the hexagonal system. Its varieties include iron black, brown and red. It's opaque and magnetic. Ilmenite is composed of FeO and  $\text{TiO}_2$ , containing theoretically 52.6%  $\text{TiO}_2$ , naturally 40–65%  $\text{TiO}_2$ , depending on its geological history. Usually, ferrous iron is partially replaced by ferric iron. Individual ilmenite grains may contain microscopic rutile inclusions. Alteration of other grains may result in structure breakdown and partial leaching and oxidation of iron. This can increase ilmenite alteration products by 60% or more. Major ilmenite reserves are found in Australia, China, India, Brazil, Norway, South Africa, Canada, Mozambique, Madagascar, Ukraine, USA etc. in total 700 million metric tons worldwide, as reported in 2022 [1]. This mineral will undoubtedly remain the primary titanium resource in the future. Currently, Ilmenite supplies roughly 90% of the world's titanium mineral demand [1]. Global ilmenite production was 5.19 million metric tons in 2009, steadily increased each year, reached to 8.4 million metric tons in 2021 [1]. China, leading producer and consumer, accounts for 37% of global production of ilmenite.

Rutile is the naturally occurring most titanium rich mineral containing about 95%  $\text{TiO}_2$  with rare deposits. Titanium deposits with 30% rutile were common in the 1950s. By 1981, the rutile content had dropped to less than 1%. Due to the scarcity of natural rutile, technologies around the world have developed methods to increase the titanium content of ilmenite. The upgraded ilmenite is referred as Synthetic rutile. Natural rutile reserves are found in Australia, India, USA, South Africa, Ukraine etc. in total 49

million metric tons worldwide and the global production or recovery of around 0.63 million metric tons of rutile, reported in 2022 [1].

Leucoxene is not a true mineral. It is titanium-rich ilmenite ( $\text{Fe}_2\text{O}_3 \cdot n\text{TiO}_2$ ), finely crystalline aggregate of rutile, brookite or anatase with more than 70%  $\text{TiO}_2$ , created by weathering or alteration of ilmenite. Highly altered grains made up almost entirely of leucoxene may contain up to 80%  $\text{TiO}_2$ .

Including this natural sources and intermediate sources obtained from the natural sources, industries utilize Natural rutile, synthetic rutile, and high titanium slag as source of  $\text{TiO}_2$ .

1. **Natural rutile:** Using series of physical separation methods including gravity concentration, electrostatic separation (separate nonconducting zircon), magnetic separation (separate magnetic ilmenite), rutile concentrate having 95%  $\text{TiO}_2$  is resulted directly from beach sand.
2. **Synthetic rutile:** It is the substitute of natural rutile. Using different upgradation routes, iron and other impurities are removed from ilmenite to produce synthetic rutile which typically contains 89-92% of  $\text{TiO}_2$ .
3. **High titanium slag:** Through smelting of ilmenite in electric arc furnace to remove the iron as metallic pig iron and producing high titanium slag. It contains about 75-86%  $\text{TiO}_2$ , can be further upgraded to about 95%  $\text{TiO}_2$  through high pressure acid leaching [1][32].

As the high-grade titanium ore is scarce, most of the titanium industry rely on intermediate sources. The price of rutile, ilmenite and high titanium slag all increases every year in USA, increased in last few years due to covid situation, reached to 1500\$/metric ton of rutile, 750-790\$/metric ton of slag and 640\$/metric ton of ilmenite [1]. These mineral sources are used to produce titanium dioxide (94-95%) and metallic titanium (only 5-6%).

The global demand for titanium metal and oxide is increasing every year because of its widespread use in a variety of industries. The global demand of  $\text{TiO}_2$  was expected to grow annually at the rate of 3%. The worldwide production capacity of titania pigment was 8.4 million metric ton and that of sponge titanium was 3,50,000 metric ton [33]. World's total sponge titanium production was 2,10,000 metric ton (excluding USA)

[33]. In 2021, pigment titania costed 2,900\$ per metric ton and sponge metal costed 11,700\$ per metric ton [33].

## 2.2 Resources in Bangladesh

Systematic mineral exploitation activities conducted in the south-eastern coastal belt of Bangladesh resulted in the discovery of about 17 deposits of heavy mineral sand, totaling 4.35 million tons of heavy minerals, with an average concentration of 23% heavy minerals [2]. Zircon, rutile, ilmenite, garnet, kyanite, leucoxene, magnetite, and monazite etc. are the economically important ones, with a total weight of 1.76 million tons [2]. The average weight percentage of those economic minerals in the heavy fraction is 4.20% for zircon, 2.04% for rutile, 26.03% for ilmenite, 6.45% for garnet, 3.92% for kyanite, 2.30% for leucoxene, 1.87% for magnetite, and 0.31% for monazite; and 53.88% for other non-economic heavy minerals [2]. Approximate reserves of the minerals are shown in Table 2.1.

**Table 2-1:** Reserves of individual economic minerals in total heavy mineral deposits [2]

Mineral	Weight in tons
Ilmenite (43% $TiO_2$ )	1,025,000
Leucoxene	97,000
Rutile (90% $TiO_2$ )	70,000
Garnet	223,000
Zircon	1,58,000
Kyanite	91,000
Magnetite	81,000
Monazite	17,000

Presence of economically valuable heavy minerals has been identified in the sand bars of the Brahmaputra-Jamuna River too, overall containing around 8.92% heavy mineral [2]. Mineral sand processing on bulk samples was conducted at a pilot plant equipped with gravity, magnetic, and electrostatic separators to characterize the separation characteristics of individual economically viable mineral sands.

### 2.3 Properties of Titanium dioxide

The structural and optical characteristics of the three commonly recognized crystalline phases of titania (i.e., Rutile, Anatase and Brookite) is tabulated in Table 2.2 and the crystal structure and the building blocks of these phases are shown in Figure 2.1 using Ball-Stick Model and Polyhedron Model. The  $\text{TiO}_6$  octahedron building block of anatase is more distorted than of rutile.

**Table 2-2: Structural Characteristics of  $\text{TiO}_2$  [34][35]**

	Rutile- ICSD #9161	Anatase- COD#9008213	Brookite- ICSD #15409
Crystal System	Tetragonal	Tetragonal	Orthorhombic
Space Group	$P4_2/mnm$	$I4_1/amd$	$Pbca$
group #	136	141	61
$\alpha, \beta, \gamma$	$\alpha=\beta=\gamma=90^\circ$	$\alpha=\beta=\gamma=90^\circ$	$\alpha=\beta=\gamma=90^\circ$
a, b, c	a=b= 4.5941 c= 2.9589	a=b= 3.7842 c= 9.5146	a= 9.184 b= 5.447 c= 5.145
Volume ( $\text{nm}^3$ ) per polyhedron	0.03112	0.03402	0.0322
Density( $\text{g}/\text{cm}^3$ )	4.248	3.895	4.123
Polyhedron type	octahedron	octahedron	octahedron
Polyhedral per unit cell	2	4	8
Edge sharing per polyhedron	2	4	3
Coordination No of Ti	6	6	6
lattice energy (kJ/mol) -relative to rutile	0	24.75	18.53
Band Gap Energy (eV)	3	3.2	3.26

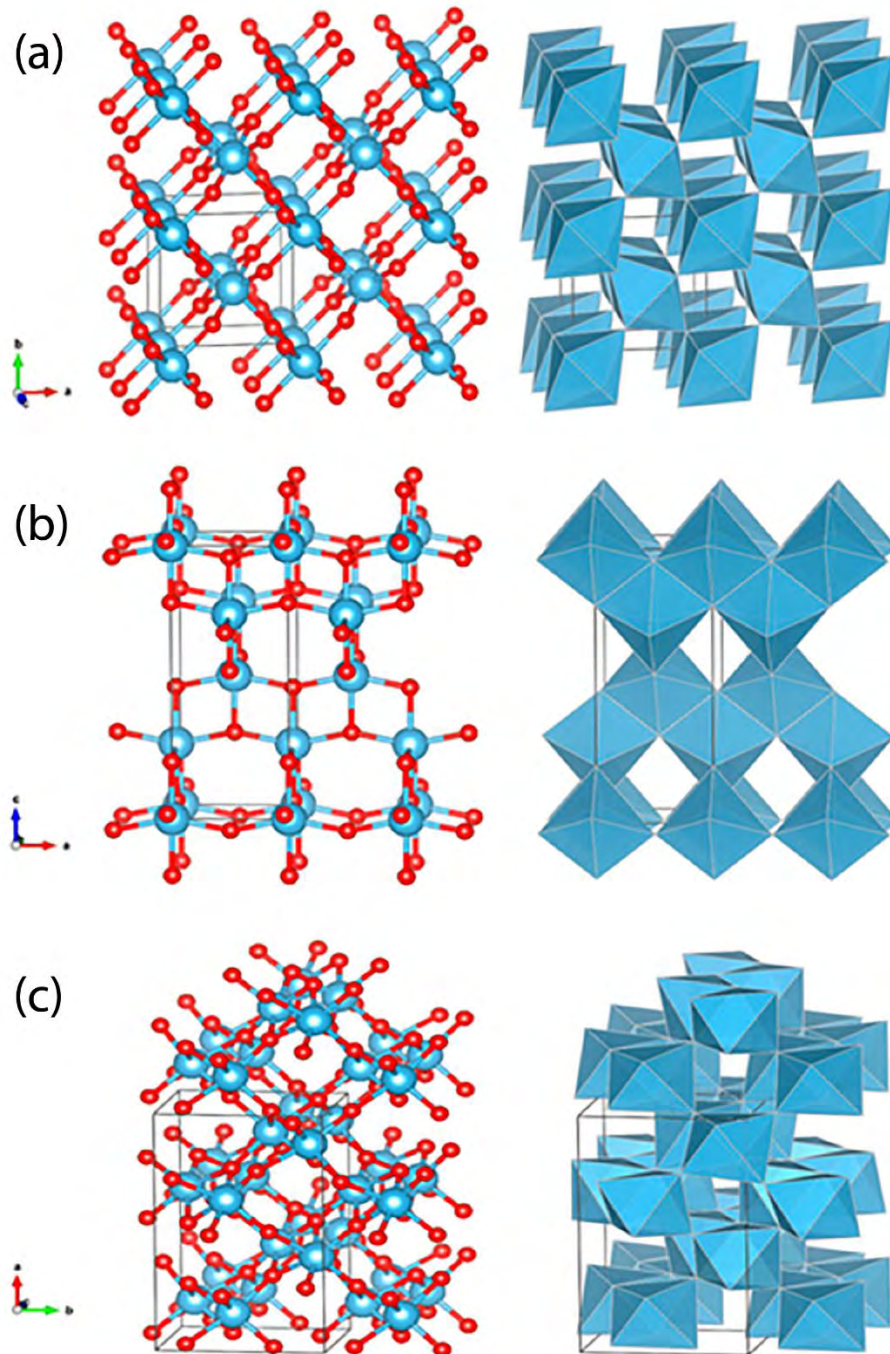


**Figure 2-1:** Structures of  $\text{TiO}_2$  (a) Rutile, (b) Anatase, and (c) Brookite phases [34]

For phase identification of polycrystalline titania, powder XRD is used. For mixed phase titania, Full profile Rietveld [36] analyses is used.

Pure titania is a wide band gap semiconductor which shows high absorbance in UV range ( $<400\text{nm}$ ) while no significant response in visible range of light.

The nonstoichiometric composition of titania containing excess titanium, acts as n type semiconductor. For which, titania treated in low oxygen pressure or hydrogen environment shows higher carrier concentration and mobility in Hall effect measurement [37].

## 2.4 Applications of Titanium and Titania

**Metallic titanium:** The commercially pure porous or sponge titanium metal, ferrotitanium and scrap are the intermediate feedstock for other industries producing ingot, slab, billet, pipe, tube, plate, rod, bar, sheet, strip, and wires of titanium alloys and steel. Because of the high strength to weight ratio and corrosion resistance in chloride environment, high temperature resistance titanium alloy makes its way in numerous industries, of which 80% is consumed by the aerospace industry. Supported by an increase of 25% in commercial aircraft orders in 2017 over 2016, the demand for titanium in the commercial aerospace industry was predicted to expand through 2020 [38]. Chemical processing, power generation, construction of water desalination, biomaterials or implants, consumer goods, marine, oil and gas, pulp, and paper, and specialty chemical industries are other applications of titanium, demands expanding from 27,000 tons at year-end 2017 to 32,500 tons by 2021 [38]. Titanium is utilized in the steel industry for deoxidation, grain size management, and carbon and nitrogen content control and stability. Interstitial free stainless steel and high-strength low-alloy steels are all titanium-intensive steels.

The application of titanium dioxide is determined by its purity, phase, particle size etc.

**Pigment:** High refractive index, greater opacity or hiding power makes  $\text{TiO}_2$  the most used pigment. Excellent chemical inertness, thermal stability and resistance to ultraviolet degradation are also the positive features of titania pigment. 85% of the produced pigments are used in paints (60%), papers (5%), plastics (20%); and the 15% is distributed in applications of printing inks, rubber, floor covering, ceramics, porcelain, textile and fabric coating, roofing granule, food, cosmetics, pharmaceuticals, other chemical industry [33]. Based on the crystal structure, the pigment titanium dioxide can be either anatase or rutile. In sunlight exposure, rutile pigment is more inert with the binders of paint compared to the anatase pigment, for which it is commonly



used in outdoor paints. Anatase pigment has application in interior paints and paper making because of its softness and bluer tone. Variation in the manufacturing and finishing process influences the quality of pigments, i.e., dispersion, durability, opacity, tinting etc.

The pigment industry grew rapidly in the early 1900's. The  $\text{TiO}_2$  pigment production worldwide is valued at over 10 billion US dollar per year [39] the global market value of its product was anticipated to be 17.12 billion US\$ by 2020 [35]. Global use of  $\text{TiO}_2$  pigments is expected to grow at a 4.1% yearly rate [38]. Global capacity for producing  $\text{TiO}_2$  pigments is predicted to rise in response to increased demand. By 2021, the capacity of chloride-process versus sulfate-process  $\text{TiO}_2$  pigments were predicted to equalize, owing primarily to the growth of chloride-process capacity in China.

**Titania Nanoparticles:** High purity titania nanoparticles, in form of powder, crystals, thin films, nanotubes, nanorods, are being utilized by researchers focusing on high-tech applications. Titania nanoparticle is used in uv-absorbing sunscreen, photocatalysis, solar cells, lithium-ion batteries, sensors, super capacitors, cancer treatment etc.

**Nanoparticles as Photocatalyst:** The creation of electron-hole pairs in semiconductor photocatalysis is triggered by the stimulation of the semiconductor particle's band gap. Selected photocatalytic transformations, such as air purification, water disinfection, and hazardous waste remediation, appear to be viable applications for this technology [40]. In the form of nanoparticles,  $\text{TiO}_2$  is far more effective as a photocatalyst than in bulk powder [41]. Below 10nm crystallite diameter size of semiconductor particles, quantum mechanical behavior [28] of each charge carrier is introduced. Decreasing particle size in nano range results in increase of band gap energy [42], blue shift of absorption edge, increase in the redox potential of photoexcited carriers [43] resulting in higher photoactivity than macrocrystalline particles. Because of the self-cleaning capacity  $\text{TiO}_2$  and  $\text{TiO}_2 - \text{SiO}_2$  photocatalyst film has application in self-cleaning devices and photoinduced hydrophilic coating [44][45]. The coating chemically breaks down the organic particles adsorbed on surface in presence of light energy corresponding to its band gap energy. Increase of hydrophobicity allows easy wash of dirt.  $\text{TiO}_2$  coating can also degrade gaseous nitrogen oxide pollutants ( $\text{NO}$ ,  $\text{NO}_x$ ). The photocatalytic and antibacterial property of  $\text{TiO}_2$  allows it to use as coating in silicone catheter [46].

The photocatalytic property of  $\text{TiO}_2$  can be utilized in mineralization and degradation of organic pollutants (i.e., aliphatics, aromatics, polymers, textile dyes, surfactants, pesticides and herbicides to  $\text{CO}_2$ , water and mineral acids ) in wastewater [42][47][48] and the degradation of pesticides (i.e., herbicides, insecticides, and fungicides) [49][50][51].

$\text{TiO}_2$  electrode has been successfully used in the production of hydrogen fuel through water splitting [52][53].  $\text{TiO}_2$  anode irradiated with near UV-light, results in flow of photocurrent through external circuit to counter electrode Pt while evolution of  $\text{H}_2$  in Pt electrode and oxygen in  $\text{TiO}_2$  electrode [54].

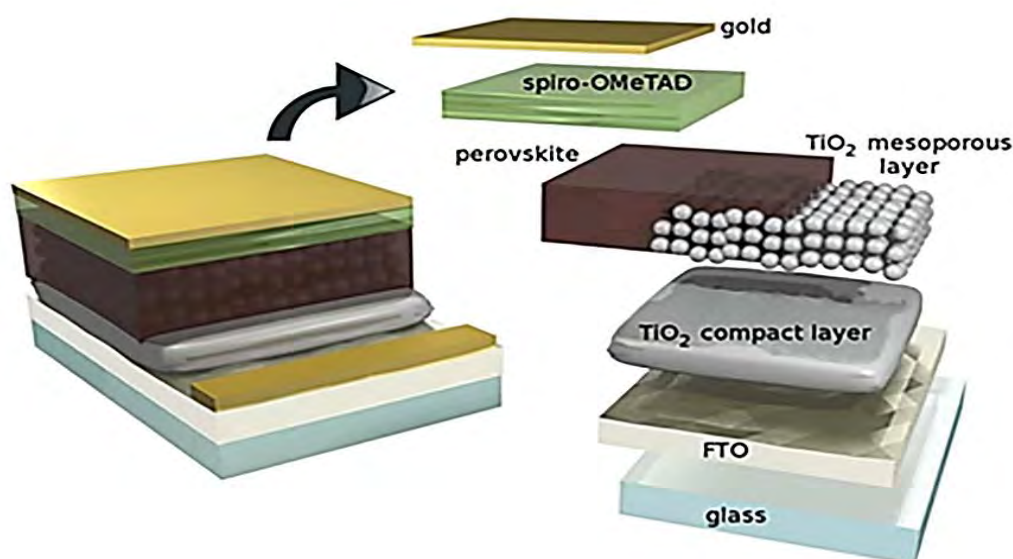


**Figure 2-2:** Titania in different layers of PSC (collected from [61])

**Nanoparticles in Solar Cell:** In third generation solar cell devices, titania and modified titania of varying morphology, structure, purity, composition can be used in different layers to serve different functions. Pure or doped anatase or mixed rutile-anatase titania is used in the mesoporous photoanode layer of the solar cell (dye-sensitized solar cell, perovskite solar cell) [55][56]. The high and indirect band gap energy of this semiconducting metal oxide makes it a strong and well-studied candidate for photoanode. Investigations about the different controlling parameters including the structure and contribution of titania in those high efficiency solar cells are numerous. Film of  $\text{TiO}_2$  is also used in the blocking layer, light scattering layer (Figure 2.2). The composition, morphology, physical and surface properties of the film serving as the

photoanode layer [57][58] in the Dye Sensitized Solar Cell (DSSC) [59] and Perovskite Solar Cell (PSC) [60] influence the light harvesting and photoconversion efficiency (PCE) of the device.

**Nanoparticles in Lithium Ion Battery:** The capacity and lifespan of lithium-ion battery is increased using carbon modified titania nanoparticles as anode [62].

## 2.5 Traditional Methods of Titania Production

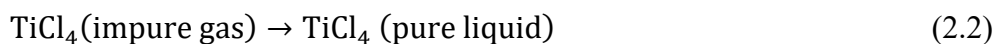
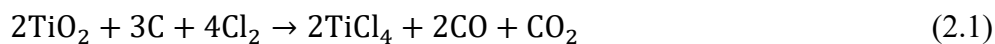
Among the two principal minerals of titanium, ilmenite is the most abundant one but contains lower amount of titania, while rutile, though has highest titania content, is less abundant. Ilmenite is used to produce synthetic rutile or titanium slag through numerous processes, nearly all are based on either selective leaching or thermal reduction of iron and other impurities present in it. Rutile, synthetic rutile, and titanium slag can be used to produce high purity titania through one of the traditional processes named chlorination process, which accounts for 60% of total titania production. Another one is the sulfate process, accounts for nearly 40% of total production. These two processes use different chemistry and raw materials [63]. Selection of one among those process is determined by the factors of raw materials availability, freight cost, weight disposal cost etc.

### 2.5.1 Chlorination process

Ore or materials containing 90-95%  $\text{TiO}_2$  are required to make this process economic. Such include the natural rutile, synthetic rutile, chloride-grade ilmenite, or titanium slag. In presence of petroleum coke and chlorine gas, the raw materials are heated at 900-1000°C in fluidized bed reactor. The product includes vapor of titanium tetrachloride (2.1), oxides of carbon, some other metal chlorides along with some non-reacting impurities. The impure gas is purified to liquid via condensation (2.2) and chemical treatment and then oxidized in a plasma arc furnace or a toluene-fired furnace above 1500°C. Aqueous hydrolysis (2.3), chemical surface treatments (with alumina, organic compounds or silica to improve functional behavior), milling (to control particle size distribution), coating and drying are followed [38]. While, in dry chlorination, the  $\text{TiCl}_4$  (2.1) is oxidized at about 1000°C to form  $\text{TiO}_2$ , which is calcined

to remove residual chlorine or hydrochloric acid forming during reaction. During the oxidation  $\text{AlCl}_3$  is added to prevent formation of anatase titania, rather forming rutile.

The reactions are [63]:

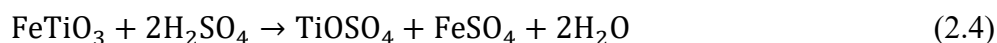


The requirement of high energy and temperature, high set-up cost, inability to process low-grade ore, high product quality, environmentally safer waste disposal path etc. are the characteristics of this process. Significant consumption of chlorine gas and energy makes this process unsuitable for low-grade ore. Ore rich in iron also requires more chlorine gas as it produces ferric chloride and hydrogen chloride as byproduct. Among the waste of unreacted coke, ore solids and metal chlorides, iron chloride is neutralized with lime or limestone and disposed [63] as it is not safe for environment.

### 2.5.2 Sulfate process

This process can utilize ilmenite (40-60%  $\text{TiO}_2$ ) or titanium slag (72-85%  $\text{TiO}_2$ ) as feedstock. Using concentrated sulfuric acid, the raw materials are digested at 150-180°C, titanium and iron get dissolved in liquor of sulfuric acid as titanyl sulfate and iron sulfate, respectively (2.4). In ilmenite-based feedstock, to ensure dissolution of all iron by converting ferric to ferrous ion (2.5), scrap metallic iron is added. Otherwise, the ferric iron would coprecipitate with  $\text{TiO}_2$  and contaminate it. Through cooling, formed ferrous sulfate is precipitated (2.6) as  $\text{FeSO}_4 \cdot 7\text{H}_2\text{O}$  along with negligible precipitation of titanyl sulphate (2.7). Through hydrolysis of the solution, precipitation (2.8) of hydrated titanium dioxide results, which is separated, dried and calcined (2.9) to bring out final product of anhydrous titanium dioxide (usually anatase), used after milled or chemical treatment.

The reactions are [31]:



Simple technology, lower energy requirement, lower grade-cheaper raw materials are the characteristics of this traditional process. But lower quality products and large amount of waste iron sulphate are the negative sides [63].

## 2.5 Pretreatment Methods of Ilmenite

As ilmenite is a lower grade titanium dioxide ore, before leaching or chlorination process, it must be upgraded using various pretreatment methods to meet the requirement of chlorination process or to either improve product quality or reduce overall cost. Oxidation and reduction, mechanical activation and hydrothermal conversion are among them [9].

### 2.5.1 Oxidation and reduction (redox)

One reported method is the carbothermic reduction at 750-1250°C of ilmenite to produce titanium dioxide and elemental iron followed by iron removal by leaching [64]. Another alternative is the vacuum carbothermic reduction followed by chlorination [65]. Other option is to pre-oxidize the ilmenite at 900-950°C for 1h, followed by its reduction at high temperature and leaching [64]. Oxidation at 600-700°C changes iron from ferrous ilmenite to ferric hematite (higher solubility in HCl) while oxidation at 900-1000°C forms pseudo-brookite (less soluble in HCl) [66]. Partial oxidation of ilmenite is caused by the pre-oxidation step [66] which increases the reactivity and reduction rate of the subsequent reduction step [64]. Also, formation of microcracks

[67] and micro holes during reduction helps enhanced penetration of leachant in the ore. This pretreatment increases the leaching rate of iron by converting it in more soluble phase [66] while decreases the leaching of titanium in HCl solution during leaching [68].

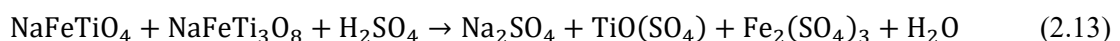
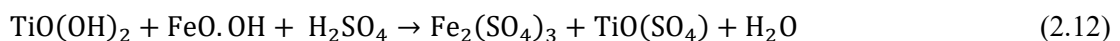
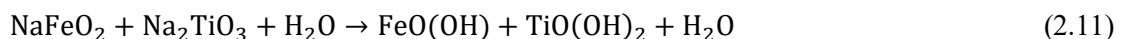
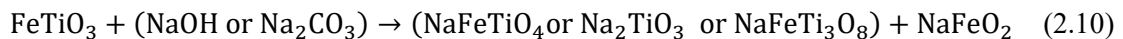
### 2.5.2 Mechanical activation

Milling activates the ore material mechanically resulting in increased subsequent leaching efficiency. Increased specific surface area, grain refinement [69][70], accumulation of lattice strain [70] and increase in lattice disorder [71][72], chemical reactions [69][73][74] or structural changes [75] can act behind the accelerated iron dissolution and titanium hydrolysis in HCl leachant. There are conflicting reports [69][70][73][75] about phase change during energetic milling. Milling time is optimized to maximize leaching efficiency and minimize solid-liquid separation problem [72].

### 2.5.3 Hydrothermal conversion (roasting)

To separate the iron and titanium in ilmenite, it can be decomposed using alkaline or acidic solution. NaOH, Na<sub>2</sub>O<sub>3</sub>, (NH<sub>4</sub>)<sub>2</sub>SO<sub>4</sub> are used as reagent.

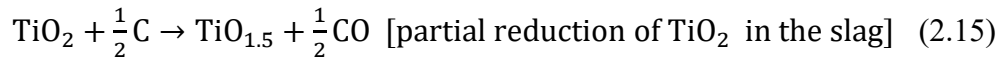
Roasting with (<70%) NaOH or Na<sub>2</sub>O<sub>3</sub> (2.10) [74] requires 550-850°C for 1-2 hours followed by water leaching (2.11) and then acid leaching (2.12-2.13).



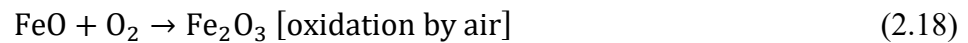
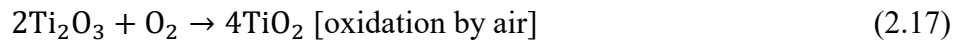
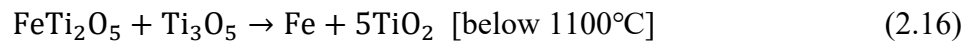
Roasting with (NH<sub>4</sub>)<sub>2</sub>SO<sub>4</sub> requires 360-500°C temperature followed by two step leaching with water and acid [76].

### 2.5.4 Smelting

Using electric arc furnace, ilmenite is heated to about 1650°C to produce a molten mixture of  $Ti_3O_5$ ,  $FeTi_2O_5$ ,  $MnTi_2O_5$ ,  $Al_2Ti_2O_5$ ,  $MgTi_2O_5$ ,  $V_2TiO_5$ ,  $Cr_2TiO_5$  [77]. Two basic reactions occur during smelting.



Reaction (2.14) proceeds further to right than (2.15). Solidified slag has pseudobrookite- $M_3O_5$  mixed phase. With reduction of temperature, the solidified slag undergoes further reaction and decompose by disproportionation (2.16) or oxidation (2.17-2.18)reaction [77].



Depending upon the oxygen supply, the composition of the solid slag at ambient temperature can vary. The final product at the ambient condition is in the  $M_6O_{11}$  form, where M indicates different metallic elements present in the ilmenite [77].

### 2.6 Leaching after Pretreatment

After the high energy pretreatments followed, the product is leached with acid or alkaline with or without subsequent water leaching to obtain the intermediate product of 90-95%  $TiO_2$  containing synthetic rutile. This product can be further treated with additional purification steps like chlorination to produce pigment grade titanium dioxide. Overall, the whole extraction process gets lengthy as it involves multiple steps and costly due to high energy requirement.

Leaching with sulfuric acid is primarily carried out after alkaline pretreatment [15][78] or mechanical activation [73][79][80].

Leaching with hydrochloric acid is carried out after redox [68] or after alkaline roasting [76][81] or mechanical activation [72].

## 2.7 Commercial Processes of Synthetic Rutile Production from Ilmenite

The commercial processes may include pyro pretreatment of ilmenite as in the Becher Process, Benelite Process, Murso Process, Laporte Process, Kataoka Process, Auspac Process, Dunn Process etc. Or it may include direct hydrometallurgical process as in the BHP Billiton Process, Altair Process etc. Those processes are summarized in Figure 2.3.

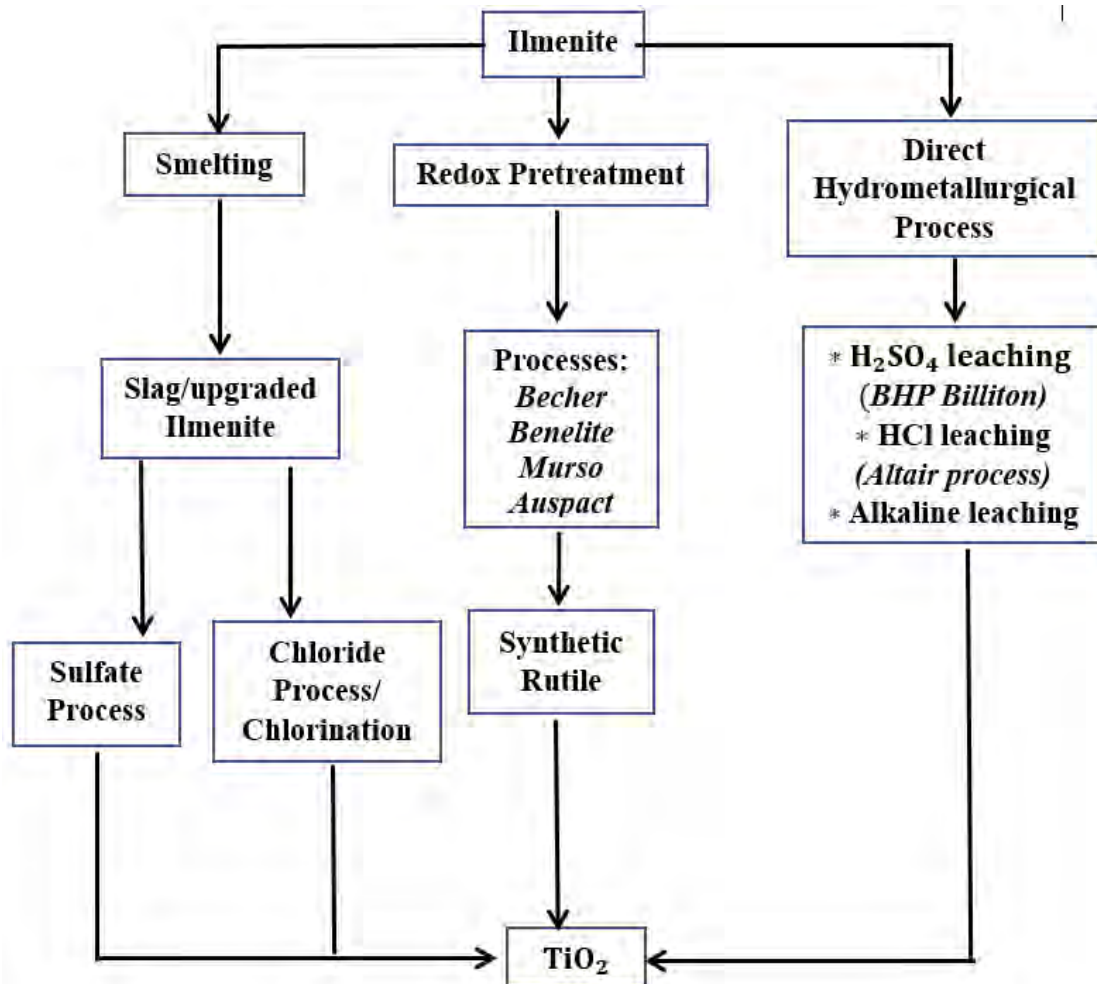


**Figure 2-3:** Existing Commercial processes for upgrading ilmenite to synthetic rutile

### 2.7.1 Commercial processes with pyro-pretreatment:

**2.7.1.1 Becher process:** As shown in Figure 2.4, the ilmenite (40-65% TiO<sub>2</sub>) goes through a series of oxidation, reduction, aeration, acid leaching steps. In oxidation, ilmenite is heated with air in rotary kiln to convert iron to iron oxides (2.19). The formed pseudobrookite (Fe<sub>2</sub>O<sub>3</sub>·TiO<sub>2</sub>) is then reduced (2.20) in presence of coal and sulfur at



1200°C to produce metallic iron. The aeration or rusting with 1% NH<sub>4</sub>Cl solution at 80°C oxidizes the metallic iron and separates it as slime (2.21). Then leaching with 0.5M H<sub>2</sub>SO<sub>4</sub> is performed to remove residual iron oxide. Diverse type of ilmenite is allowed as feed in this process but high energy consumption and CO<sub>2</sub> emission are the negative sides [3]. Also, this process is more suitable for beach sand ilmenite with low content of Ca and Mg [82].

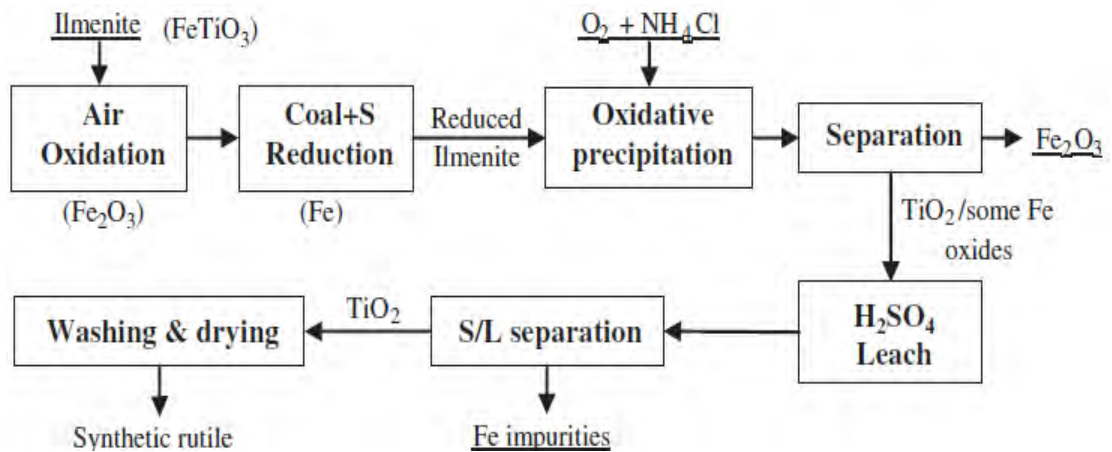
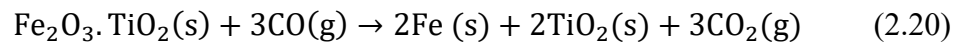
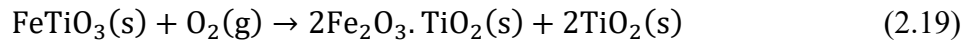


Figure 2-4: Flowsheet of Becher Process [1]

**2.7.1.2 Benelite process:** The iron other than ferrous state is converted to ferrous state by carbon thermo reduction and then separated by leaching with 18-20% HCl [31]. Though it involves one step, but the ilmenite type is limited for this process.

**2.7.1.3 Murso process:** In this process [4], Ilmenite is oxidized in fluidized bed at 900-950°C, which is then reduced in a separate fluidized bed in presence of H<sub>2</sub> gas or other reducing agent. Then the product is leached with 20% HCl at 108-110°C. After magnetic separation of the solid synthetic rutile from the leach solution, the leftover

HCl acid is regenerated. This process offers higher efficiency than Becher process for fluidized bed and HCl regeneration [31].

**2.7.1.4 Laporte process:** Pre-oxidation of ilmenite is carried out in fluidized bed at 950°C. Then it is reductive roasted with coal at 900°C in rotary kiln. The choice of equipment, temperature, reductant, partial pressure of CO<sub>2</sub> prevents complete reduction to metallic iron. The roasted ore is leached with 18% HCl for only 3.5h with a bed contactor to prevent formation of too fine particles during leaching. This process [5] is like Becher process but uses lower temperature.

**2.7.1.5 Kataoka process:** In this process [8], iron in ilmenite is reduced to ferrous form by reduction roasting. The roasted product is leached with H<sub>2</sub>SO<sub>4</sub>, during which hydrated TiO<sub>2</sub> is added to act as seed of precipitation and to increase iron removal rate. Lower leaching temperature and acid concentration is required but produces large amounts of iron sulphate waste. Product contains >95% TiO<sub>2</sub>.

**2.7.1.6 Austpac process:** Ilmenite is roasted at 800-1000°C and magnetized at this temperature to remove gangue minerals. Then the reactive product is leached with 25w/w% HCl followed by filtering precipitate, washing, and calcining. Through last stage magnetic separation, synthetic rutile containing >97% TiO<sub>2</sub> can be yielded [6].

**2.7.1.7 Dunn process:** In this process [7], through selective chlorination in fluidized bed, iron in ilmenite is more readily chlorinated than titanium. Excess ilmenite is provided so that any chlorinated titanium forms TiO<sub>2</sub> by reacting with iron oxide. The produced iron chloride gas reacts with oxygen and forms Fe<sub>2</sub>O<sub>3</sub> and Cl<sub>2</sub> gas for recycle. Handling difficulties of corrosive Cl<sub>2</sub> gas is a negative side of this process.

### 2.7.2 Direct hydrometallurgical processes

The direct hydrometallurgical process (Figure 2.5) requires no energy intensive costly pretreatment methods. It enables production of titanium dioxide without the use of intermediate synthetic rutile. Production of both pigment grade and nanoscale titanium dioxide is possible in this process.

The hydrometallurgical process uses three possible types of lixiviants.

1. Acid leaching with strong and weak acids with or without presence of reductant
2. Alkaline leaching

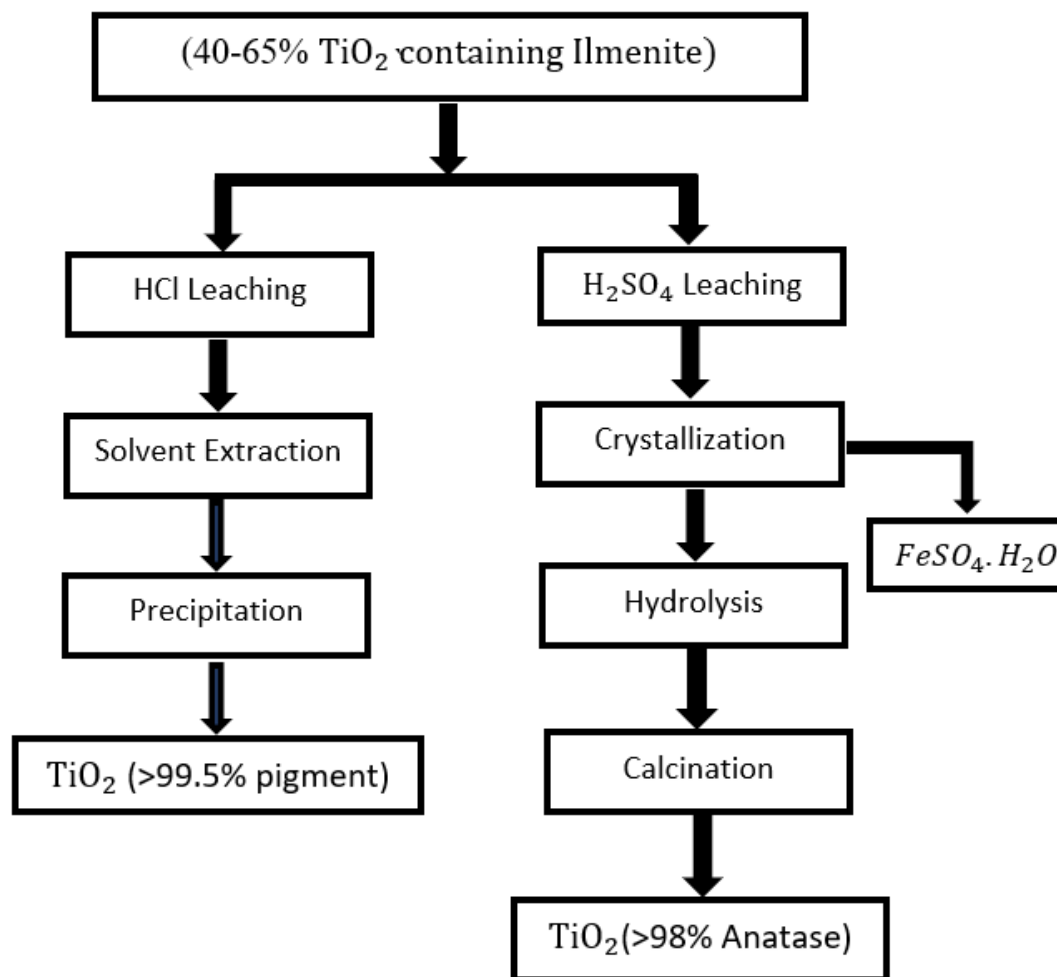
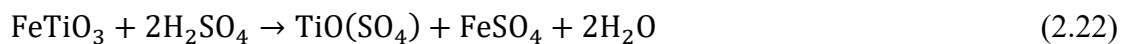


Figure 2-5: Hydrometallurgical processes of TiO<sub>2</sub> Extraction [1]

### 2.7.2.1 Sulfuric acid (strong acid) leaching

Ore leaching in sulfuric acid is primarily carried out without any prior treatment. Titanium is dissolved in solution or precipitates as a hydrolyzed product depending on the reaction temperature, reaction time, solid-liquid ratio, acid concentration and presence of additives. Those experimental conditions also influence the rate and extent of titanium or iron leaching, as well as the formation of titanium complexes. Particle size and agitation also can change reaction rate. The dissolution of titanium in sulfuric acid primarily follows (2.22) [39].



Decomposition with acid solution requires concentrated sulfuric acid and a temperature of 150-160°C [83][84] for 30-120minutes. It is followed by either cooling or water leaching, filtration, and hydrolysis. As sulfuric acid is not corrosive to equipment, this requires less expensive equipment. Sulfuric acid discharge can be reused. As the acid has lower selective leaching capability, leaching rate and impurity removal efficiency is also lower.

#### **BHP Billiton process:**

It is improved sulphate process (Figure 2.6) which is frequently improved to increase the efficiency of titania recovery. Compared to the sulphate process described in 2.3.2, this process features lots of improvement. Leaching with sulfuric acid in presence of reductive iron scrap, followed by crystallization of the ferrous sulfate from the leachate and then separation of titanyl sulfate through the solvent extraction.

Utilizing at least a portion of the raffinate from the solvent extraction phase as the leaching solution maximizes the process's effective usage of acid and regulates the iron concentration in the circuit.

Utilizing depleted leach liquor enables the reduction or removal of waste acidic effluents and/or their neutralization products such as 'brown gypsum'; it also enables heat recovery and removes energy-intensive acid recovery and evaporative

concentration procedures. Iron sulphate precipitation can be accomplished in a single stage, hence simplifying iron sulphate downstream processing.

To separate titanium from impurities such as iron, chromium, manganese, and niobium, a selective solvent extraction (SX) phase using organic systems such as tri-octyl-phosphine oxide and butyl-di-butyl-phosphonate is performed.

As a result of the solvent extraction step, the titania produced is extremely pure (99%). The addition of a reductant such as metallic iron, Ti(III) salts,  $\text{SO}_2$ , or thiosulphate allows for the use of less concentrated sulfuric acid than is necessary for the standard sulphate process.

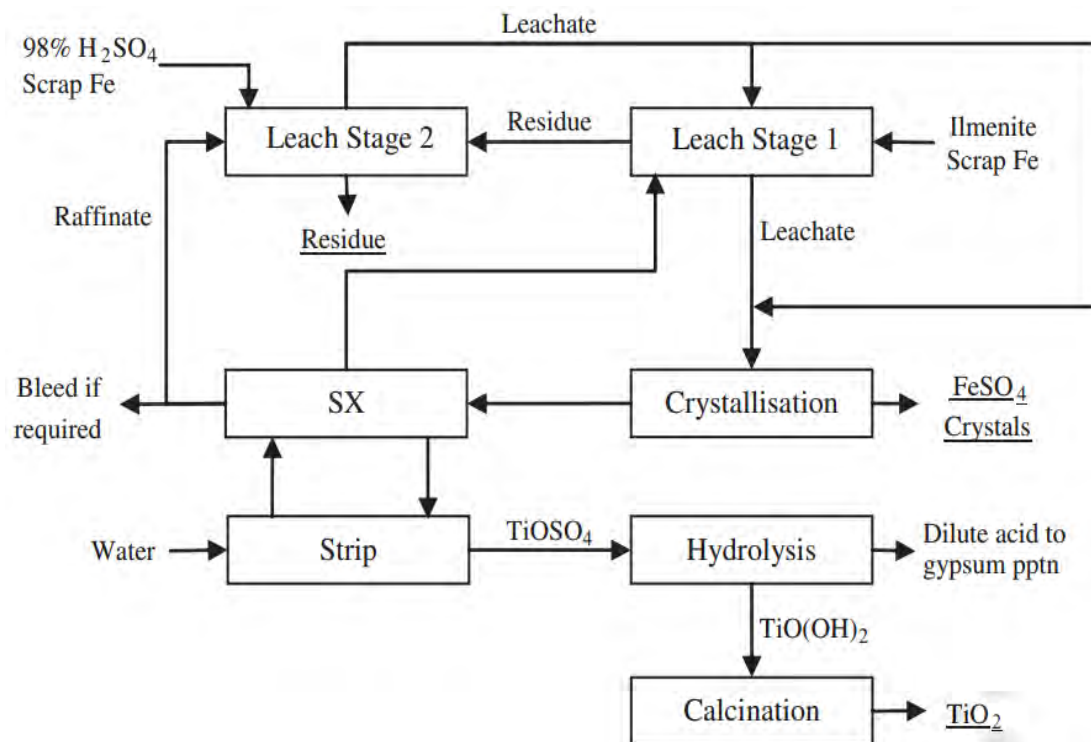


**Figure 2-6:** Improved sulphate process [10]

Instead of solvent extraction, the crystallization of titanyl sulfate step to make  $\text{TiOSO}_4$  crystals, dissolving the crystals and then hydrolyzing to make a solid phase with hydrated titanium oxides, calcination to titania was proposed further [11]. As in hydrolysis, temperature, retention time and solution concentration determine the crystal growth and fineness. Though crystallization is simpler, the product quality is lower (97%) than solvent extraction (99%). Later it was found that, titanyl sulphate

particulates can act as a seed, causing the dissolved titanyl sulphate to precipitate early during the leach step, which can negatively affect the extraction rate [12].

Later, a filtering leachant for the leach step has been introduced that removes most of the titanyl sulphate particles from the leachant before it is sent to the leach step (Figure 2.7). It was also found by the inventors that the co-precipitated ferric iron with titanyl sulphate tended to be carried over to the next steps in the process, which could harm the quality of the finished product. For this reason, reductant of scrap iron,  $Ti^{3+}$  species,  $SO_2$  gas, Zinc dust are used to ensure ferric reduction. After hydrolysis of  $TiO(OH)_2$ , a bleaching step is used to remove the chromophores from solid by reducing into their soluble forms. Mixture of  $K_2SO_4$ ,  $ZnO$ ,  $H_3PO_4$  are used as additive during calcination to control growth of rutile crystals. The product is 98-99% pure.

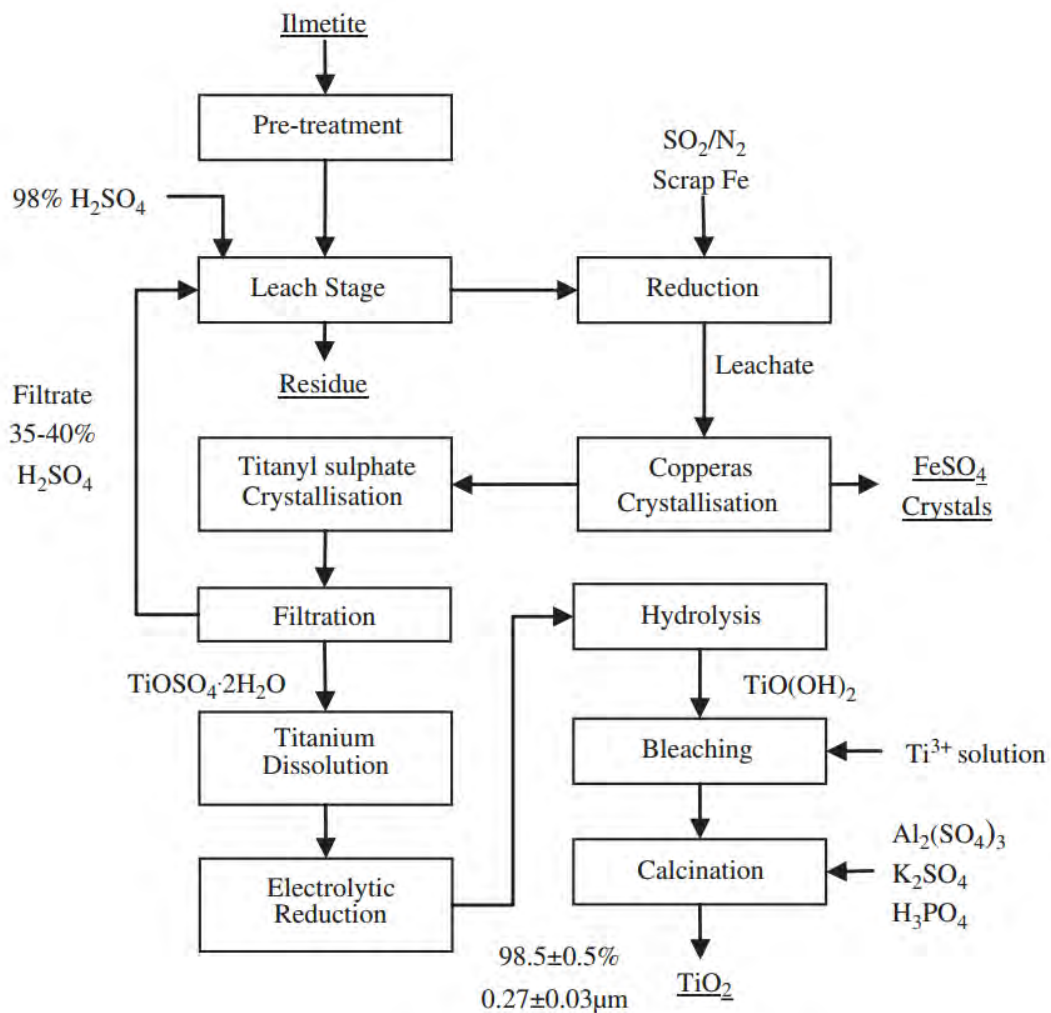
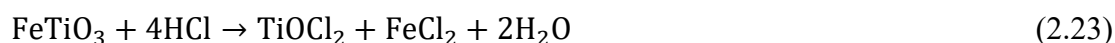


Figure 2-7: BHP Billiton developed updated process. [12]

### 2.7.2.2 Hydrochloric acid leaching

The leaching rate and extent are determined by particle size of ore [85], reaction time and temperature, acid concentration, solid-liquid ratio, and the presence of additives. Whether titanium hydrolysis, dissolution or polymerization would occur is also determined by these conditions. The concentration of  $\text{Ti}^{4+}$  and  $\text{Cl}^-$  in solution determines the species of  $\text{Ti}^{4+}$  those forms, which ultimately can be correlated with acid strength, solid-liquid ratio and other aforementioned variables [86].

The dissolution reaction of titanium in HCl acid follows (2.23) [39].



Impurity removal and selective leaching efficiency are both excellent with HCl. Used acid can be easily regenerated [87] and recycled; but it necessitates energy-intensive pyro-hydrolysis and expensive process equipment. It is also simpler to manage waste.

### Altair process

In this process (Figure 2.8), Hydrochloric acid is used to leach the ore, after separation, the leachate contains titanium and iron chloride, which is then cooled to form crystals of  $\text{FeCl}_2$ . Titanium and ferric ions are extracted combined with phosphine oxide in a first solvent extraction (SX) circuit to create raffinate containing ferrous ions and other contaminants. Then ferric ions from the loaded strip liquor of the first SX circuit is extracted with an amine extractant in the second SX circuit. The raffinate is then hydrolyzed to produce titanium dioxide. To regenerate HCl and ferric oxides, distillation or pyro-hydrolysis of the strip liquor can be followed. Or, by electrolytic reduction or reduction with metal iron scrap can be followed before crystallizing  $\text{FeCl}_2$ . Use of low-grade ilmenite, use of gaseous HCl to increase leaching rate and purity of titanium chloride solution, recovery of cleaner iron oxide, renewing and recycling gaseous HCl are the bright features of this process.

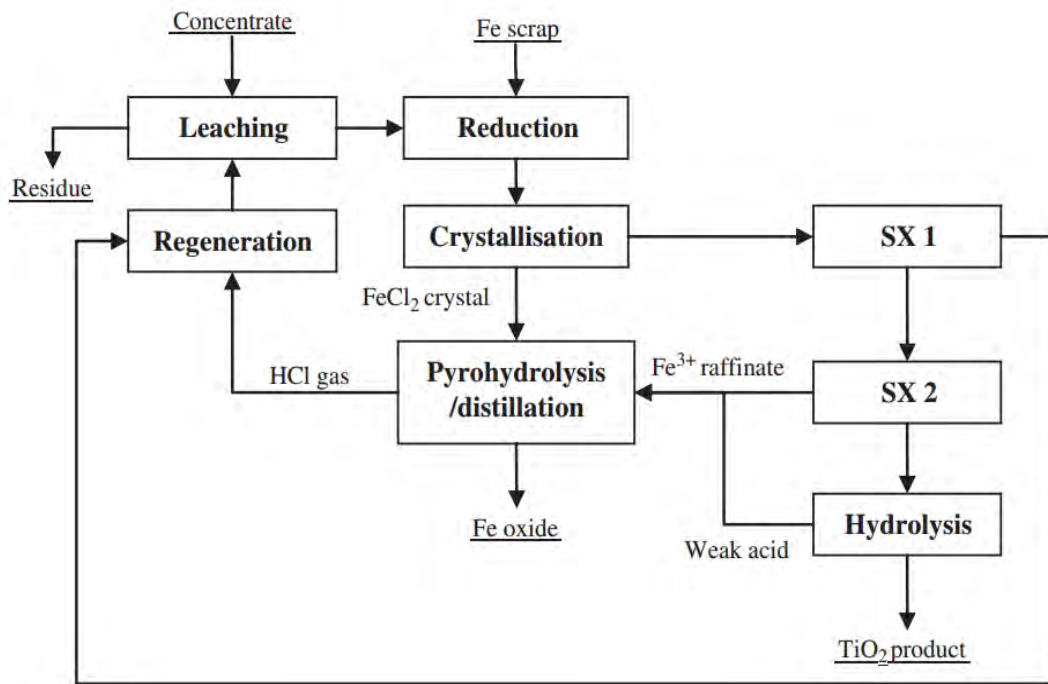
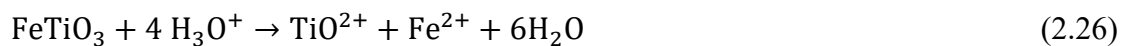


Figure 2-8: Flowsheet of Altair process [13][14]

### 2.7.2.3 Weak acid leaching

Ilmenite is leached using oxalic and citric acids too, among which, citric acid performs better in separating Ti and Fe [15][16]. The weak acids are less corrosive, showing higher selective leaching efficiency, requires lower concentration of acid. But cost of acid is higher.

The dissolution reaction of titanium follows (2.24-2.26).

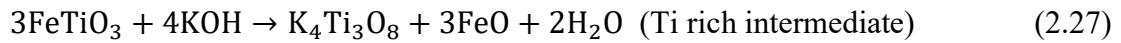


### 2.7.2.4 Caustic leaching

As shown in Figure 2.9, concentrated KOH [88] or NaOH [89] solution is used to decompose ilmenite at atmospheric pressure, yielding a titanium-rich intermediate (2.27) with low iron content, which can then be transformed into pigment-grade titanium dioxide following further processing of subsequent acid leaching (2.28).



Decomposition with 80% KOH [90] requires 180-220°C, 500-1200rpm of agitation, which results in formation of potassium titanate and iron oxide. Through hydrolyzing in acid solution of pH 2 for 1hour, potassium titanate phase transformation is occurred, and hydrous titania is obtained. Then calcination results in 99% pure TiO<sub>2</sub>. Temperature, pressure, concentration of caustic are the variables to optimize the efficiency of leaching.



Similarly, when decomposed with NaOH, sodium titanate(K<sub>4</sub>Ti<sub>3</sub>O<sub>8</sub>) is formed which is then acid leached.

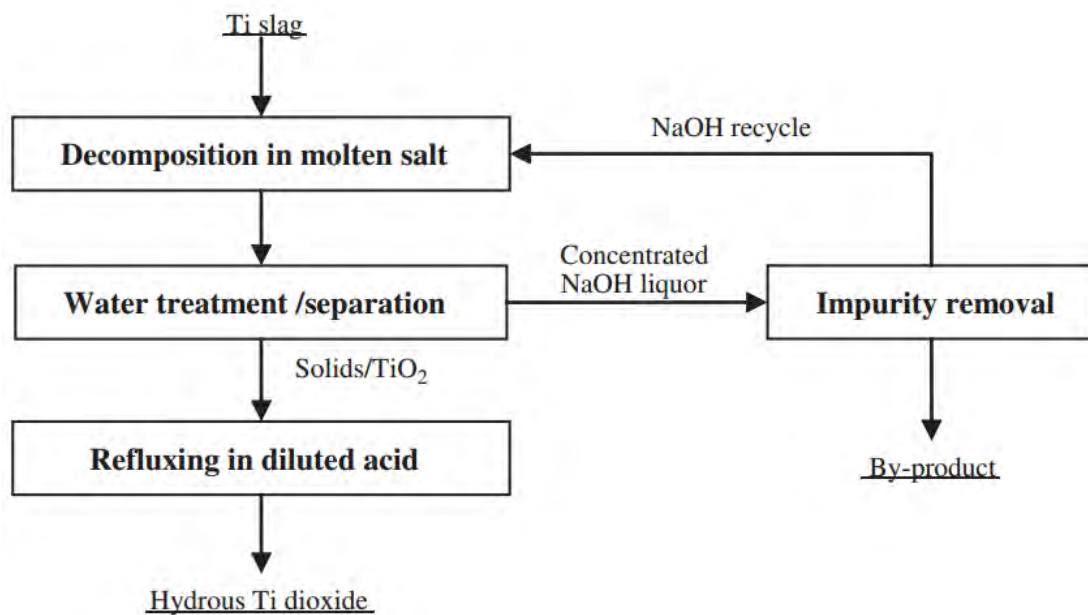


Figure 2-9: Flowsheet of alkaline leaching [1][88]

**Table 2-3:** Literature studies about titania upgradation from ilmenite

<b>Work link</b>	<b>Extraction Steps</b>	<b>% of Ti Recovery</b>
Tan et al.2011 Zhang et al. 2011 [68]	Oxidation-Reduction-Milling-HCl Leaching	90.5% (Imp: Fe, Si, Ca, Mg)
Guo et al. 2014 [81]	Roasting-HCl leaching-NaOH leaching	95.34% (Imp: Si, P, Ca, Mg)
Liu et al.2016 [76]	Roasting- Water leaching-HCl leaching- NaOH leaching	92.86% (Imp: Fe, Si, Al, Ca, Mg)
Lasheen 2008 [91]	Roasting-Water leaching-HCl leaching (Fe Reductive agent) -NaOH leaching	97% (Imp: Fe, Si, Al, Ca, Mg)
Middlemas 2013 [92]	Alkaline roasting-HCl leaching-solvent extraction-Hydrolysis	99.9% (Imp: Fe)
Wu et al 2010 [93]	Milling- HCl leaching	90.8% (Imp: Fe, Si, Al, Ca, Mg, Mn)
Li et al. 2008b [72]	Milling- HCl leaching	92.3% (Imp: Fe, Si, Al, Mn, Ca, Mg)
Mehdilo and Irannajad 2012[94]	HCl leaching	91% (Imp: Fe, Si, Ca, Mg)
Mahmoud et al. 2004 [95] Lasheen 2005 [96]	HCl leaching, Fe Reductive agent	89.45% (Imp: Fe, Si, Al, Mn, V, Cr, Ca, Mg)
Nayl and Aly 2009 [15]	KOH decomposition-Oxalic acid leaching -Hydrolysis	98% (Imp: Fe, Si, Mn)
Xiong et al. 2013 [83]	Milling-HCl leaching- H <sub>2</sub> SO <sub>4</sub> decomposition-Water leaching- Hydrolysis (EDTA)	

## 2.8 Preparation Methods of Mesoporous TiO<sub>2</sub> Film

The mesoporous TiO<sub>2</sub> thin film, which is one of the main components of the DSSC, can be prepared using a variety of ways, including doctor blade, screen print, spin coating, spray coating, physical vapor deposition, sol-gel method, and liquid phase crystal deposition (LPCD) etc. Among those, low-cost methods include the doctor blade, screen print and spin coating; that is why have been studied for fast preparation of TiO<sub>2</sub> electrodes. To ensure the maximum efficient charge storage and transfer in the titania film, the thickness must be optimum. and both the thickness and structure of the titania thin film are affected by the preparation method.

### 2.8.1 Doctor's Blade process

To prepare mesoporous titania thin film for lab-scale DSSC, Doctor Blade film preparation method (Figure 2.10) is the most used one, because of its low cost, ease of operation and lack of moving parts [97][26][25]. This method does not require operation training. Simple and flexible apparatus and cost effectiveness allows it to be adopted by the amateurs. The apparatus includes a stage, substrate, blade or tape, and a glass rod or squeeze. A clean substrate is placed on the stage or support, the substrate is placed fix on the stage by the tape on its edge. The thickness of the film is controlled by the tape near the edge, and by the distance between the substrate and blade/rod. Then the paste of TiO<sub>2</sub> nanoparticles to be deposited is placed on one of the edges and using a glass rod or moving blade pressure, the paste is spread uniformly on the bare substrate. For multiple layered film or increased thickness, the process can be repeated and lastly the film is dried.

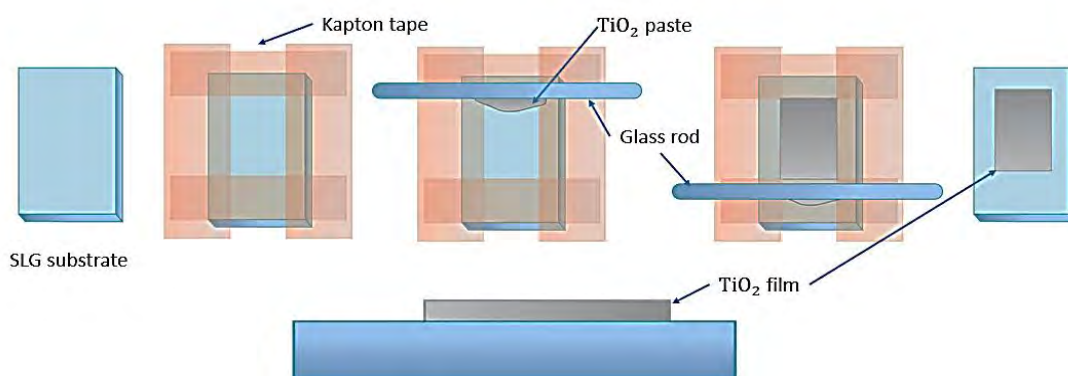


**Figure 2-10:** Principle of Doctor Blade Method

### 2.8.2 Screen printing

In this method (Figure 2.11), the paste containing the powder, solvent, dispersant, and binder is pressed onto the mesh of the screen mask to deposit a patterned layer on the flat substrate placed under the screen mask. The pressure is given either manually or automatically by the squeegee, consisting of polyurethane rubber. After the deposition, the screen mask is removed, leaving the film of paste on substrate. Thickness of film can vary from few microns to millimeter. In case of multiple printing, curing after each layer is followed. The quality of screen-printed film depends on the stability and homogeneity of paste, preventing the sedimentation and agglomeration of powder over time. The solvent is the dispersion medium for the powder and medium to dissolve other additives. It determines the drying rate, which too controls the quality of paste. The dispersant, (frequently polyethylene glycol, penta-stearic acid oligomer, alcohol poly-oxyethylene, phosphoric acid ester etc.) decreases the paste viscosity, increases the repulsion among particles of powder, improving the stability of the paste. The binders improve particle network in the film and provides strength of handling [98].

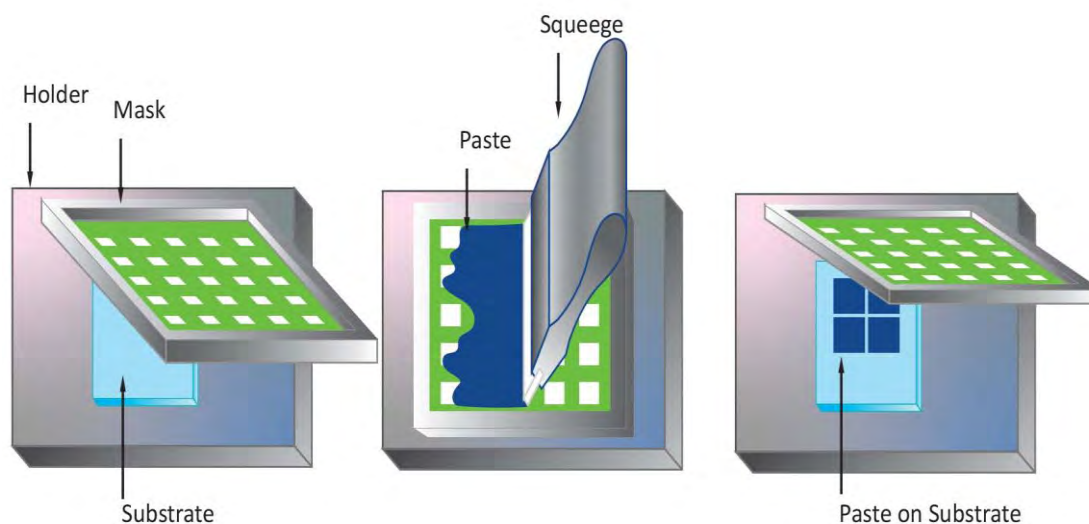


**Figure 2-11:** Screen printing process

Screen printing method has been widely used for preparation of mesoporous titania thin films used for the dye sensitized solar cell [29][99][100][24].

### 2.8.3 Spin coating

In this process (Figure 2.12), the substrate is hold on a support with vacuum. After that liquid paste is dropped on the middle of the substrate while the horizontal rotation of the support starts, which causes the liquid to spread on the substrate. Resulting in a coated film on the substrate. The rotational speed, rotation time and the viscosity, homogeneity of the paste and the drying rate of the film determines the quality and stability of the prepared film.

To prepare both the mesoporous and compact film of titania, spin coating method has been investigated [101] .



Figure 2-12: Spin coating process

### 2.9 Calcination

During calcination, the hydrated titanium dioxide powders get crystallized. Depending up on the temperature, time of calcination and purity, particle size, preparation history of the powder, presence of nuclei or additive in the powder, the calcination product varies [102]. Ideally, for temperature below 550°C, anatase titania forms while for temperature above 750°C, rutile titania forms and for intermediate temperatures, mixed phase of rutile and anatase titania forms [103]. But the previously mentioned factors

can cause the change of the rutile transformation temperature from 400-1100°C [102]. Additives of S, Si, La, P, Nb etc. act as rutile inhibitors [104], while additives of Li, Zn, Mg, Sb, K, Cu, Al, Sn, Cd facilitates rutile formation [102][104][105]. Some additives influence the crystal growth and optical characteristics also. If annealing is performed in vacuum condition, defects like oxygen vacancy and interstitial titanium is introduced in surface resulting in reduced TiO<sub>2</sub> crystals [106] .

## **2.10 Dye Sensitized Solar Cell (DSSC)**

Solar energy is the most appealing of the renewable and green energies (hydropower, solar energy, wind power, biofuel, biomass and geothermal) explored by humans so far because of its abundance and cleanliness. According to the statistics, utilizing only 0.16% of the earth's surface with solar cells with a 10% efficiency would be enough to meet the entire world's energy needs [107]. Each year, the annual market for PV devices grows [27]. Conventional silicon based solar cell requires complex manufacturing process, resulting in higher cost of cell. On the other hand, the third-generation dye sensitized solar cell has low production cost, easier fabrication process and high conversion efficiency.

### **2.10.1 Components of a DSSC**

Typically, a DSSC has four main components.

- a. The photoanode
- b. Dye/sensitizer
- c. Electrolyte
- d. Counter electrode

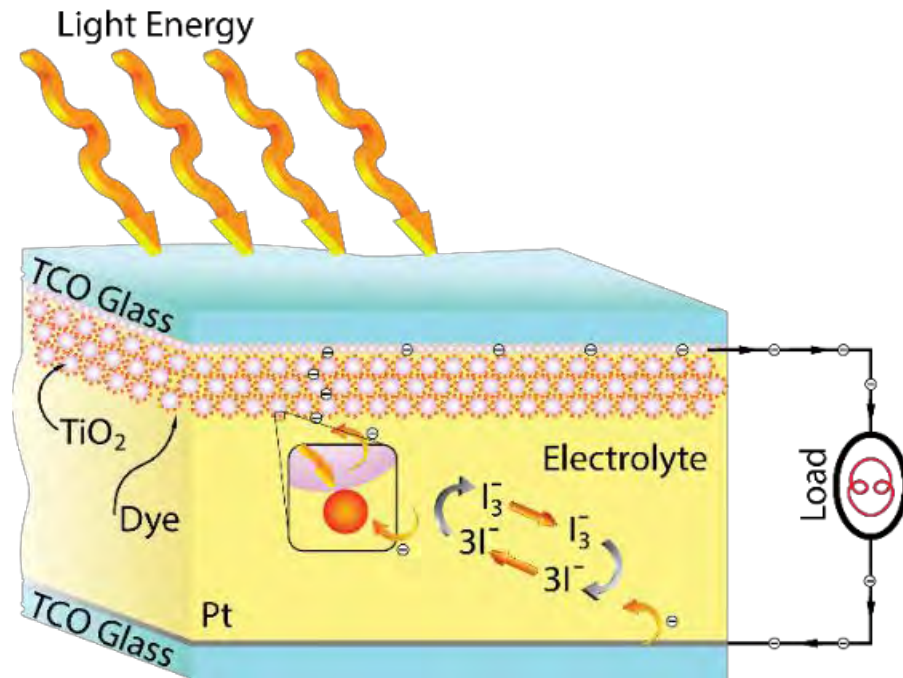


**Figure 2-13:** Components of a Dye-Sensitized Solar Cell

A substrate supports the semiconductor layer and collects current, so it must be both optically transparent and electrically conductive.

**Photoanode:** The photoanode serves two critical functions: it regulates the collection and transport of photo-excited electrons from the dye to substrate to external circuit and serves as a matrix/scaffold layer for dye adsorption. An ideal photoanode requires to have the following characteristics [59].

- large surface area for maximum possible dye loading and light absorption. Conventionally, mesoporous film is used for this purpose.
- high transparency to reduce incident photon loss
- high electron mobility to facilitate electron transport
- no reaction with electrolyte to minimize recombination rate
- contain hydroxyl group or defects for the attachment of dye molecule on its surface

As photoanode, conventional semiconductor materials (GaAs, CdS, InP, etc.) have caused reduced cell lifetime due to photodegradation. Semiconducting metal oxides of wide band gap such as titanium dioxide (TiO<sub>2</sub>) and zinc oxide (ZnO), deposited on the transparent conducting oxide (TCO) substrates have been used successfully but they

only absorb the ultraviolet part of the solar spectrum. The high chemical stability, mesoporous nature and low toxicity, higher CB edge, higher electron affinity are the reasons behind the wide use of titania as photoanode. Among its three crystalline forms, anatase shows more efficiency in solar energy conversion and photocatalysis than rutile or brookite. Because of its indirect band gap in anatase, the photoexcited electrons can't undergo direct transition from CB to VB, resulting in longer lifetime of photoelectrons. Also, the lighter average effective mass of the photoexcited electrons provides faster migration and lower recombination rate of electrons in anatase.

**Dye:** The primary function of the dye absorbed in the photoanode film is to harvest light and to generate photo-excited electrons, which are then injected into the photoanode to be transferred to the outer circuit via the TCO substrate. In DSSC, organometallic dyes based on Ruthenium, organic dyes or natural sensitizers are used as dyes.

**Electrolyte:** The electrolyte's function is to carry electronic charge between the electrodes while also regenerating the oxidized dye. Iodide-triiodide redox couple in organic solvent acetonitrile is commonly used as liquid electrolyte. The advantages include fast dye regeneration, low recombination loss and slower penetration into semiconducting oxide film, though other quasi-solid or solid electrolytes have been investigated for evaporation and leakage issues.

**Counter electrode:** Usually Pt-coated FTO glass is used as counter electrode. Pt is the catalytic layer which reduces the overpotential for redox reaction and resist the corrosion against electrolyte. Pt is deposited on FTO by sputtering, spray pyrolysis or doctor blade process.

### 2.10.2 Working principle of a DSSC

Under illumination, the excited photons from dye molecules flow through the conduction band of semiconducting metal oxide to the TCO substrate. The electrons flow through the external circuit and reach to the counter electrode. The oxidized dye gets back to its ground state by electron transfer to the redox couple present in electrolyte. This process needs to be fast so that the recombination of photoexcited



photons with oxidized dye is prevented. The oxidized redox mediators are regenerated at the counter electrode by receiving the electrons, as shown in Figure 2.13.

### 2.10.3 Factors influencing performance of a DSSC

Modification of the morphology, composition, or thickness of the photoanode film influences the photovoltaic performance of the DSSC. Significant research has been conducted to investigate the influences of photo-anode modifications on DSSC performance. The modifications can be classified into three categories [59], namely

1. interfacial modification through the introduction of blocking and scattering layer
2. doping with different external or internal species improves performance by narrowing band gap, shifting absorption edge toward visible spectrum or by altering conduction band minimum, valance band maximum or by improving conductivity and charge mobility with effective electron-hole separation. Non-metallic anions (N, B, S, F, C, I) [108] show better photoelectric properties [109] than metallic cations (Zr, Fe, Y, Zr, Nb, W, Cr, Sc, Ce, Sn, Sb, Mn, Cu, V, In, Ga, La) [110]. Also, intrinsic defects of oxygen vacancy or  $Ti^{3+}$  can be introduced by reducing in hydrogen or vacuum annealing [37][111].
3. replacing the conventional mesoporous semiconducting metal oxide films with one-dimensional or two-dimensional nanostructure.

To improve photovoltaic performance of DSSC, a blocking layer or compact layer is introduced between FTO and mesoporous  $TiO_2$  photoanode to reduce interaction of electrolyte with FTO and the mesoporous  $TiO_2$ ; so that the recombination of photo injected electron with  $I_3^-$  in electrolyte is reduced. This also improves the electronic contact at FTO- $TiO_2$  interface. Compact  $TiO_2$  film, deposited by sputtering or hydrolysis of  $TiCl_4$  aqueous solution or atomic layer deposition technique is usually used as blocking layer. An additional 'light scattering layer' above the  $TiO_2$  layer acts to increase the photoanode's optical absorption. For this layer, use of nanostructures of titania such as hollow spheres, nanorods, nanowires, nanofibers or nanotubes is frequent.

### 3. EXPERIMENTAL OVERVIEW

The overall outline of the experimental work is shown in the following Figure 3.1.

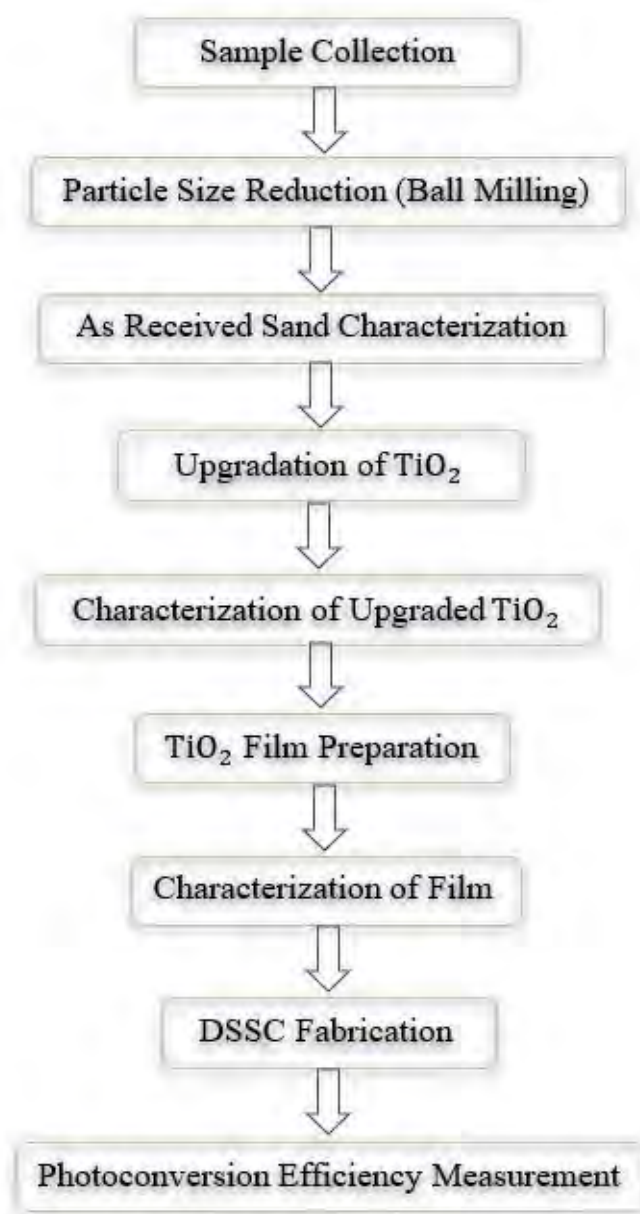


**Figure 3-1:** Brief Flowchart of Experimental Outline

#### 3.1 Sample Collection

Beach sand from Cox's Bazar was physically separated to different fractions by Beach Sand Minerals Exploitation Center (BSMEC) and the rutile concentrate "Rutile Sand" was collected from them for this work. The as received sand was black in color (Figure 3.2).



**Figure 3-2:** As-Received Sand

### **3.2 Particle Size Reduction**

Part of the as-received sand was dried at 110°C for 24 hours, and ball milled using Planetary Ball Mill (Model- Poluerisette 6, FRITSCH, Germany) for 15 minutes at 400 rpm with ball: sand mass ratio of 2:1 [Figure 3.3a]. As this size distribution resulted in reduced filterability by increasing solid-liquid separation difficulty, another batch of the as-received sand was ball milled for 5 minutes to tradeoff between reduced size distribution and efficient separation of solid liquid phase. And the 5 minutes ball-milled sand was selected for further upgradation experiments.

Part of the milled sand was heat treated at 750°C for 3hours to observe the effect of oxidation.

### **3.3 As received Sand Characterization**

The upgradation route depends on the mineral composition, chemical and physical properties of the sample, for which characterization is an important step before upgradation. In this work, the selection of upgradation route and experiments were influenced by the locally available facilities.

### 3.3.1 Particle size distribution

The particle size distribution of as-received sand, 15minutes ball milled sand and 5 minutes ball milled sand were measured in Laboratory Test Sieve (Retsch (D-42759/Germany; Mesh and frame materials- Stainless steel; Serial No-5621123; ASTM-E11) with a vibration speed of 80ram for 10minutes [Figure 3.3b]

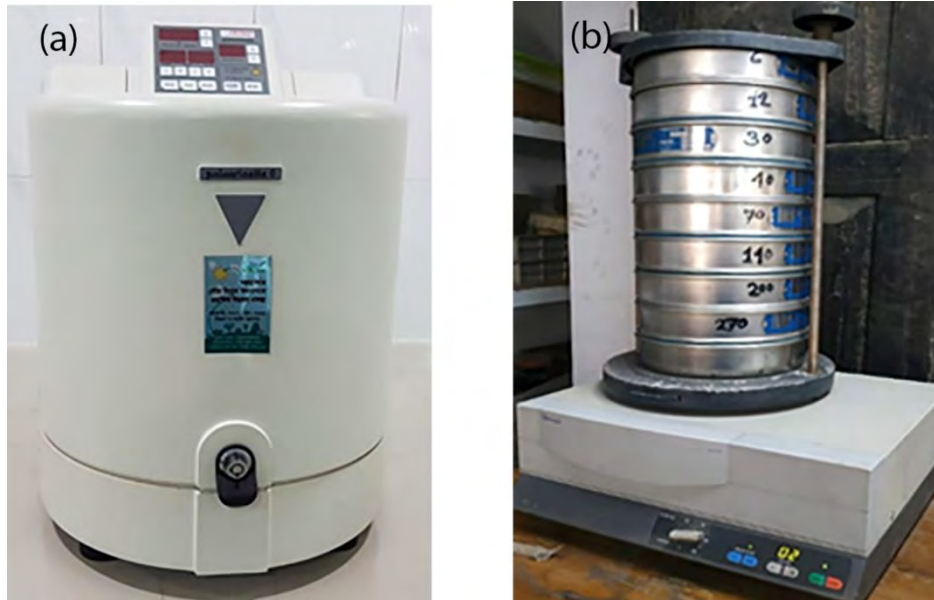


**Figure 3-3:** (a) Planetary Ball Mill (b) Laboratory Test Sieve

### 3.3.2 Materials composition

- The characterization began with the bulk chemical analysis of the sample by XRF (Model: Lab Center XRF- 1800, SHIMADZU). The concentration of desired and major impurities can be measured accurately using XRF.
- Then to detect the minerals and measure their probable quantity, PM (Model-LEICA-ICC50E, Germany) images of the as-received sand were studied.
- To identify the crystalline phases, present in the as-received sand and heat-treated sand, it was characterized with XRD (Rigaku, Smart Lab) and the resultant data was fitted using Rietveld fitting (X'pert High Score Plus Software) to measure the percentage of phases.

### 3.4 Upgradation of $\text{TiO}_2$

The overall upgradation experiment is shown in following flowchart (Figure 3.4).

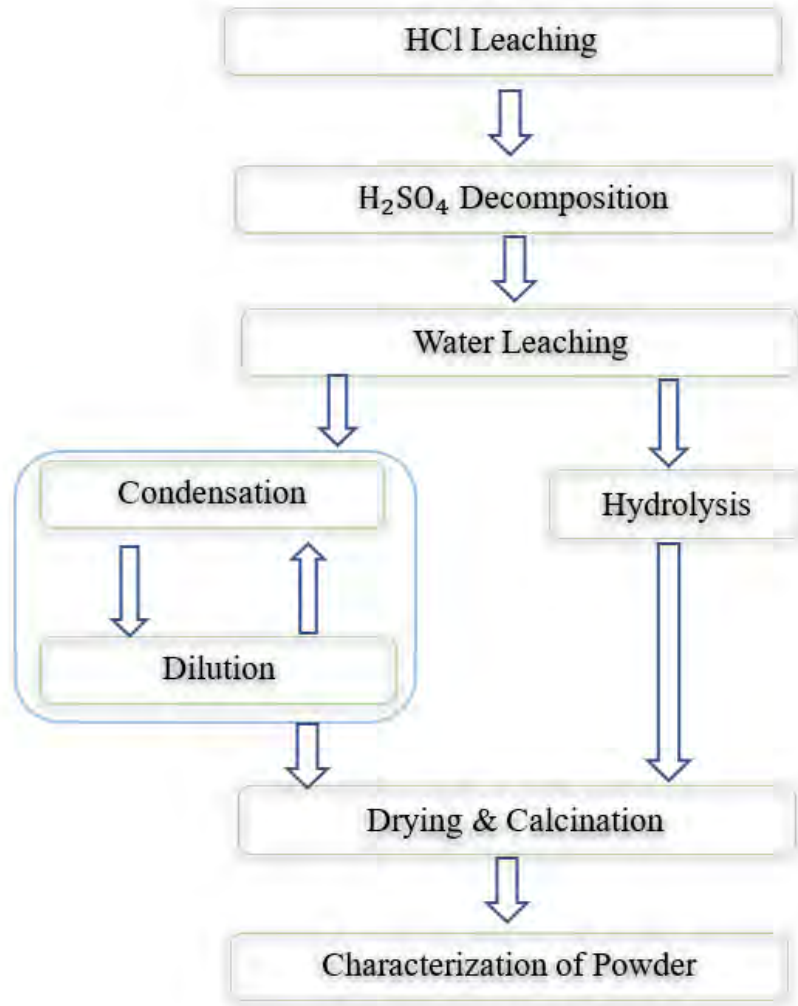


**Figure 3-4:** Flowsheet of upgradation of titania from sand sample

### 3.4.1 Leaching with HCl solution

Leachant of 20w/w% HCl solution was prepared and initially heated at 95°C, and sand [Figure 3.5a] was poured in it with the solid liquid weight by volume ratio of 1:6. The agitation was fixed at 400 rpm for 6 hours long leaching process [Figure 3.5 b, c] and the temperature was maintained at boiling temperature (107-108°C). After completion, the solution was cooled rapidly and washed with 5% HCl, centrifuged at 2000rpm (Model- Velocity 14, Dynamica, UK) and solid residue was dried overnight at 110°C and weighed. With the residue, this step was repeated.

The residue was rich in titanium and the filtrate was rich in iron.





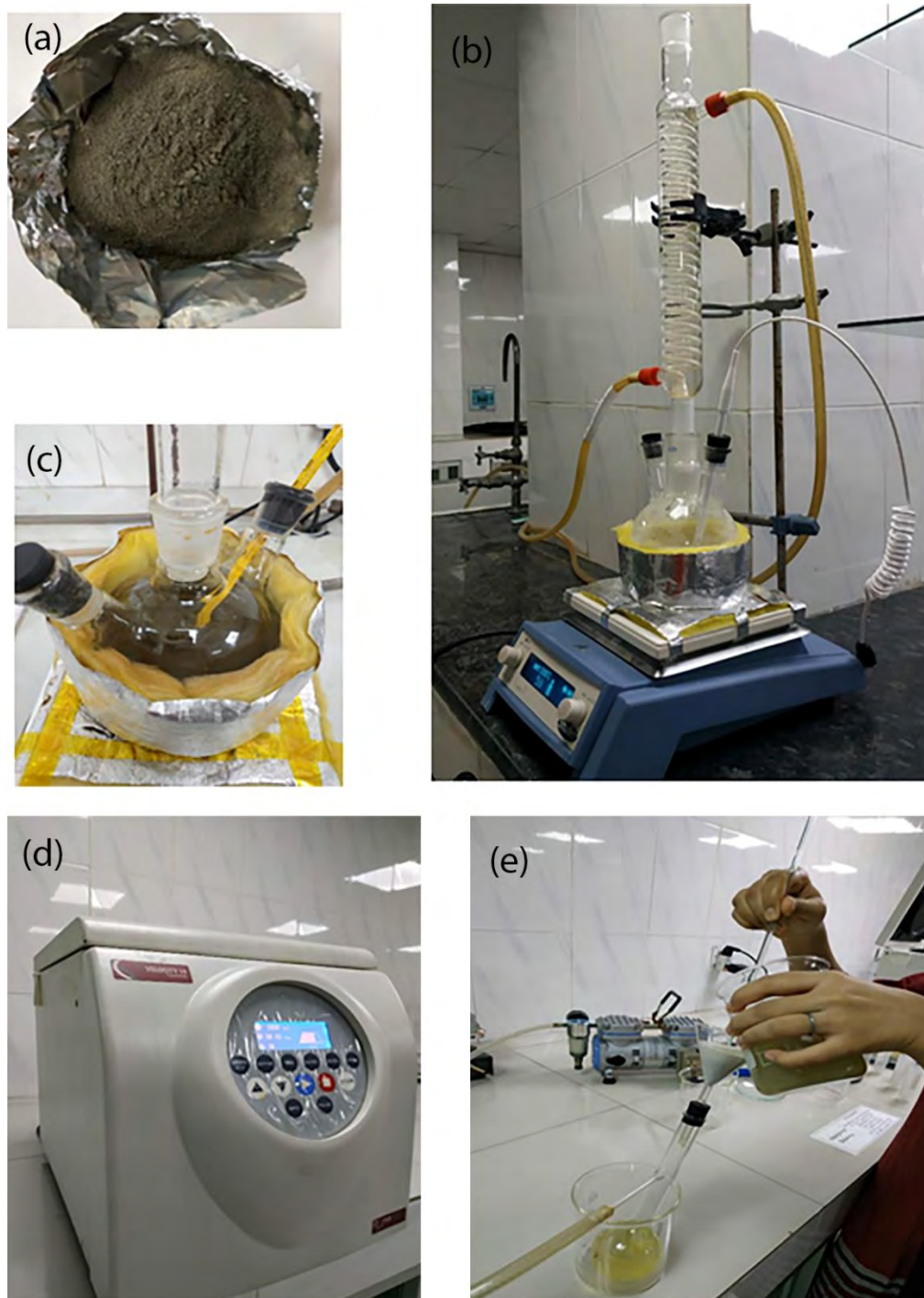
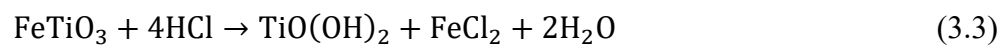
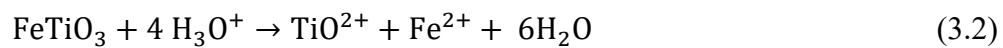
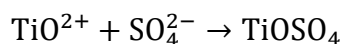
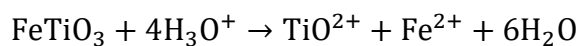
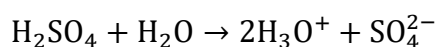


**Figure 3-5:** Leaching procedure (a) weighed dried sand, (b, c) sand poured in heated liquid inside 3-neck flask with condenser, (d) after completion rapid cooling and separation through centrifuge (e) filtration

### 3.4.2 Sulfuric acid decomposition

Sulfuric acid of high concentration was used to dissolve the titanium in solid residue of earlier step. After heating the sulfuric acid in a three neck round bottom flask with condenser at 135°C, sand was poured in it with solid liquid weight ratio of 1:3. Temperature was 150°C with agitation of 400rpm. Total weight of the paste (including the sand and solution) was measured. After completion the solution is cooled rapidly with ice water [83][112]. Initially the decomposition time of 45min, 60min, 90min, 135min were tried for acid of 80w/w% fixed concentration. The effect of varying time was observed after completion of upgradation, by observing morphology, yield, and elemental composition of the upgraded titania. Based on the observation results, 60minutes of decomposition time was selected for final five samples prepared by varying the acid concentration from 70%-90% with 5% interval.



### 3.4.3 Water leaching

Water was added to the paste of previous step in weight ratio of 1.5:1 water: paste. This water leaching step was continued for 100 minutes at 75-80°C. Then the solution was cooled and filtered while washed with 5% sulfuric acid. This step stabilizes the  $\text{TiO}^{2+}$  ion in solution. After centrifuge and then filtration, the filtrate is used in the next step while the residue is dried overnight and weighed and stored.

### 3.4.4 Separation of titanium from solution

#### 3.4.4.1 Repeated condensation and dilution

For the upgradation experiments with varying decomposition time at constant acid concentration, the water leached filtrate is condensed at constant temperature of 110°C until evaporation of all the water [Figure 3.6b]. Then the temperature is increased to the boiling temperature of the remaining acid until it turns to solid blackish crystals at the

bottom of the container. After that, it was diluted [Figure 3.6c] with about 10 times volume of the 98% acid initially added during decomposition. This condensation and dilution were repeated until white precipitation arrives at the bottom. Amount of precipitation and repetition time was unpredictable and inconsistent. For which for further upgradation with varying acid concentration, another separation method (hydrolysis) was followed.

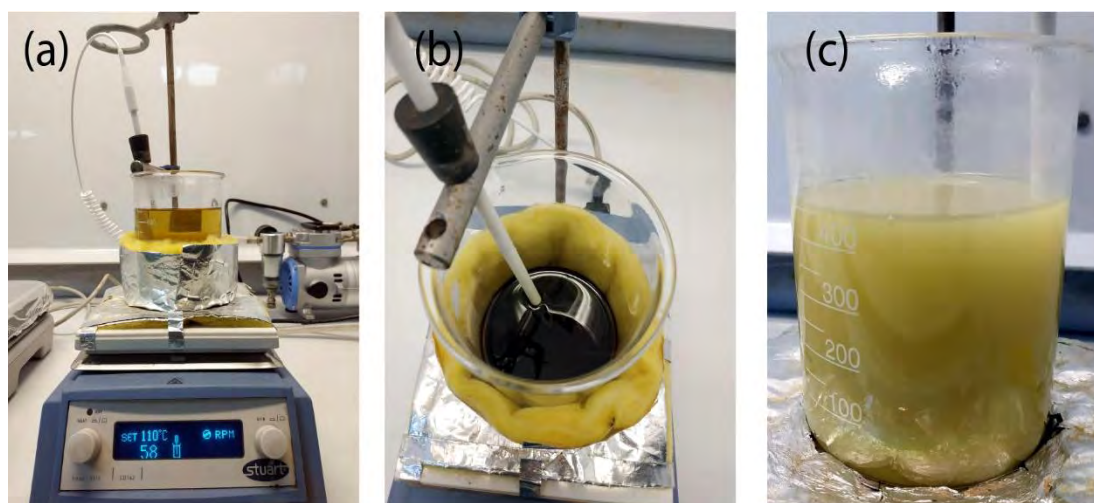


**Figure 3-6:** Repeated dilution and condensation to separate titanium from solution, (a) condensation (b) near end of condensation (c) dilution

#### 3.4.4.2 Hydrolysis

Filtrate was diluted up to 20:1 v/v ratio of total solution: initial concentrated acid added in decomposition step. The diluted solution was hydrolyzed at its boiling point (103-105°C) for 4 hours [Figure 3.7a]. Then the precipitation was separated by decantation [Figure 3.7b]. It was followed by drying the precipitate.



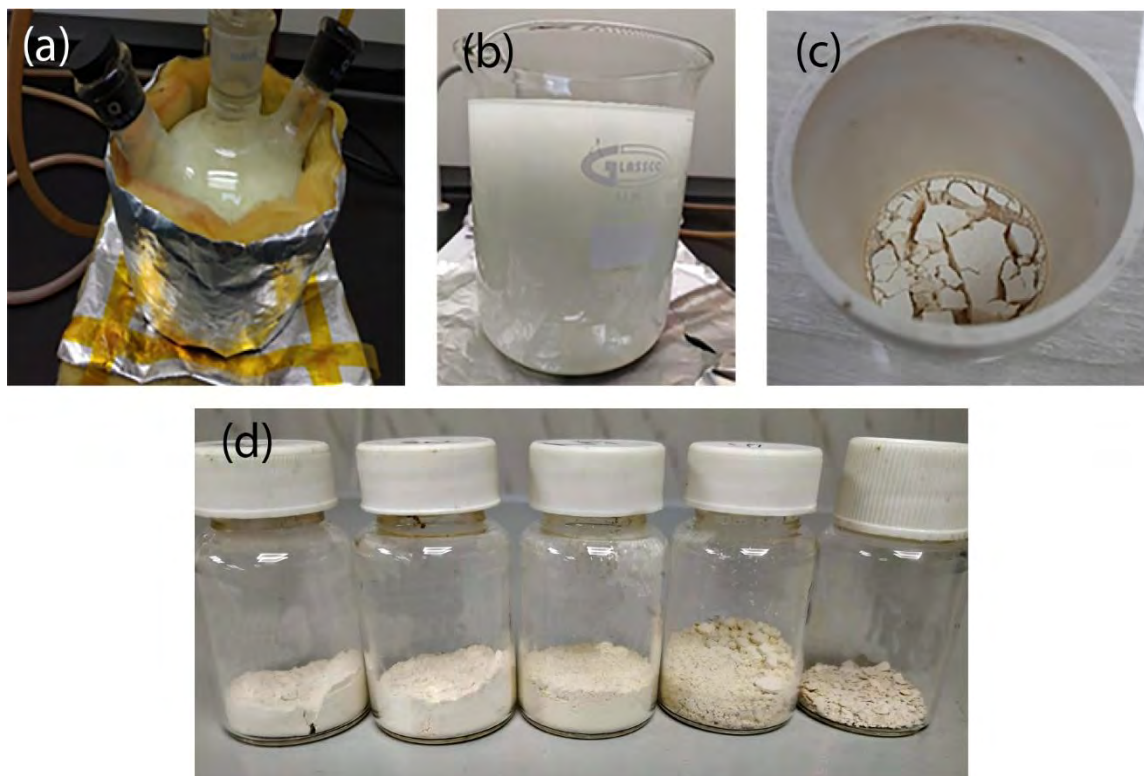


**Figure 3-7:** (a) Hydrolysis in three neck flask (b) solution poured in beaker after hydrolysis (c) dried and calcined powder in crucible (d) titania powder prepared with varying decomposition acid concentration

### 3.4.5 Drying and calcination

The precipitate was dried for 24h at 110°C and then crystallized at 900°C for 4 hours at 10°C /min. [Figure 3.7c-3.7d] for the samples prepared through varying decomposition time and at 500°C for the samples prepared with varying acid concentration.

### 3.5 Characterization of the Upgraded TiO<sub>2</sub> Powder

The initial samples prepared on trial for optimizing decomposition time were characterized based on morphology, composition, and structural properties. While the finally selected samples with higher yield, so that can be used for further application, were characterized based on the structural, morphological, compositional (ratio of titanium and oxygen in the titania) and optical properties. The characterized properties were compared with the properties required for solar cell application.

### 3.5.1 Morphology and composition

The SEM (SEM-EDX: Model- EVO18 Research, Carl Zeiss, UK) was used to observe the morphology and EDS was used to measure the element composition.

### 3.5.2 Structural property

The upgraded titania phase purity was characterized by XRD; peak position, intensity was matched with references available in crystallographic open database.

### 3.5.3 Optical property

The optical reflectance percentage was measured using the UV-Vis-NIR (palmer, lambda 365).

## 3.6 Film Preparation

### 3.6.1 Paste preparation

Calcined powder was grinded for 2hours using mortar and pestle through circular motion to refine the agglomeration.

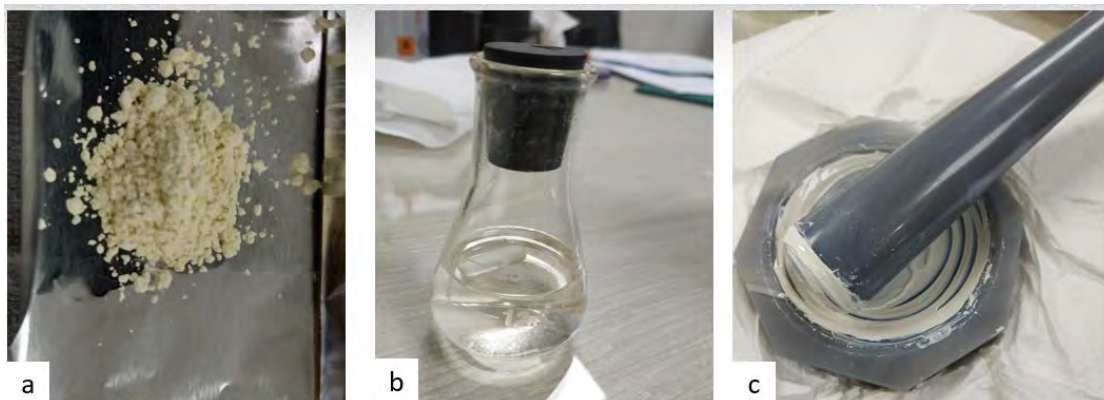


**Figure 3-8:** Paste preparation steps (a) powder of upgraded titania, (b) binder sol preparation, (c) paste preparation by mixing with hand grinding

A binder with 1:6:24 molar ratio of titanium iso-propoxide: citric acid: ethylene glycol was prepared [Figure 3.8b]. Its function is to bridge the particles and enable adhesion of the paste with substrate. To prepare binder, ethylene glycol was heated at 60°C, with continuous stirring; titanium iso-propoxide was added drop by drop. Finally, the

required amount of citric acid was added to it slowly with increasing temperature up to 90°C, though transparent solution formed near 85°C.

To prepare paste, 1g of grinded powder was mixed with 30 drops of binder and 10 drops of triton X-100 surfactant. The surfactant is added to prevent agglomeration of particles and increase surface area of the paste. Whole paste was grinded after addition of 3-4 drops of additives to make a homogenous well mixed paste [Figure 3.8c].

### **3.6.2 Film preparation**

To prepare mesoporous film of titanium dioxide, doctor's blade, screen printing and spin coating method was tried at first, using the powder samples prepared in initial trials. Based on average thickness, morphological property and stability and handling tolerance of the films, finally screen-printing method was used to prepare all the samples.

### **3.6.3 Drying and annealing**

The films were dried in air and annealed in the following cycle. 5minutes at 175°C, 5 minutes at 198°C, 10 minutes at 232°C, 15 minutes at 350°C, 30 minutes at 450°C. Heating rate was 2.5°C per minute for the whole cycle.

## **3.7 Characterization of Film**

The films were characterized based on the morphology, thickness, optical and electrical properties and compared with the required properties for solar cell photoanode.

### **3.7.1 Morphology**

The morphology was studied as before using the SEM to find the mesoporous or compact nature of the film and presence of substrate exposing crack in films.

### **3.7.2 Thickness and uniformity of thickness**

Using the Surface Profilometer (Model- DektaXT-A, Bruker Corp., USA), the average thickness of the prepared films was measured, and the uniformity of the films was observed by 3D mapping of the film areas.

### **3.7.3 Optical property**

The optical transmittance and optical absorbance of the films were measured using UV-Vis-NIR (Model- UH-4150, Hitachi High Tech. Corp., Japan) from the range of 300nm to 850nm.

### **3.7.4 Electrical property**

The hall-effect measurement was performed by the Hall Effect Measurement Unit (Model- HMS-3300, Ecopia Corp., South Korea) using the films to find the hall coefficient and resistance value.

## **3.8 Solar Cell Fabrication**

To find the suitability of the prepared films in solar cell application, DSSC cells were assembled using the prepared titania films as anode. The step of fabrication is shown below in Figure 3.9.

### **3.8.1 Counter electrode preparation**

A hole was drilled on the TCO (transparent conducting oxide) substrate, so that after assembling of two electrodes, the liquid electrolyte can be inserted through the hole. Then using sputter coater, 15nm of platinum coating was applied on each substrate to be used as counter electrode.

### **3.8.2 TiCl<sub>4</sub> treatment**

40mM TiCl<sub>4</sub>(aq) solution was prepared. Then it was heated at 60°C, on which the prepared TiO<sub>2</sub> films were kept immersed for 30minutes. After that, the films were dried for 10minutes on hot plate.

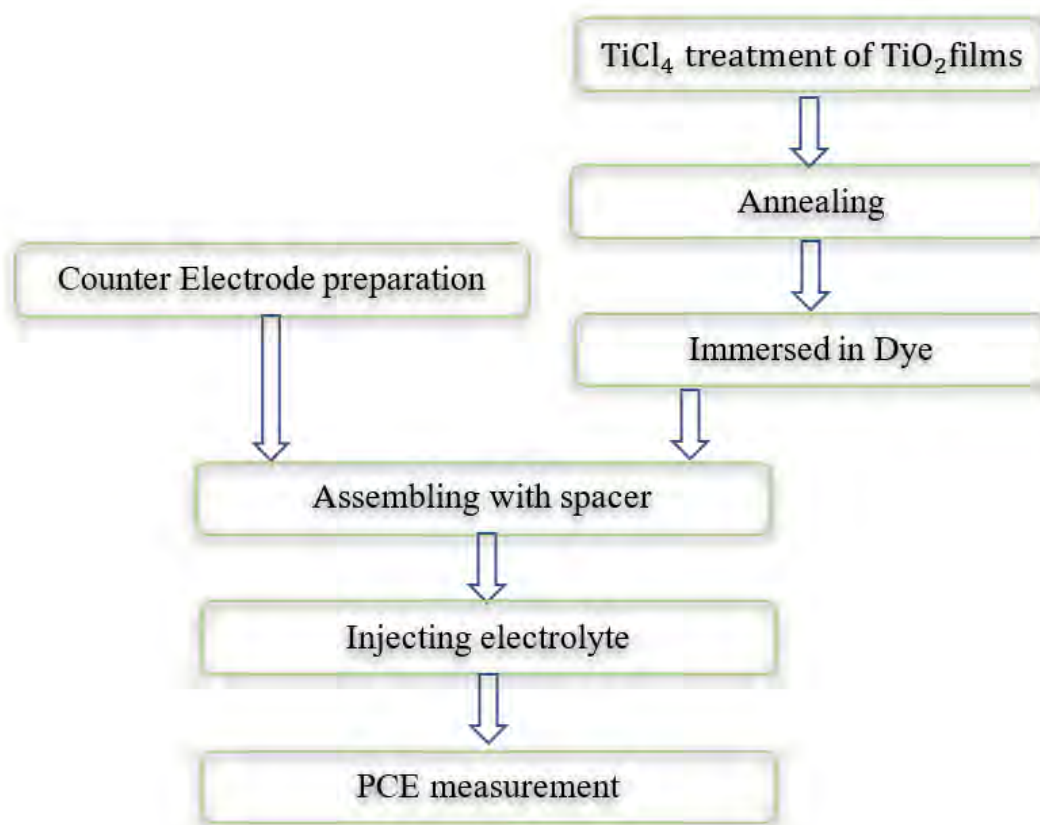


**Figure 3-9:** Flowsheet of DSSC Fabrication

### 3.8.3 Dye solution preparation

Solution of 0.5mM N3 dye with solvent of 1:1 v/v of Acetonitrile and Tert-butanol was prepared and stirred for 3h at 200rpm in dark [Figure 3.10a]

### 3.8.4 Film annealing and dye absorption

The  $\text{TiCl}_4$  treated films were annealed at  $450^\circ\text{C}$  for 30 min. then when the furnace temperature was cooled to  $80^\circ\text{C}$ , the films were dipped in dye solution and kept for 24h in dark. After the immersion step, the films were washed with acetonitrile and dried.

### 3.8.5 Electrolyte preparation

0.5M of  $\text{LiI}$  and 0.05M of  $\text{I}_2$  were added in acetonitrile solvent and stirred for 1h at 200rpm. For another batch of films, commercial electrolyte was used.

### 3.8.6 Cell assembling

Electrodes were joined [Figure 3.10b] with spacer at by pressing with 0.15MPa at 215°C for 30s. then the liquid electrolyte was injected inside.

### 3.9 Testing photoconversion

The light to electricity conversion efficiency of the assembled DSSC were measured using a Class AAA Sun Simulator (Model- K3000LAB55, McScience, South Korea).

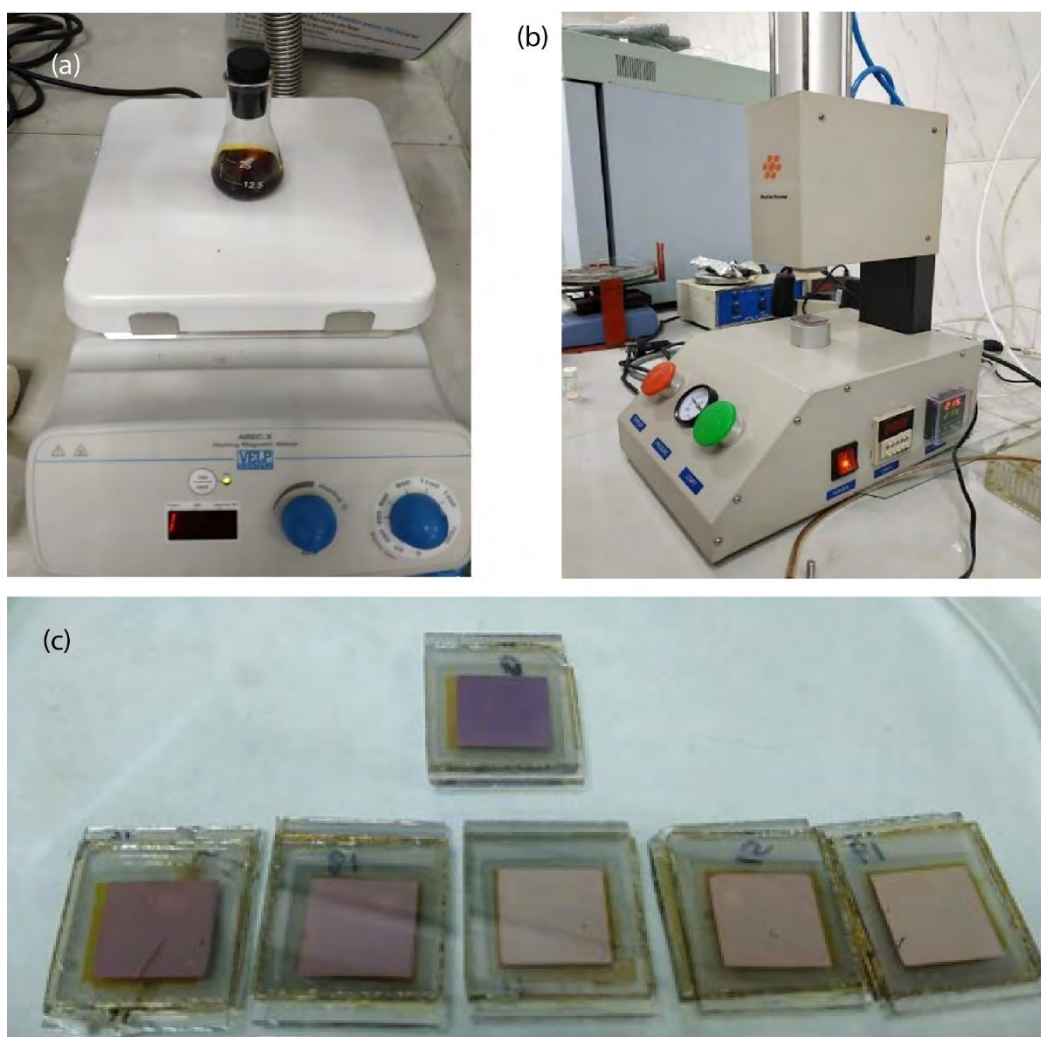


**Figure 3-10:** Assembling DSSC (a)dye solution preparation, (b)joining two electrodes with spacer, (c) assembled DSSC

### 3.10 Valorization of the Process Followed

- Lower temperature is required throughout the whole upgradation cycle making it a less energy-intensive process.
- The waste/by-products of the upgradation route are less threatening to environment and can be reused/regenerated/neutralized. Iron rich filtrate in the HCl leaching step can be either neutralized with limestone and landfilled or can be used for production of  $\text{LiFePO}_4$ . Or the acid can be used in acid regeneration technology (EARS) [87]. Iron sulphate is produced in very negligible amount, is cleaner as the impurities are separated in the first step; so, it can be utilized to prepare value-added products. Filtrate obtained after hydrolysis can be mixed with commercial 98% sulfuric acid to prepare an acid solution of about 80% used in the sulfuric acid decomposition.
- Though it was rutile sand, the titanium dioxide was extracted from the ilmenite fraction of it. The titania of rutile fraction was too low to follow chlorination process and remains inert in the followed improved sulphate process.
- A new line of sand to solar cell indicates high value product of our available cheap sand can be utilized in research and industry.
- The reagents used are not very expensive. But multiple steps are involved in this process.

## 4. RESULTS AND DISCUSSION

### 4.1 Introduction

One of the objectives of this study was to upgrade the cox's bazar beach sand into synthetic titanium dioxide. It was decided to follow direct hydrometallurgical route to reduce the energy consumption throughout the upgradation process. The sand sample was characterized in as-received condition and/ or after particle-size reduction by mechanical milling. The particle size distribution of the sand before and after milling were measured by sieve analysis. The mineralogical composition of as-received sand was analyzed by taking polarizing microscopic image and performing Rietveld refinement of the XRD data. Structural and compositional analysis of some upgraded titania samples and some residue sand samples were performed by XRD and XRF. All the upgraded titania samples were observed in SEM for morphology study, among which elemental composition of some were performed by EDS. The structural, morphological, compositional, optical, and electrical properties of the films prepared from the upgraded five titania samples were analyzed by XRD, SEM, EDS, XRF, UV-Vis, Hall-effect measurement, respectively. Along with these properties, the suitability of those prepared films for DSSC cell were studied directly by measuring the photo-conversion efficiency (PCE) in solar simulator of the assembled DSSC cell.

The results of these investigations are presented and discussed below as in the following sub-heading.

- a. Characterization of the as-received sand (Structural and mineralogical)
- b. Characterization of the upgraded  $\text{TiO}_2$  powder (Structural, yield, morphological, composition and optical)
- c. Characterization of the titania film (Morphology, thickness, electrical and optical)
- d. Measurement of PCE of the assembled DSSC.
- e. Discussion of the results.



## 4.2 Characterization of the As-received Sand (Structural and Mineralogical)

The as-received sand was beneficiated by BSMEC from the Cox's Bazar Beach Sand (Raw) through the following physical separation steps to concentrated Rutile Sand.

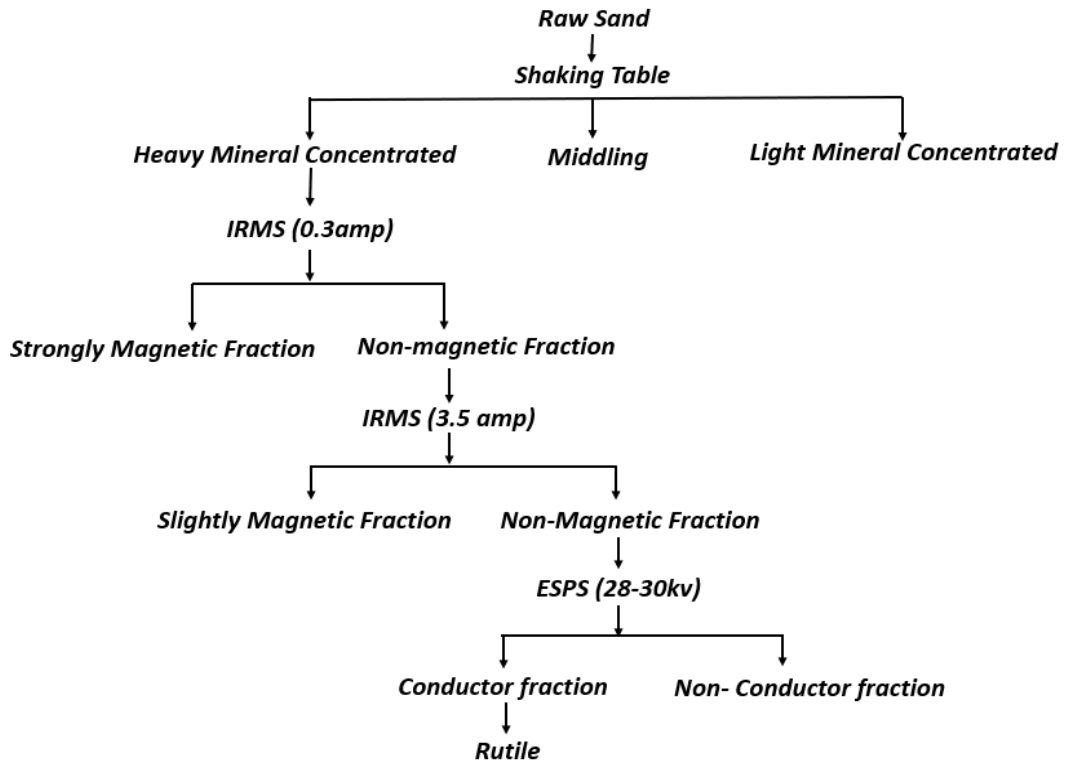


**Figure 4-1:** Beneficiation history of as-received sand

### 4.2.1 Particle size distribution of as-received sand

Particle size distribution of raw material has a significant influence on the leaching or reaction rate. To accelerate the recovery of iron or titanium through their separation in either solid or liquid phase, reducing the particle size is important. But too low particle size can negatively affect the filterability.

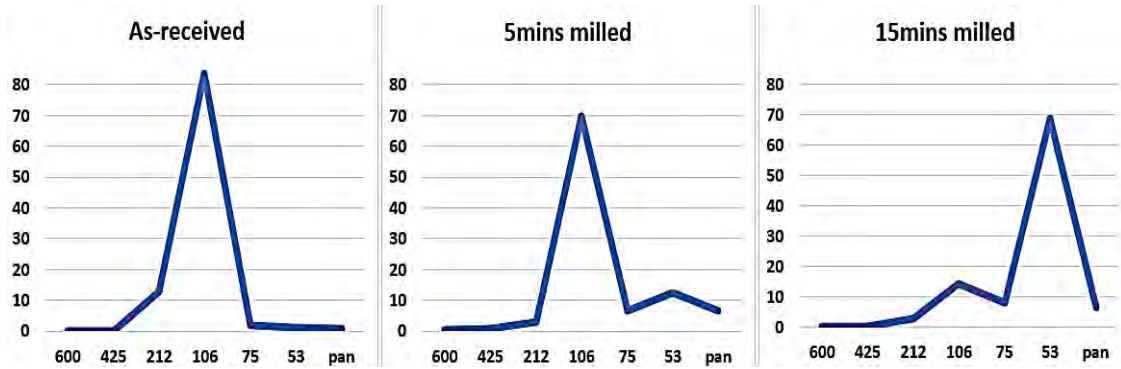


**Figure 4-2:** Size distribution of sand

The weight percentage of different size-ranged particle is tabulated below in Table 4.1.

**Table 4-1:** Size Distribution of As-received Sand and Ball milled Sand

Mesh size ( $\mu$ )	As received	Ball-milled (400rpm,5mins)	Ball-milled (400rpm,15mins)
	Wt. %	Wt. %	Wt. %
>600	0.04	0.2	0.04
425-600	0.07	0.67	0.06
212-425	12.88	3.09	2.62
106-212	83.46	69.86	14.13
75-106	1.76	6.69	7.95
53-75	1.12	12.51	68.68
<53	0.67	6.63	6.52

As shown in the Table 4.1, the as-received sand had 83.46% particles sized in range of 106-212 $\mu$ , in total 96.45% particles size above 106 $\mu$ . The 15 minutes ball milled sand, having 68.68% particles in 53-75 $\mu$  range, had only 16.85% particles sized above 106 $\mu$ . And the 5 minutes ball milled sand had 69.86% particles in 106-212 $\mu$  range, in total 74.17% particles above 106 $\mu$ . The distribution profile is shown in Figure 4.2.

#### 4.2.2 Morphology and mineralogy of as-received sand

The morphology was observed using both SEM and polarizing microscope. The heavy minerals present in the as-received sand were identified and quantitatively measured using polarizing microscope. From the SEM images in Figure 4.3, different shaped grains (irregular spherical, elongated) of about 100-200 $\mu$  size were observed, which agrees with the result of sieve analysis showing more than 80% grains are on the range of 106-212  $\mu$ .

Better understanding of the morphology had been possible with polarizing microscopy. The mineralogy of the sand sample was observed by grain slide analysis with polarizing microscope. From the images, the minerals were identified with the help of Michel-Levy interference color chart. From the traditional Michel-Levy chart [113], it is evident that, the polarization colors visualized in the microscope and recorded onto film or captured digitally can be correlated with the actual retardation value, thickness, and birefringence of the specimen. This, as a result can be used as a key to identify minerals. The grains of the minerals present can be identified both quantitatively and qualitatively through this microscopy.

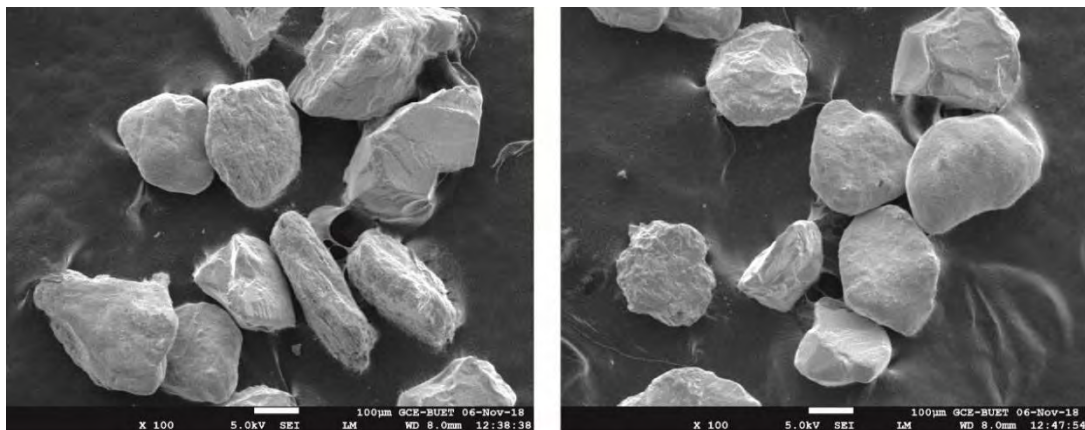


**Figure 4-3:** Microscopic image of as-received sand (100X)

In Figure 4.4, presence of rutile along with other garnet, silica, zircon minerals along with traces of monazite, chloritoid etc. can be observed. The images taken in plane-polarized light and cross-polarized light were matched with references to identify the mineral type of grains [114]. As ilmenite is one of the opaque minerals in both type of lights, it's grains could not be distinguished from other opaque minerals including

magnetite and hematite. So, titanium bearing minerals in this sand sample include rutile and probably ilmenite.

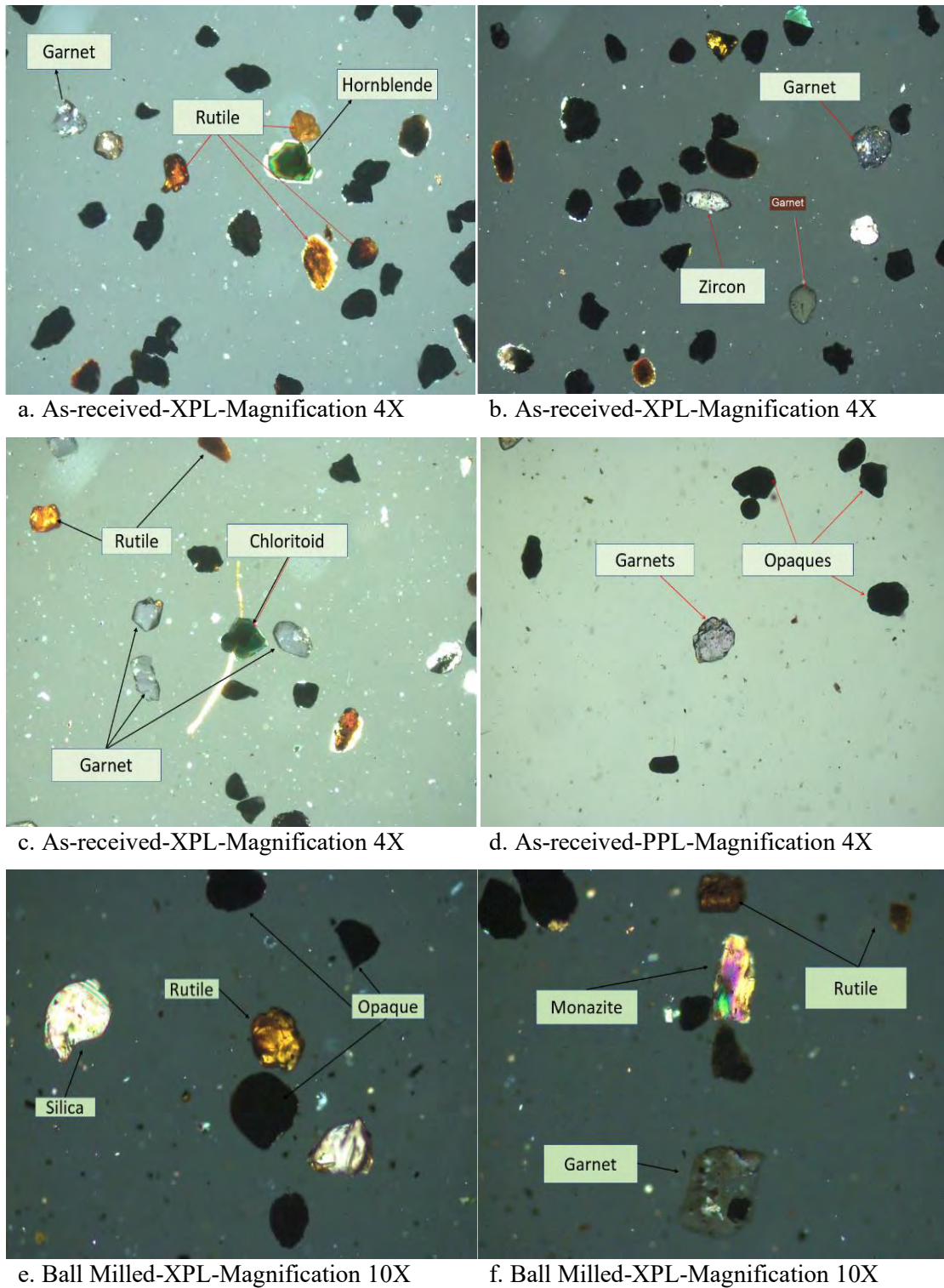


Figure 4-4: Polarizing Microscopic Image of As-received sand before (a-d) and after particle size reduction (e-f)

**Table 4-2:** Relative Percentage of the minerals present in As-received sand

Heavy Minerals	Percentage (%)
Opagues (Magnetite, Ilmenite, Hematite)	35
Rutile, TiO <sub>2</sub>	25
Garnet, (Silicates of Ca/Al/Mg/Fe/Mn/Cr)	22
Silica, SiO <sub>2</sub>	8
Hornblende	3
Zircon, ZrSiO <sub>4</sub>	2
Monazite	2
Tourmaline	1
Chloritoid	1
Staurolite	1

The relative percentage of the minerals can be quantified by calculating the number of individual mineral grains in the sample slides relative to the total number of grains. As observed from Table 4.2, in total, the opaque minerals were quantified to be 35% of the total grains in sample slide, while rutile was about 25% of the sample slide. Silica grains were about 8%, but silicon is present as silicates of other elements too.

#### 4.2.3 Phase identification of as-received sand

The XRD pattern of the as-received sand is shown in Figure 4.5a. The prominent peak position of the diffraction curve showed agreement with phases of Rutile-TiO<sub>2</sub> (ICSD -93097), Silicon dioxide- SiO<sub>2</sub>(ICSD-168355), Pyrope-ferroan-Mg<sub>1.6</sub>Fe<sub>1.2</sub>Ca<sub>0.2</sub>Al<sub>2</sub>Si<sub>3</sub>O<sub>12</sub> (ICSD-23845), Ilmenite- FeTiO<sub>3</sub> (ICSD-43466), Hematite-Fe<sub>2</sub>O<sub>3</sub> (ICSD-184766), Merrihueite- K<sub>2</sub>Mg<sub>5</sub>O<sub>30</sub>Si<sub>12</sub>(ICSD-77131) with a goodness of fitting (GOF) value of 1.03579.

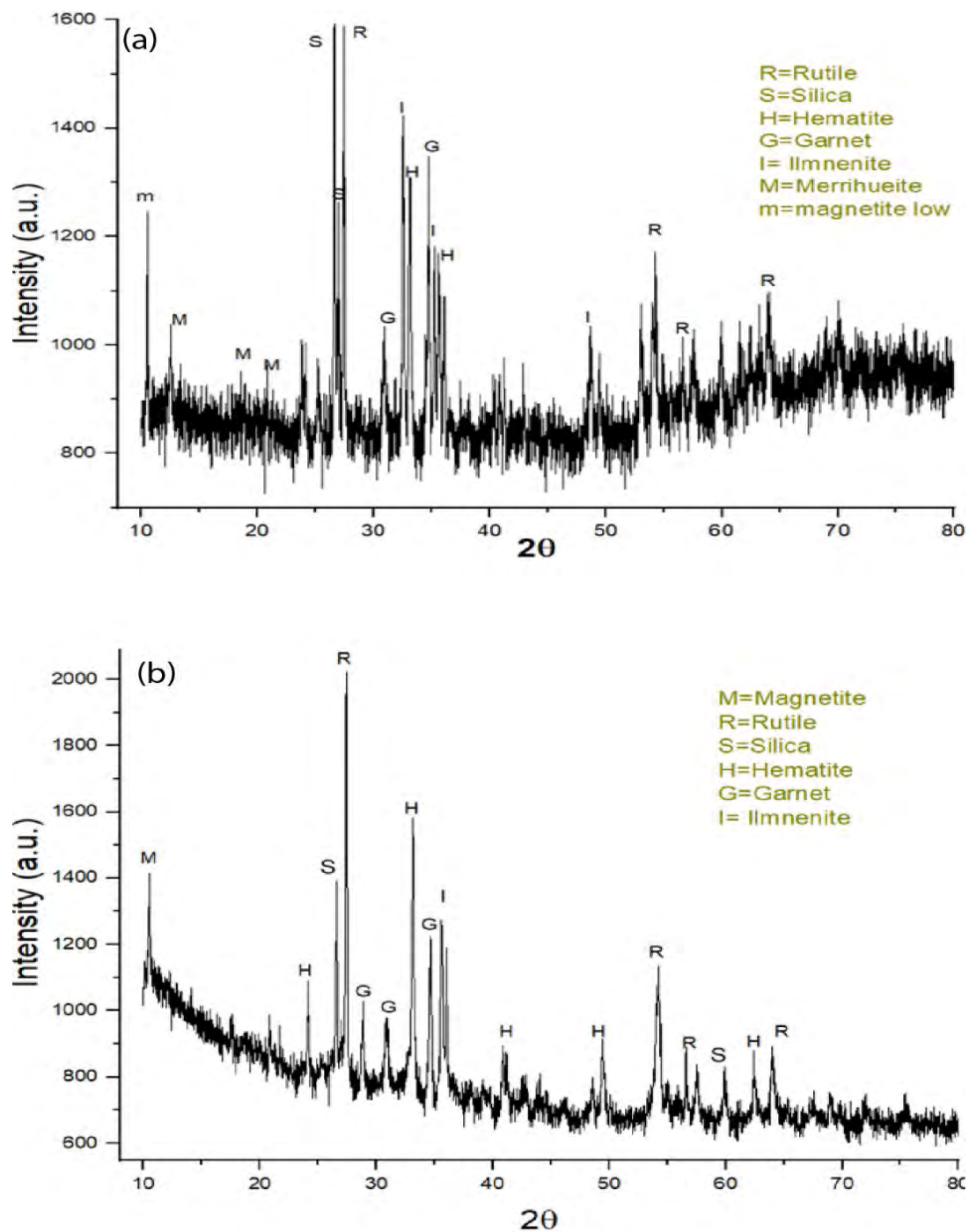


Figure 4-5: XRD plot of (a) as received sand and (b) 750°C heat treated sand

Some of the ball-milled sand was heated at 750°C for 3 hours and then characterized with XRD. The XRD pattern of the heat-treated sand is shown in Figure 4.5b. The prominent peak position of the diffraction curve showed agreement with phases of



Rutile-  $\text{TiO}_2$  (ICSD-168138, 167965, 51932), Silica-  $\text{SiO}_2$  (ICSD-89277), Grossular-  $\text{Al}_2\text{Ca}_3\text{Si}_3\text{O}_{12}$  (ICSD-86350), Magnetite- $\text{Fe}_3\text{O}_4$  (ICSD-98084), Ilmenite-  $\text{FeTiO}_3$  (ICSD-153494), Hematite- $\text{Fe}_2\text{O}_3$  (ICSD-43465) with a goodness of fitting (GOF) value of 1.05251.

**Table 4-3:** Phases Identified by peak position of dried and heat-treated sand

Phases Identified	% In Dried Sand	% In Heat treated Sand
Rutile	15.2%	27.7%
Ilmenite	22.3%	11.2%
Hematite	18.1%	23.6%
Magnetite	-	1.4%
Silicon oxide	10%	11.1%
Garnet (Grossular/Pyrope ferroan)	22.3%	25%
Merrihueite	12.1%	-

From Table 4.3, we can see that, the rutile content of the as received sand was approximately 15%. But other titanium bearing mineral ilmenite is about 22%. After the heat treatment the ilmenite content was decreased and both hematite, rutile content increased. It can be attributed to the oxidation of ilmenite to hematite and rutile during the heat treatment. Also, the amount of silica and garnet phases match with the result obtained from polarizing microscope.

#### 4.2.4 Composition of as-received sand

The composition of the as-received sand was analyzed using XRF and the result in Table 4.4 shows that, very high concentration of iron is present in this sand sample, majority in hematite and ilmenite. Similarly, both rutile and ilmenite are the source of titanium. The total content of titanium dioxide, present in both rutile and ilmenite phase is only 21.4% in this rutile concentrated sand. Among the impurities present, Fe, S, P, Si, Ca, Al, Mg are tough to remove completely through upgradation routes other than

chlorination, as shown in the table. The sample also contains S, Zr, Nb, Cr, Sn, Y, Ce as impurities, which, because of their band gap tuning capability, have been studied as dopant in  $\text{TiO}_2$  anode used for high-efficient photovoltaic device [59].

**Table 4-4:** XRF composition of as-received sand

Analyte	Mass%	Analyte	Mass%
$\text{Fe}_2\text{O}_3$	42.5	$\text{ZrO}_2$	0.608
$\text{TiO}_2$	21.4	$\text{CeO}_2$	0.591
$\text{SiO}_2$	16.7	$\text{P}_2\text{O}_5$	0.380
$\text{Al}_2\text{O}_3$	8.14	$\text{Nd}_2\text{O}_3$	0.3
$\text{CaO}$	2.13	$\text{ThO}_2$	0.280
$\text{Cr}_2\text{O}_3$	1.92	$\text{La}_2\text{O}_3$	0.264
$\text{MgO}$	1.71	$\text{Na}_2\text{O}$	0.227
$\text{MnO}$	1.08	$\text{Nb}_2\text{O}_5$	0.211
$\text{K}_2\text{O}$	0.911	Y, S, Ni, Rb, Sr, Sn, Sm, Pb, U	0.654

For having low content of rutile, dry chlorination process is not suitable for this sand to upgrade, as this process requires high grade rutile ore. On the other hand, conventional sulfate process would create harmful byproduct of  $\text{FeSO}_4$  because of high content of Fe in this sand. To remove the major impurity of Fe, upgradation was started with HCl leaching because of its higher efficient selective leaching, which agrees with the purpose of low energy requirement and environment friendly disposal.



#### 4.2.5 Comparison of composition obtained from XRF, XRD and polarizing microscope (PM)

Table 4.5 shows the summary of the raw sand composition obtained from polarizing microscopic slide analysis, from XRD through Rietveld analysis and from XRF analysis. The target element titanium is present in rutile, ilmenite and garnet, so relative percentage of these minerals are shown in the following table.

**Table 4-5:** Comparative analysis of sand composition

Analyte	% From PM	% From XRD	% From XRF
TiO <sub>2</sub>	25	15.2	21.4
Ilmenite	Total opaque 35	22.3	-
SiO <sub>2</sub>	8	10	16.7
Garnet	22	22.3	-

Other studies investigating beach sand minerals of Bangladesh showed [2] that, percentage of titanium dioxide in ilmenite, rutile, garnet is about 43%, 90% and 0.2%, respectively. Including titania from all three minerals, the total titania in the sand sample is calculated to be 25.8%, which is in close match with the titania content calculated via XRF (21.4%) and polarizing microscopic image (25%). Silicon dioxide and garnet content obtained are also close for polarizing microscope and XRD.

To measure the relative mineral percentage using XRD and PM is comparatively more accurate than XRF, as XRF is not designed for mineral identification, rather for total element identification. So, it can be considered that, the total titanium present in ilmenite, rutile or garnet is counted in XRF.

#### 4.3 Characterization of the upgraded TiO<sub>2</sub> powder (Structural, optical, and morphological)

After the upgradation, the structural, morphological, optical properties of the extracted powder were measured.

### 4.3.1 Structural properties and composition

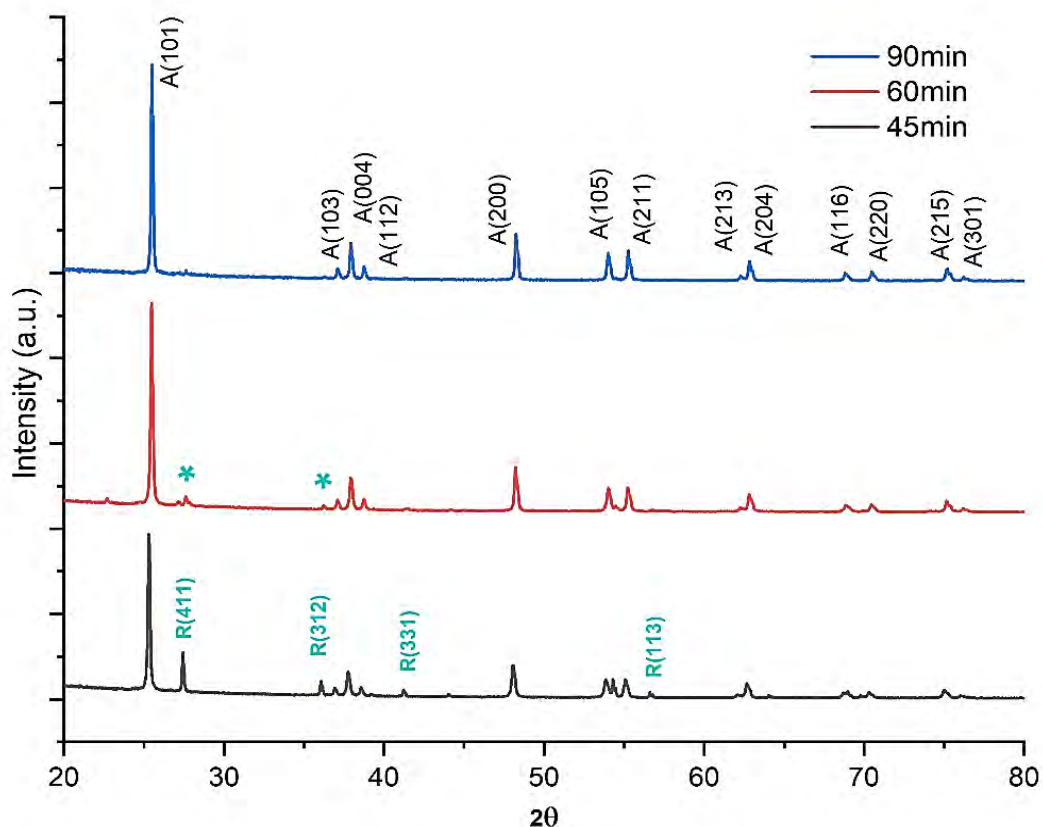
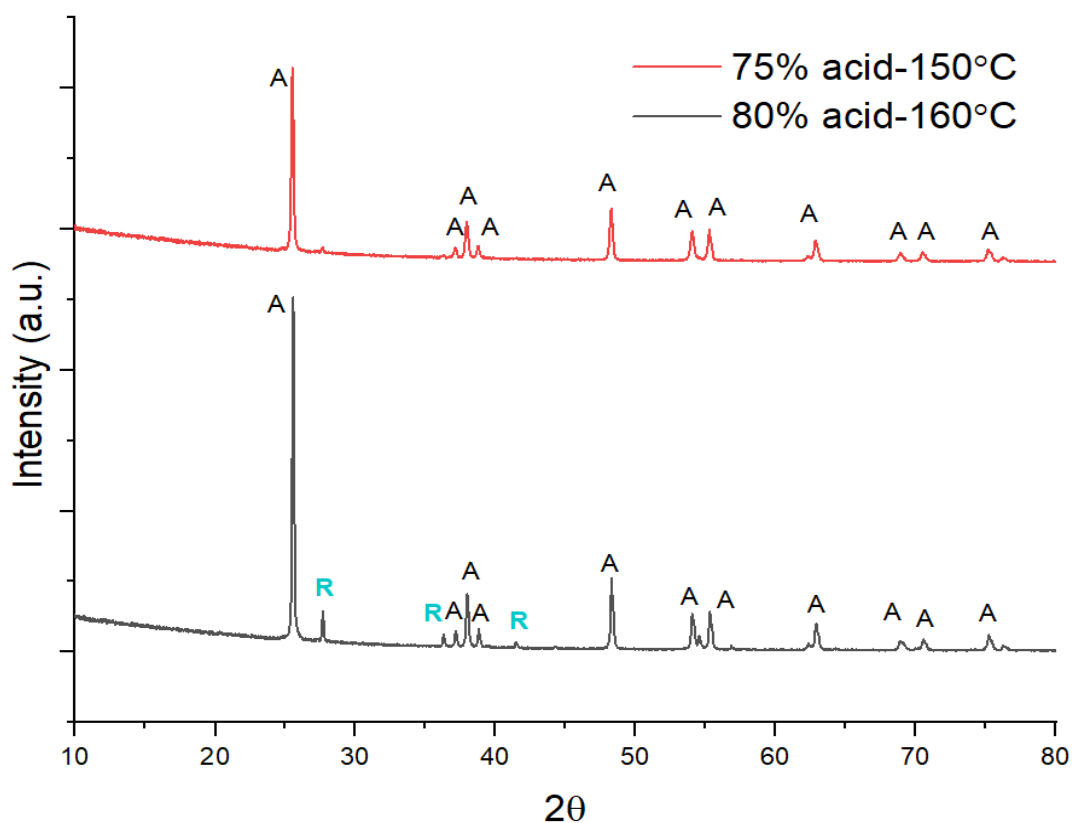


Figure 4-6: Titania powder (annealed at 900°C) obtained through varying  $H_2SO_4$  decomposition time (90min, 60min, 45min) during upgradation

The XRD patterns of initial samples prepared by varying acid decomposition time in the upgradation route of *HCl leaching- $H_2SO_4$  decomposition- water leaching-repeated condensation-dilution- -drying-calcination* is shown in Figure 4.6. All the samples show sharp peaks of anatase titania A. The 45minute decomposed sample shows a few peaks of rutile too, among which R (411) is of comparatively higher intensity. With increasing temperature in 60 minutes decomposed sample, the relative intensity and number of rutile peaks decreased. And for 90 minutes decomposed one, there is no rutile peaks present in the sample. XRD plot of the 90minutes sample was fitted by Rietveld refinement and found to contain about 98.1% anatase (ICSD-24276) with 1.7% silicon dioxide (ICSD-170541) and 0.2% titanite (ICSD-89748), with the GOF value of 1.72827. The average crystallite size was calculated to be 65.1nm, 57.7nm, 75.8nm for the 45min, 60min, 90min decomposed samples, respectively.

Even though single phase anatase peaks along with lower impurity content were obtained for 90min sample. But the larger grain size makes it weaker candidate for applications requiring high surface areas. The morphology of the 60min sample was more uniform. Beyond 60 minutes, with increasing decomposition time, the yield of titania powder decreased, which can be attributed to the failure to measure exact pH for precipitation to occur. As yield and morphology are two important concerns for this work, further upgradation was performed with 60minutes decomposition time as optimum for this work.



**Figure 4-7:** Titania powder (annealed at 900°C) obtained through 60min decomposition time and 75% H<sub>2</sub>SO<sub>4</sub> (150°C) and 80% H<sub>2</sub>SO<sub>4</sub> (160°C) following Hydrolysis

The XRD patterns of extracted titania powder through upgradation route of *HCl leaching-H<sub>2</sub>SO<sub>4</sub> decomposition- water leaching- hydrolysis-drying-calcination* is showed in Figure 4.7. For the same decomposition time of 60minutes and hydrolysis separation phase, sample obtained through 80% acid-160°C decomposition condition resulted in mixed rutile and anatase titania peaks, while the 75% acid-150°C condition resulted in single anatase phase with no visible rutile peaks.

The unavailability of tools to measure exact pH and concentration of  $\text{TiO}^{2+}$  required for precipitation to occur makes the earlier mentioned upgradation route (route including repeated condensation-dilution) inconsistent. And, as the yield of titania powder obtained by the upgradation route of *HCl leaching -  $\text{H}_2\text{SO}_4$  decomposition - water leaching - hydrolysis - drying - calcination* results in higher yield than the route including repetitive condensation-dilution, five samples were prepared with varying acid concentration with hydrolysis separation step.

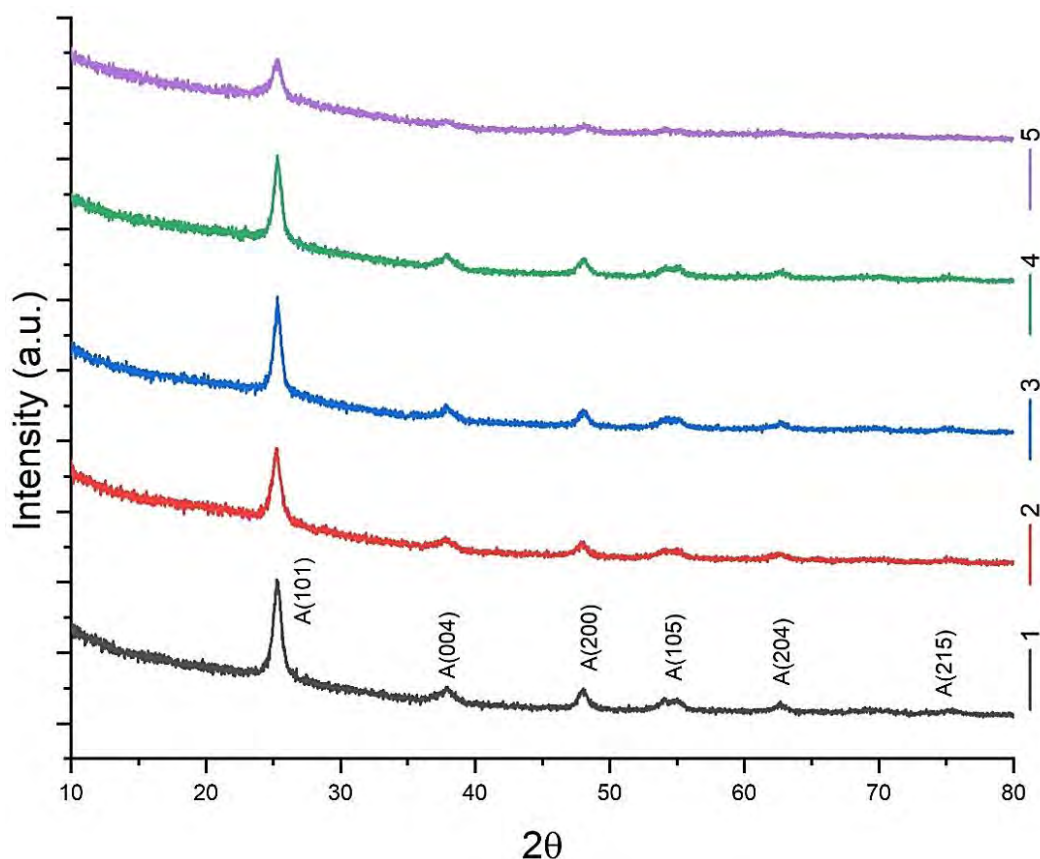


**Figure 4-8:** Titania powder (annealed at  $500^\circ\text{C}$ ) obtained through 60min- $150^\circ\text{C}$  decomposition condition with varying acid concentration (1. 70%, 2. 75%, 3. 80%, 4. 85%, 5. 90%) following Hydrolysis.

Figure 4.8 shows the XRD patterns of the  $500^\circ\text{C}$  annealed samples prepared with varying sulfuric acid concentration. In those samples, the peaks were of lower intensity and broader area, indicating lower crystallinity of the samples, which can be attributed to the lower annealing temperature in ambient condition.

The crystallographic information calculated from the XRD data is shown in the table below. The crystallite size ( $D$ ) was calculated using the Scherrer formula [115] (4.1).

$$D_{hkl} = \frac{0.94\lambda}{\beta \cos\theta} \quad (4.1)$$

In (4.1), (hkl) are the miller indices of the planes,  $\lambda$  is the X-ray wavelength (0.15406 nm), and  $\beta$  is the full width at half maximum (FWHM) of the diffraction peak at  $2\theta$ , where  $\theta$  is the Bragg diffraction angle, both  $\beta$  and  $\theta$  are in radians. The FWHM of the most prominent peak (101 crystallographic plane) was calculated using Origin Lab (Origin2021) software. The developed micro-strain ( $\epsilon$ ) along (101) plane was calculated from the relation[116] (4.2)

$$\epsilon = \frac{(\beta \cot\theta)}{4} \quad (4.2)$$

where  $\theta$  is the Bragg diffraction angle and  $\beta$  is the width of the peak at half of the maximum peaks. The dislocation density is the length of dislocation lines per unit volume of the crystal [117]. Dislocation is a crystallographic irregularity within a crystal structure, and it could change the characteristics of materials. The dislocation density ( $\delta$ ) is determined from Williamson- Smallman relation, using the expressions: The dislocation density along (101) is calculated by the Williamson and Smallman's relation (4.3)

$$\delta = \frac{n}{D_{hkl}^2} \quad (4.3)$$

Where, n is a factor, which equals unity giving minimum dislocation density and  $D_{hkl}$  is the crystallite size along [hkl] direction.

The interplanar distance (d-space) along (hkl=101) crystallographic plane is calculated using the relation (4.4)

$$d = \frac{\lambda}{2\sin\theta} \quad (4.4)$$

As for tetragonal unit cell of Anatase, the relation among interplanar spacing (d) with the lattice parameter (4.5), to find lattice parameter c, d-space for plane (004) was used and to calculate the lattice parameter a, d-space for plane (200) was used. Then the unit cell volume was calculated using the relation  $V = \frac{1}{4}a^2c$ , as anatase has 4 polyhedra per unit cell.

$$\frac{1}{d^2} = \frac{h^2+k^2}{a^2} + \frac{l^2}{c^2} \quad (4.5)$$

**Table 4-6:** Crystallographic data obtained from XRD plot

Sample ID	H <sub>2</sub> SO <sub>4</sub> % (w/w)	Crystallite size (nm)	Microstrain (* 10 <sup>-3</sup> )	Dislocation Density(* $\frac{10^{-3}}{\text{nm}^2}$ )	Each polyhedron volume (nm <sup>3</sup> )	d-space (along 101)
1	70	11.869	13.939	7.098	0.03403	0.35202
2	75	12.211	13.57	6.706	0.03402	0.35257
3	80	14.831	11.138	4.546	0.03406	0.35147
4	85	12.968	12.728	5.946	0.03398	0.3512
5	90	11.863	13.914	7.106	0.03396	0.3512

Table 4.6 shows that, crystallite size increased from sample 1 to 3 and then decreased again. So, sample 3 has the highest crystallite size among the five samples, resulting in lowest macrostrain, dislocation density and highest unit cell volume among the five samples.

### 4.3.2 Yield

The weight of the samples prepared by varying acid concentration of 70% to 90% during decomposition at 150°C for 60 minutes were measured after annealing at 500°C. The yield is tabulated below in Table 4.7.

**Table 4-7:** Weight of upgraded titania powder after annealing and quality of precipitation

Sample ID	H <sub>2</sub> SO <sub>4</sub> % (w/w)	Weight extracted	Quality of precipitation	Annealing Condition
1	70	3.7954g	Sticky, Very slow precipitation settle	Temperature: 500°C Duration: 4h Ramp: 10°C/min
2	75	3.8277g	Not sticky, very slow settle	
3	80	2.4910g	Not sticky, faster settle	
4	85	3.5230g	Not sticky, faster settle	
5	90	0.8851g	Not sticky, slow settle	

Though highest yield was for sample 2, the yield for sample 1, 3, 4 was close to it. But sample 5 has the lowest yield which less than 1/4<sup>th</sup> of sample 2. Also, the change in acid

concentration of Ti decomposition step influenced the quality of hydrated titania obtained after hydrolysis. Titania obtained for sample 1 was sticky to glass beaker, while the other four samples were non-sticky. Although, after annealing, sample 1 became non-sticky too.

After completion of hydrolysis, the settlement of the precipitates in solution was slowest for sample 1 and 2, slow for sample 5, and comparatively fast for sample 3 and 4. This may be attributed to the difference of density of precipitates due to agglomeration occurred during 4-hour long hydrolysis step.

### 4.3.3 Morphology

Among the initial upgradation trials of varying sulfuric acid decomposition time (80% acid, 150°C), better morphology (smaller particle size) was obtained for 60min decomposition time (Figure 4.9).

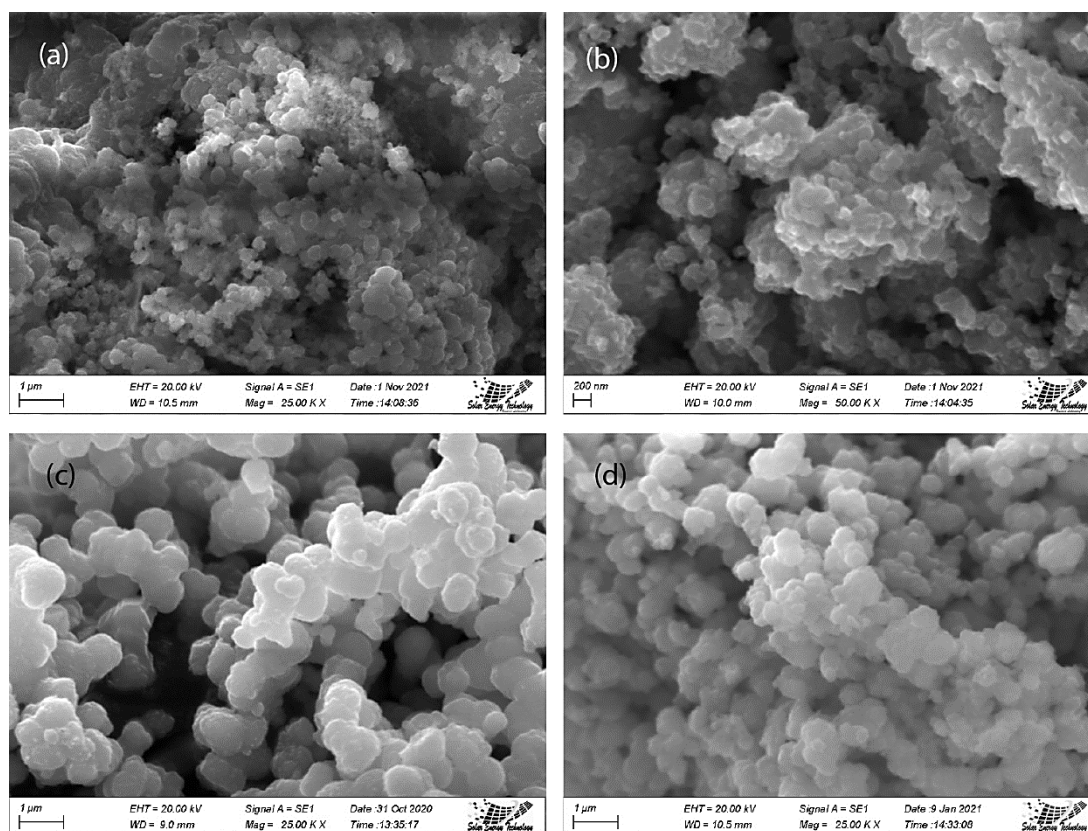


**Figure 4-9:** SEM image of Titania (annealed at 900°C) extracted using HCl 80% $H_2SO_4$ , 150°C for (a) 45min, (b) 60min, (c) 90min, (d) 135min



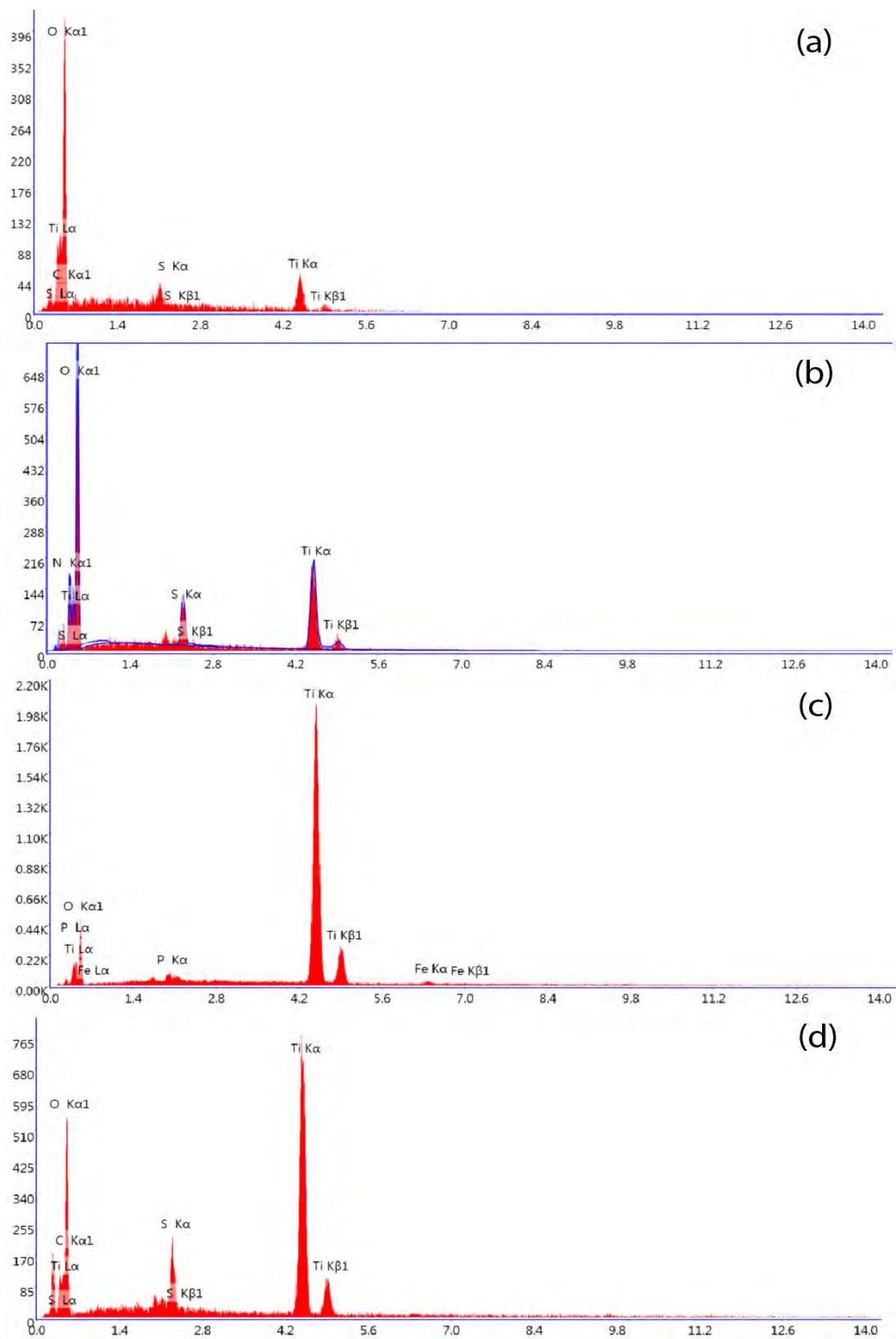


**Figure 4-10:** EDS patterns of samples with a. 45 min b. 60min c. 90min d. 135 min decomposition time



EDX report in Figure 4.10 and Table 4.8 showed that, the elemental ratio of oxygen and titanium decreases toward the ideal value with increasing decomposition time, gets closest for 90mins, then increases again for 135min. Impurity elements of Fe, Si, S, P was identified in all the samples. Among these, Fe is a rutile promoting element and the other three are rutile inhibiting elements, while they are in solid solution or added as additive during calcination [102]. Some of the inhibiting agents may resist the crystallite growth too. So, the change of impurity elements percentage and their effect on the anatase - rutile transformation and crystal growth during calcination results in the varying crystallite size and particle size (Fig. 4.9) and phase content (Fig. 4.6). The Fe content decreased with increasing decomposition time, which explains decreasing the peaks of rutile in the XRD Pattern (Fig. 4.6). From 45min to 60min, Fe decreased, but P, Si increased, lowering the rutile content and crystallite size. With increasing decomposition time, sudden decrease in all rutile inhibiting agents may be responsible for sudden growth of crystallite size and particle size too (Fig. 4.9; further increase of decomposition time resulted in increased P,S, Si content, lowering the particle size (Fig. 4.9). Here, in this study, yield and particle size of powder were important criteria, for which, the 60min retention time was selected as an optimum variable for this study.

**Table 4-8:** Elemental composition of upgraded samples (varying time)

Element	Average weight %			
	45min	60min	90min	135min
Ti	34.23	48.96	55.56	38.74
O	58.68	40.21	42.32	55.14
Fe	3.4	0.83	0.76	0.44
Si	0.67	0.66	0.34	0.58
P	1.8	1.92	0.96	0.94
S	1.23	7.42	0.07	4.16
Ratio (O/Ti) Ideal=0.6683	1.7143	0.8213	0.7617	1.4234
S+P+Si	3.7	10	1.37	5.69
Avg. Crystallite size	65.1nm	57.7nm	75.8nm	

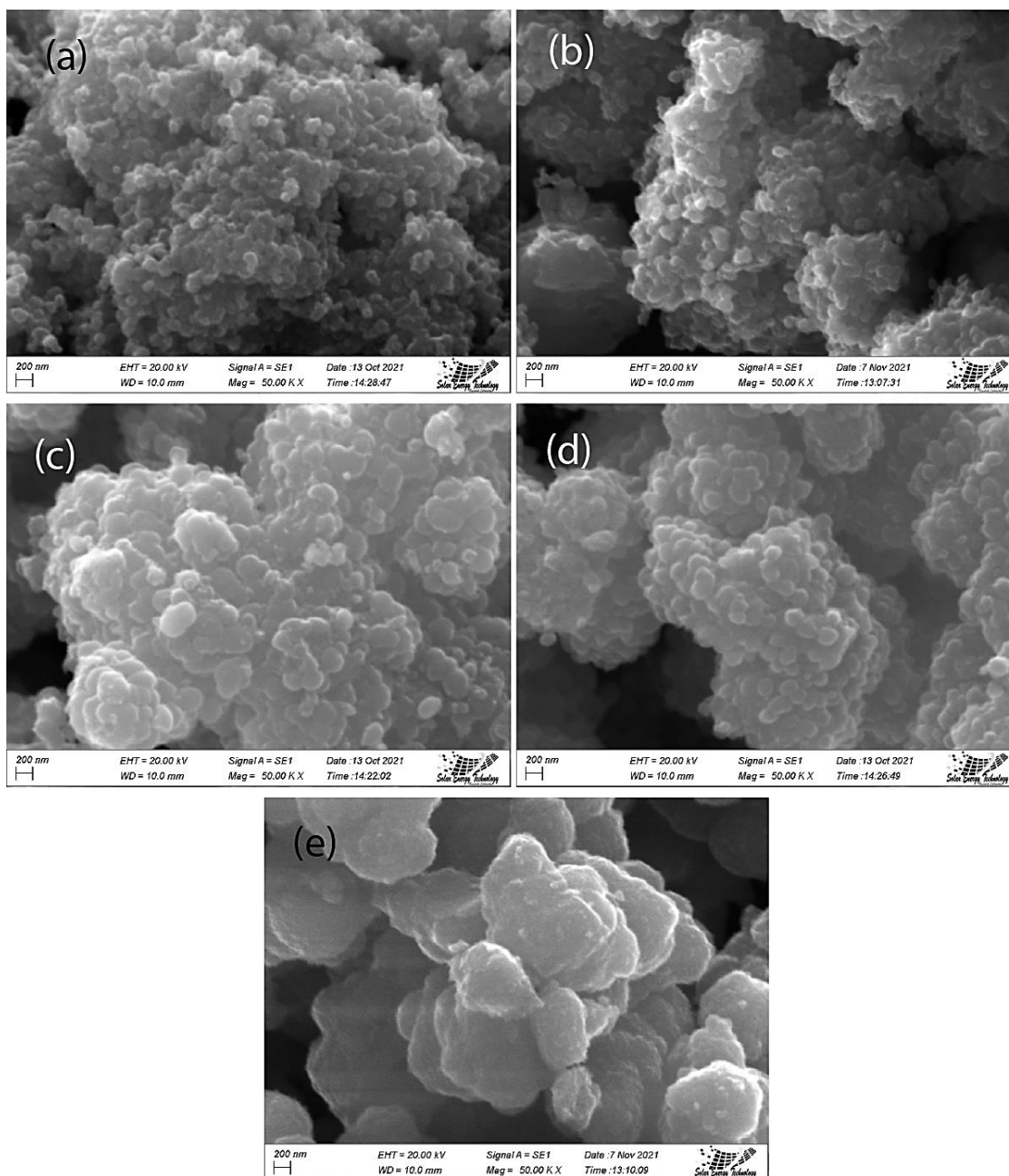


**Figure 4-11:** SEM image of powders extracted with varying decomposition  $\text{H}_2\text{SO}_4$  solution concentration a. 70%, b. 75%, c. 80%, d. 85%, e. 90% and annealed at  $500^\circ\text{C}$  after hydrolysis

Based on the observation of morphology and yield, further upgradation was performed with the condition of decomposition step of 60 minutes,  $150^\circ\text{C}$ . and after the extraction, the samples were annealed at  $500^\circ\text{C}$ . From the SEM image (Figure 4.11), large agglomeration of particles was observed for all the powder samples, from sample 1 to 5; and larger particle size were obtained for increasing concentration of sulfuric acid.

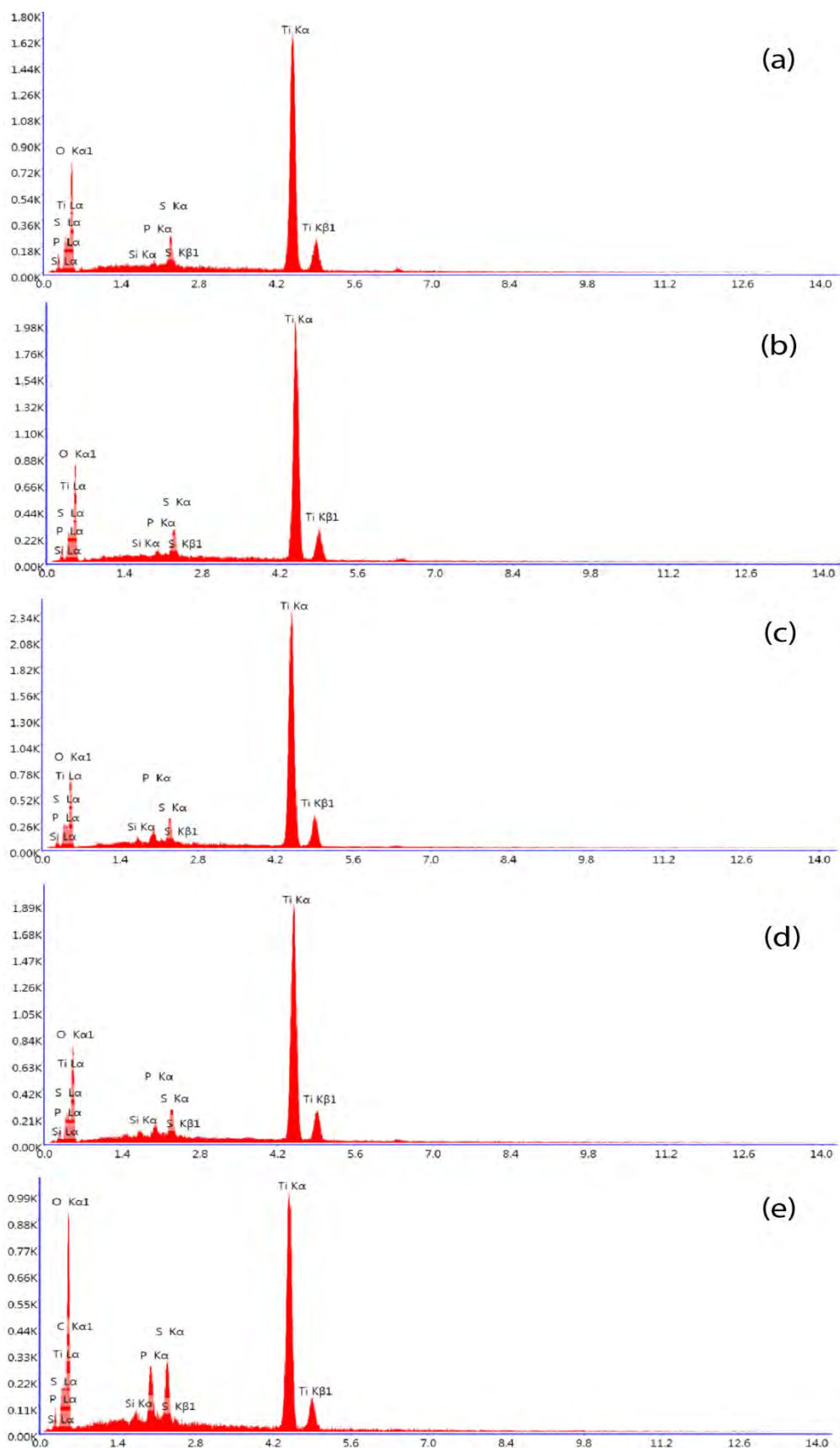


**Figure 4-12:** EDS patterns of a. Sample 1 (70%) b. Sample 2 (75%) c. Sample 3 (80%) d. Sample 4 (85%) e. Sample 5 (90%)

**Table 4-9:** Elemental composition of upgraded titania samples (varying acid concentrations)

<b>EDS (Wt%)</b>	<b>S1-70%</b>	<b>S2-75%</b>	<b>S3-80%</b>	<b>S4-85%</b>	<b>S5-90%</b>
<b>Ti%</b>	45.01	48.45	52.09	48.31	31.53
<b>O%</b>	51.82	48.34	43.39	47.42	59.83
<b>S%</b>	2.7	2.56	2.47	2.51	4.27
<b>P%</b>	0.39	0.55	1.62	1.47	3.82
<b>Si%</b>	0.08	0.1	0.43	0.29	0.55
<b>O/Ti Ratio (ideal=0.6683)</b>	1.151	0.998	0.833	0.982	1.898
<b>Total impurity</b>	3.17	3.21	4.52	4.27	8.64

From the EDS results in Figure 4.12 and Table 4.9, it can be observed that, S, P, Si are the impurity elements found. With increasing acid concentration, the impurity removal efficiency decreased. The oxygen-titanium elemental ratio was closest to the ideal value of 0.6683 for the sample obtained using 80% acid, the ratio going away from the ideal value for both side of changing acid concentration.

#### 4.3.4 Material Composition

Two of the annealed (900°C-4h) titania powders (decomposition condition-60min, 75%, 150°C and 60min-80%-160°C) were analyzed with XRF. The result obtained is tabulated below.

**Table 4-10** : Titania powder (annealed at 900°C) obtained through 60min decomposition time and [left] 75%  $H_2SO_4$  (150°C) and [right] 80%  $H_2SO_4$  (160°C) following Hydrolysis.

Analyte (75%, 150°C)	Mass%	Analyte (80%, 160°C)	Mass%
TiO <sub>2</sub>	98.42	TiO <sub>2</sub>	98.14
P <sub>2</sub> O <sub>5</sub>	1.25	P <sub>2</sub> O <sub>5</sub>	1.5
SiO <sub>2</sub>	0.26	SiO <sub>2</sub>	0.3
SO <sub>3</sub>	0.07	SO <sub>3</sub>	0.06

From Table 4.10, it can be observed that, impurity of iron, phosphorus, niobium, silicon etc. is detected in upgraded powders. The total titania content in both samples is ~ 98%, though from XRD [Figure 4.7] mixed rutile and anatase is present in right sample and mostly single phase is present in the left one.

The titania samples prepared with different concentration of decomposition solution were analyzed with XRF.

**Table 4-11**: Material composition of upgraded titania powder (varying acid concentrations)

Analyte	S1-70%	S2-75%	S3-80%	S4-85%	S5-90%
<b>TiO<sub>2</sub></b>	87.8165	87.654	85.6893	84.6393	82.6769
<b>SO<sub>3</sub></b>	11.4459	11.1609	10.364	12.341	8.5069
<b>P<sub>2</sub>O<sub>5</sub></b>	0.6918	1.1296	3.2333	2.8635	7.2675
<b>SiO<sub>2</sub></b>	0.0458	0.0554	0.7134	0.1562	1.5487

As observed from the XRF data in Table 4.11, with increasing the acid concentration, the selective leaching efficiency is decreased. Among the impurity of sulfur, phosphorus, and silicon, both P and Si content increased, and S decreased in the same pattern from sample 1 to 5 except for Sample 4. Reduced annealing temperature can also be a reason for presence of high amount of sulfur.

### 4.3.5 Optical Property

The UV-Vis diffuse reflectance of the 5 powder samples (prepared from varying acid concentration during decomposition during upgradation) was measured from 300nm to 850nm wavelength of light. This measurement was performed after hand grinding the powders for 2 hours using mortar and pestle.

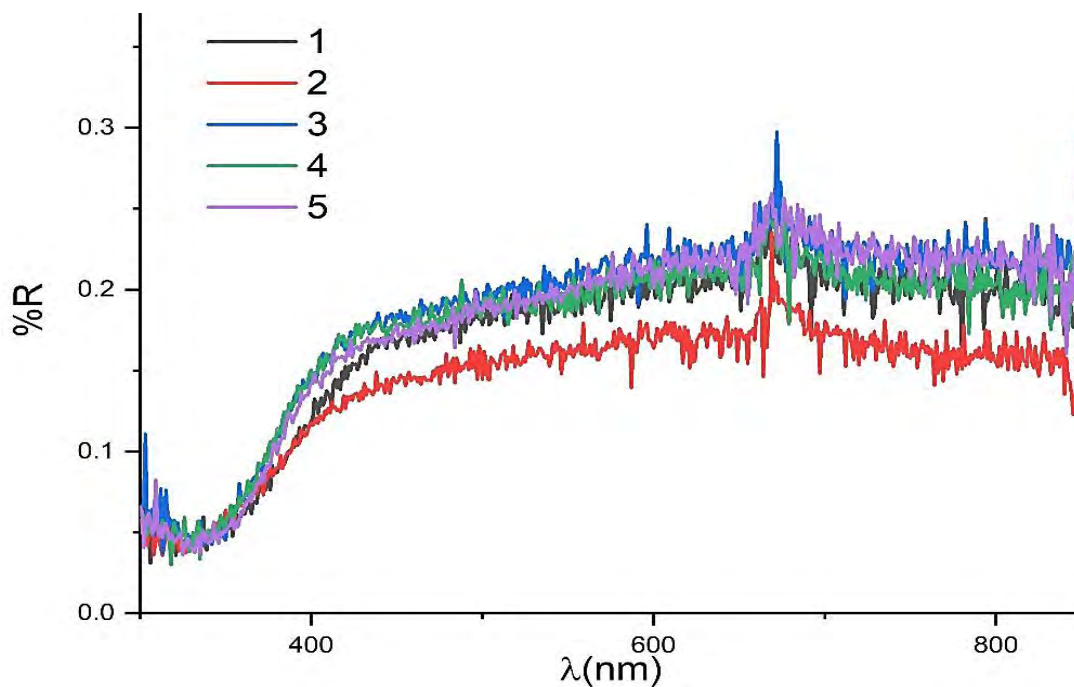


**Figure 4-13:** UV-Vis reflectance plot of powder sample 1,2,3,4,5 for 300-850nm wavelength range.

From the reflectance curve in Figure 4.13, it can be observed that, with increasing wavelength the reflectance increases, but in this range, it was maximum 0.3% in the visible range, and even lower in the UV range, which is a negligible fraction of the incident light energy.

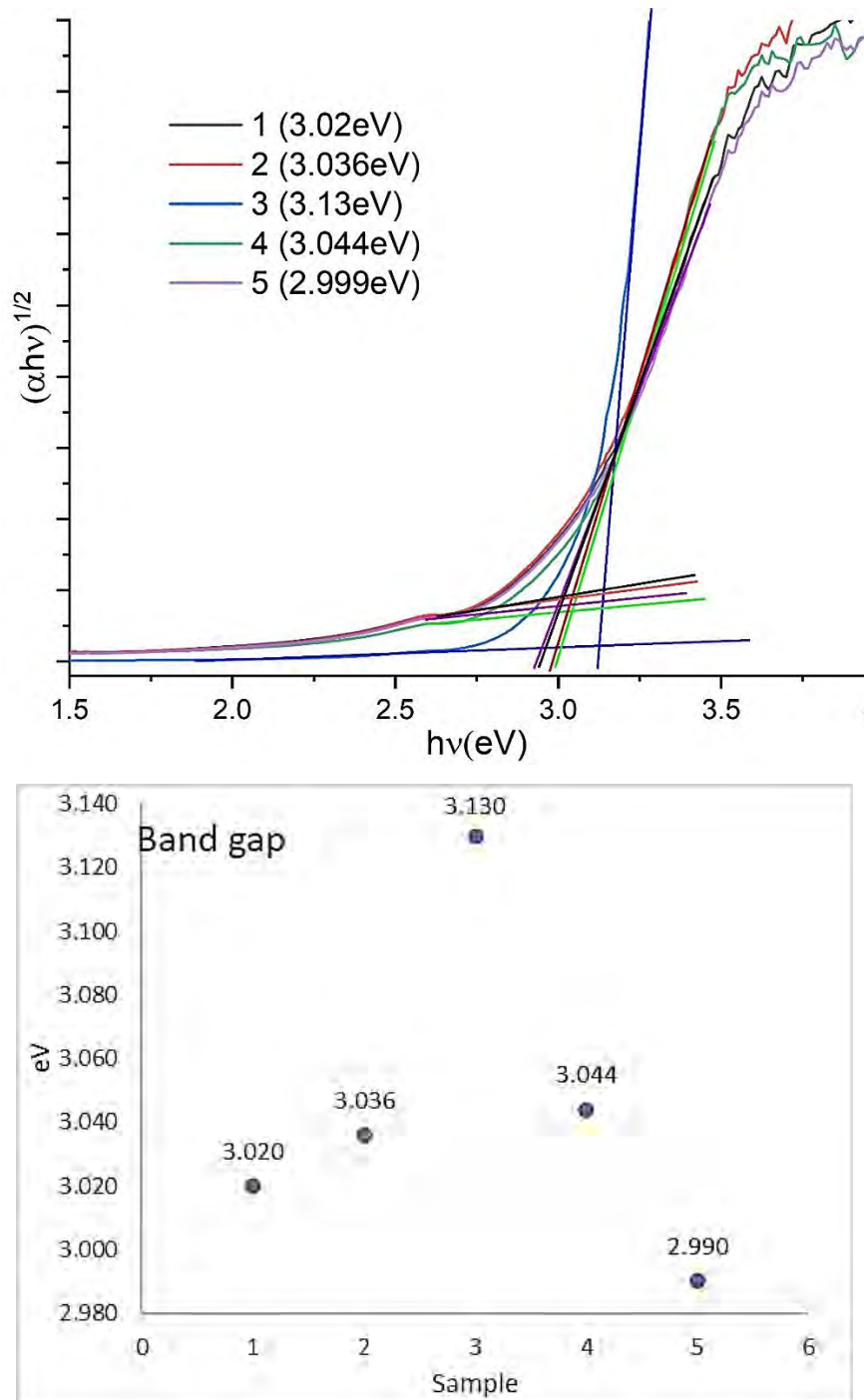


**Figure 4-14:** Transformed Reflectance Spectrum plot for Sample 1,2,3,4,5 using the Kubelka-Munk function

Plotting  $(\alpha h\nu)^2$  with respect to incident photon energy allows the calculation of semiconductor direct optical energy bandgap ( $E_g$ ) using the Tauc [118] relation.

$$(\alpha h\nu)^{1/\gamma} = B(h\nu - E_g) \quad (4.6)$$

where  $h$  is the Planck constant,  $\nu$  is the photon's frequency,  $E_g$  is the band gap energy, and  $B$  is a constant. The  $\gamma$  factor depends on the nature of the electron transition and is equal to 1/2 or 2 for the direct and indirect transition band gaps, respectively [119]. The band gap energy is usually determined from diffuse reflectance spectra.

Using the Kubelka-Munk function [120] (Eq. 4.7), Tauc [118] plot was drawn in Figure 4.14 for the samples considering the indirect inter-band transition; and to find the optical band gap, it was modified with baseline and fitted line to transformed reflectance spectrum [121].

$$F(R_{\infty}) = \frac{K}{S} = \frac{(1-R_{\infty})}{2R_{\infty}} \quad (4.7)$$

The band gap energy increased from sample 1 to 3, going closer to the ideal band gap value for anatase titania (3.2 eV) [122], then decreased again for sample 4 and 5. This change of band gap value can be attributed to the presence of impurity elements S [123], P [122], Si [104] which, when added as dopant in titanium dioxide, reduces the band gap energy and increases the response of titania in the visible spectrum. Several studies investigated the effect of non-metallic anion or metallic cation doped titanium dioxide to increase reduce the band gap energy so that absorption of visible spectrum too, ensuring utilization of higher %age of solar spectrum. The varying particle size of the samples can also be a reason. The annealing temperature of doped titania can also influence the visible light response [123].

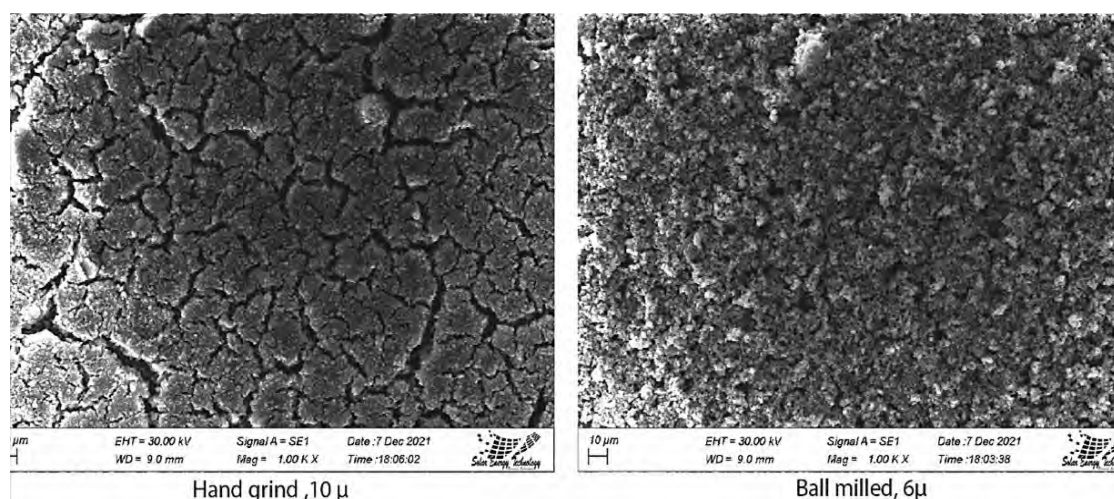
#### 4.4 Characterization of Titania Film (Morphology, thickness, electrical, optical)

##### 4.4.1 Morphology

For the application of photoanode of DSSC, the film should have large surface area, which can be achieved by controlling the particle size and pore size of the film. Nanosized particles and mesoporous morphology provide with the required high surface area, ensuring maximum dye loading and efficient charge transfer. For this reason, the desired morphology was the mesoporous nature of film for this study. In the characterization of powder samples, it was observed that, spherical nanoparticles formed large agglomeration.

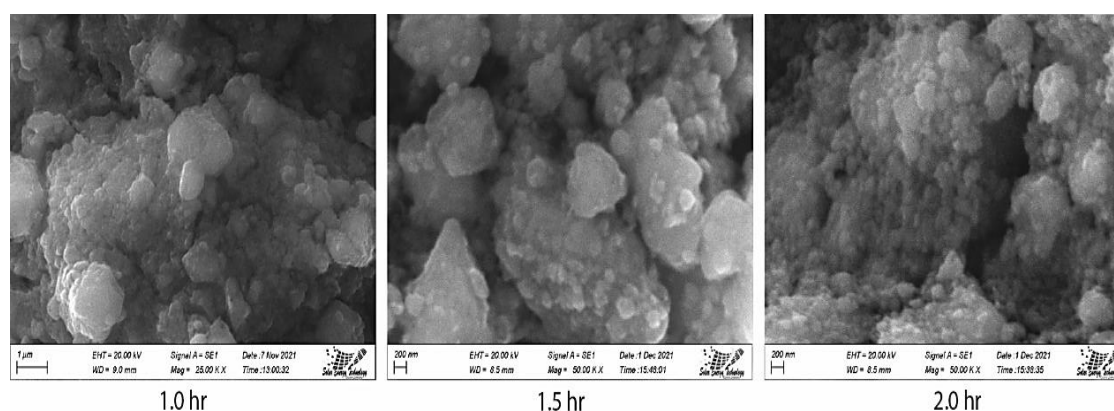


Initially two of the upgraded powders were used to select the suitable film preparation method providing with desired thickness and morphology.



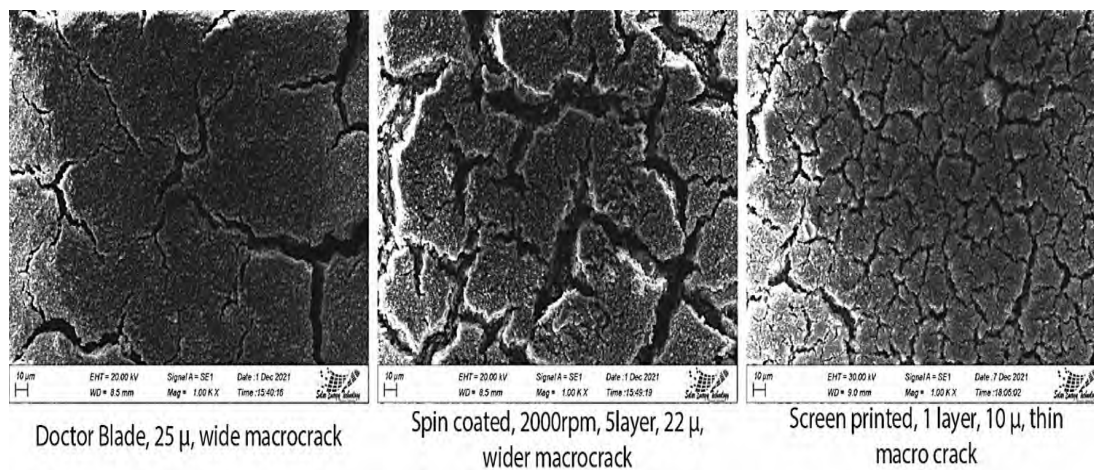
**Figure 4-15:** Influence of paste preparation method on film quality (Used powder sample's decomposition condition while upgrading-75%acid-150°C; hydrolysis; Method: screen printed; films annealed with 2.5°C/min)

Figure 4.15 shows effect of paste mixing and preparing method on the film quality. Same powder (prepared through 75%acid-150°C decomposition condition followed by hydrolysis) was used to prepare paste by mixing through ball milling or hand grinding with mortar-pestle. Paste grinded with ball mill makes better film with no macrocrack, while the hand grinded paste shows macrocrack in the film after annealing. But the paste recovery from large surface area balls is very low which causes waste of pastes.



**Figure 4-16:** Effect of hand grinding time on film morphology (Method: Doctor blade).

The Figure 4.16 shows the decrease of particle agglomeration size with hand grinding time. Further film preparation was preceded by 2hr grinding of powder.



**Figure 4-17:** Influence of film preparation method on film quality (Used powder sample's decomposition condition while upgrading-75%acid-150°C-60min; hydrolysis; hand grinding time-2h, films annealed with 2.5°C/min)

In Figure 4.17, morphology of films prepared by three methods using same powder shows that, single layer screen printed film gives better film with thinner-non substrate exposing cracks. Single layer doctor blade film is thick and contained wide macrocracks, while the spin coated layer shows intermediate thickness and even wider macrocracks.

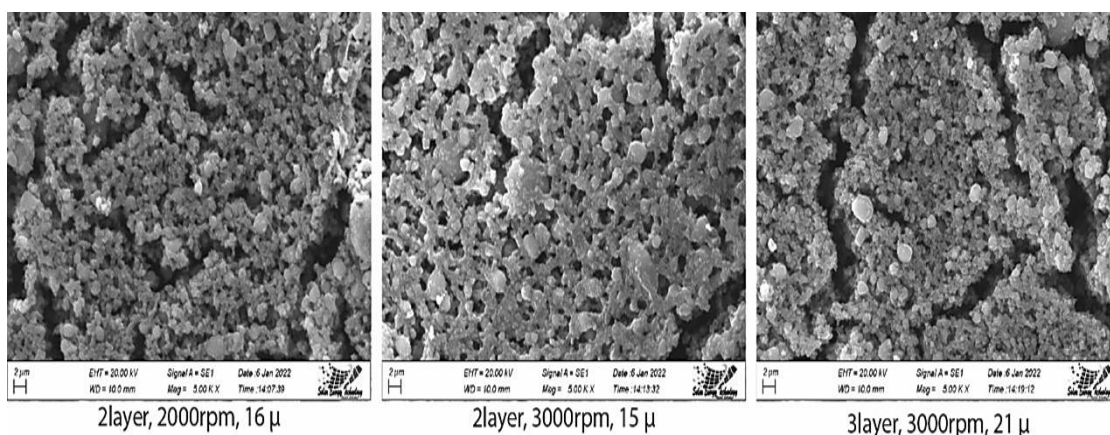


**Figure 4-18:** Influence of film thickness on film quality in spin coating (Used powder sample's decomposition condition while upgrading-80%acid-150°C; hydrolysis; hand grinding time-2h, films annealed with 2.5°C/min)

Figure 4.18 shows, for spin coated films, increasing the spin rate, and reducing layer number of films reduces the width of crack.



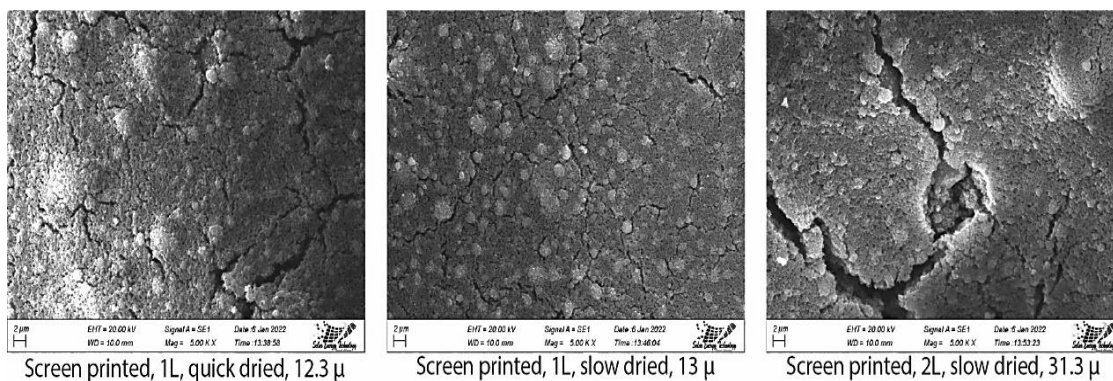


**Figure 4-19:** Influence of film thickness on film quality in screen printing (Used powder sample's decomposition condition while upgrading-80%acid-150°C-60min; hydrolysis; hand grinding time-2h, films annealed with 2.5°C/min)

Based on the morphology shown in Figure 4.19, in screen printing, with increasing layer wider cracks are observed with very high thickness. Also, quick drying of single layer film induces thin macrocracks. Slow drying of single layered screen printing was found to be favorable.

From the images shown in Figure 4.16 to Figure 4.19, it was observed that, films obtained through doctor's blade and spin coating show wide macrocracks while screen printed one shows thinner cracks. More uniform thickness was obtained for screen printing than doctor blade and spin coating. Films obtained by single layer screen print and double layer spin coating provided desired thickness (12-15 $\mu$ ). For longer annealing time, stability was higher for doctor blade and screen-printed film.

In Figure 4.20, morphology of the film samples prepared from powder sample 1, 2, 3, 4 and 5 is shown. Presence of very few agglomerations is observed due to the separation of softer agglomerates (those formed by capillary or weak surface forces) during hand grinding. Some hard agglomerates were still observed which may have formed due to the chemical bond formed during paste preparation. All the films had mesoporous nature and uniform distribution of pores.

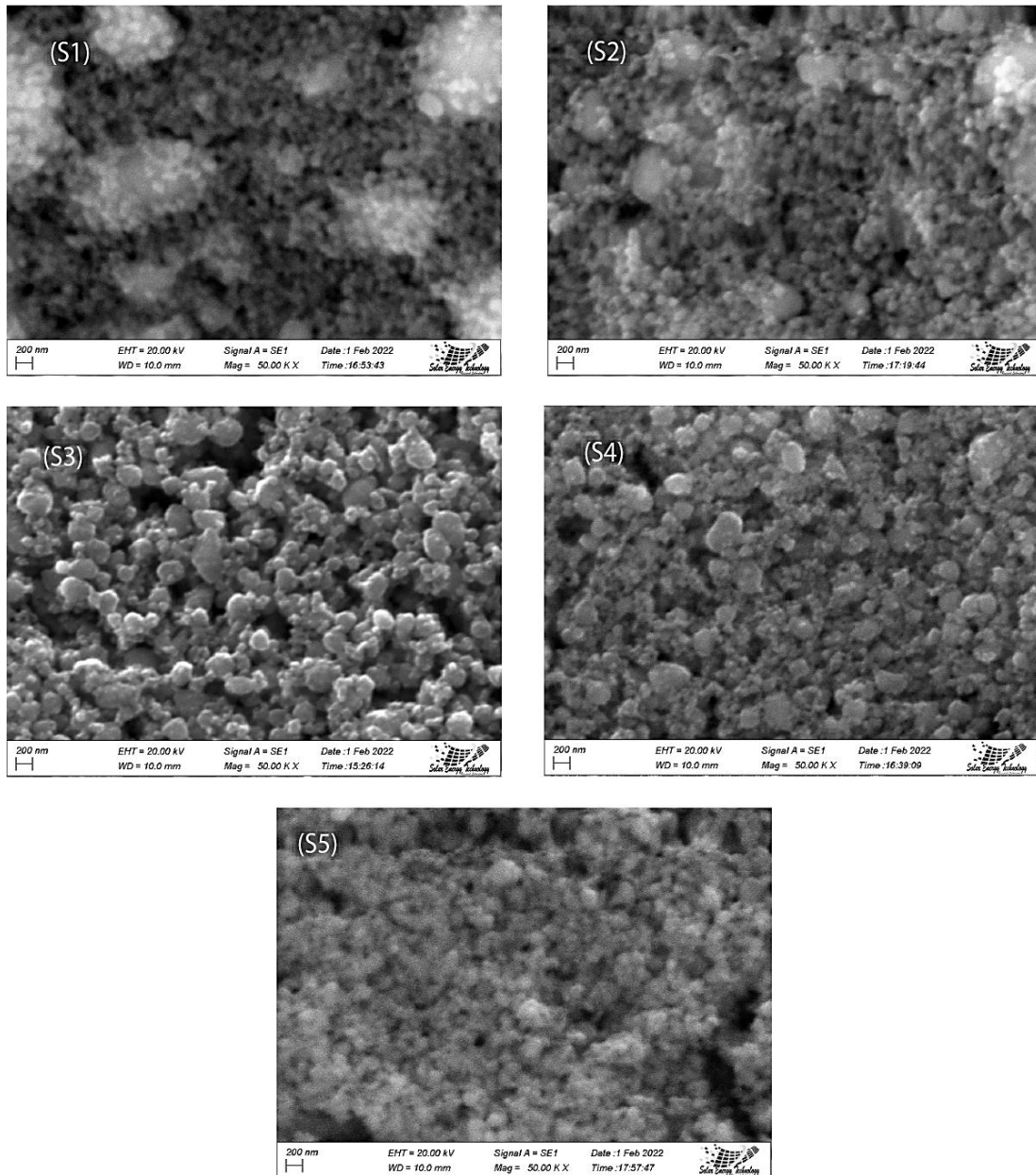


**Figure 4-20:** SEM image of Screen printed (single layered, slowly dried) and annealed films, paste prepared from powder samples 1, 2, 3, 4, 5 after 2h hand grinding

#### 4.4.2 Thickness Profile

The average thickness of the films prepared by sample 1 to 5 is shown in the Table 4.12.

**Table 4-12:** Thickness range of screen-printed film prepared by upgraded titania powders

Sample	No. of films	Thickness ( $\mu$ )
S1	18	12.0~14.0
S2	21	12.0~15.0
S3	15	11.5~13.5
S4	13	12.0~15.0
S5	13	12.5~16.0

The desired range of thickness for this study was  $12\mu$ - $15\mu$  ensuring no wide-substrate exposing macrocrack, so that tradeoff between maximum dye absorption and increasing electrical resistance could be possible. From the table, the average thickness was within the desired range for all samples, except for a few films of sample 5.

The film thickness and uniformity of surface along the whole layer was checked for 5 film samples as the film uniformity influences the reproducibility of cell efficiency. In Figure 4.21, the images show the 3D surface profile of 2mm-2mm area of films, thickness indicated by the color chart at the right of each image. The side view of the selected area is shown in the bottom side of each image. In terms of thickness uniformity of the selected samples, sample 1, 2 and 4 has more uniformity than sample 3 and 5 shows less uniform height distribution over the area.

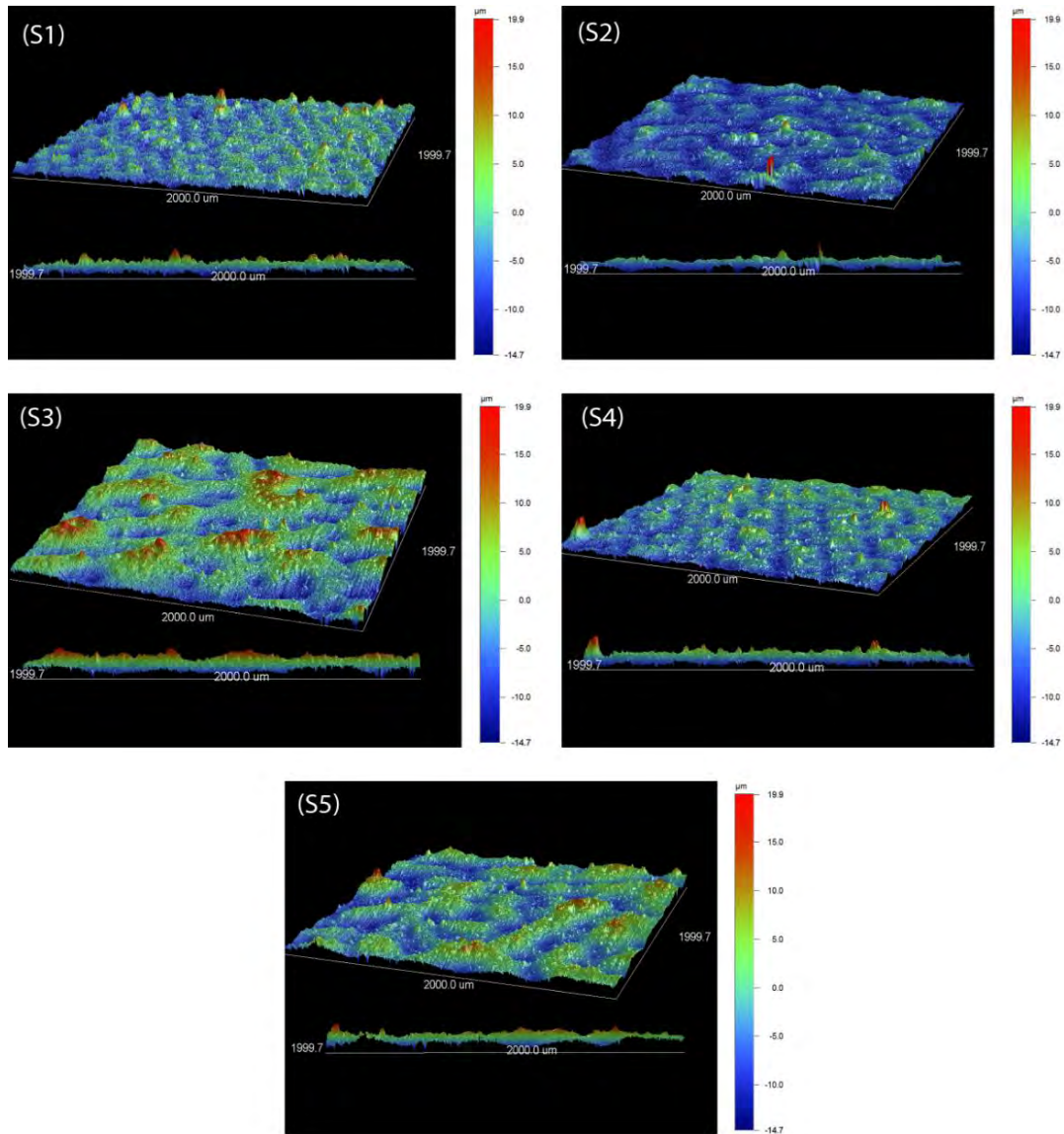


**Figure 4-21:** 3D mapping of screen-printed films prepared from sample 1, 2, 3, 4, 5

#### 4.4.3 Hall effect Measurement

For electrical properties of the films, the hall effect measurement was conducted. From Figure 4.22, it can be observed that, the average electrical resistance was in the order of  $10^8$  ohm.

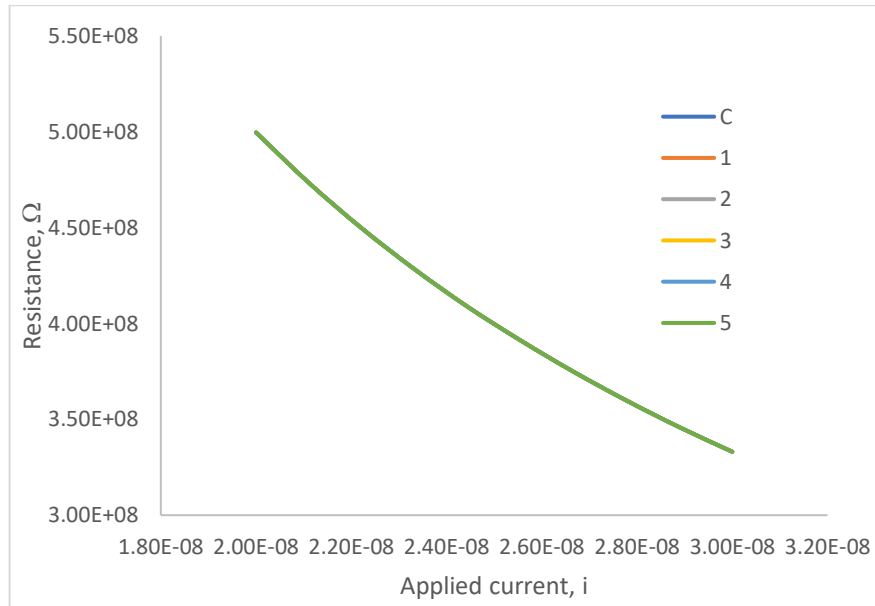


**Figure 4-22:** R-I curve of films from sample 1, 2, 3, 4, 5 and commercial powder

Table 4.13 shows that, carrier density of the sample was 3 orders of magnitude lower than other study. And carrier mobility was 1 order of magnitude lower than other similar investigations. Controlled doping with specific dopants (Nd) in titania can increase the carrier density, decrease the resistance[124][126]. Presence of impurity elements and the defect sites present in the film can also be responsible for lower mobility of carrier [124].

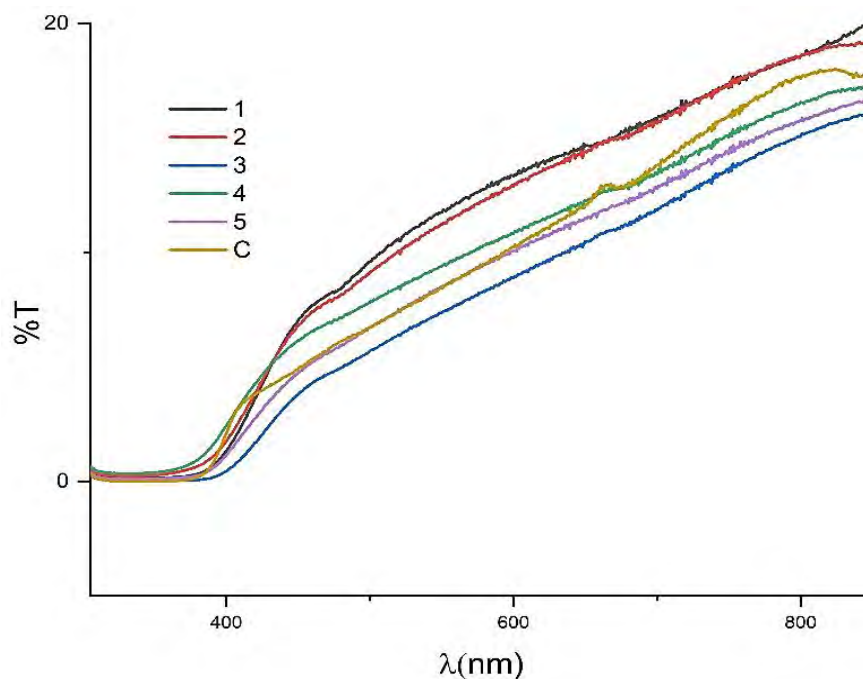
**Table 4-13:** Comparison of Electrical properties of sample with reference works

	Average value	Ref. works [124] [125]
Carrier Density ( $\text{cm}^{-3}$ )	$3.95 \times 10^{12}$	$10^{15}$ to $10^{17}$
Carrier Mobility ( $\text{cm}^2\text{V}^{-1}\text{s}^{-1}$ )	$1.97 \times 10^{-2}$	$10^{-1}$ to 1.5
Resistance ( $\Omega$ )	$10^8$	$10^7$
Average Hall coefficient ( $\text{cm}^3\text{C}^{-1}$ )	$1.58 \times 10^6$	



#### 4.4.4 Optical Property

With UV-Vis NIR, optical transmittance and absorbance of the films were measured from 300nm to 850nm, with a fresh soda-lime glass substrate used as a reference.



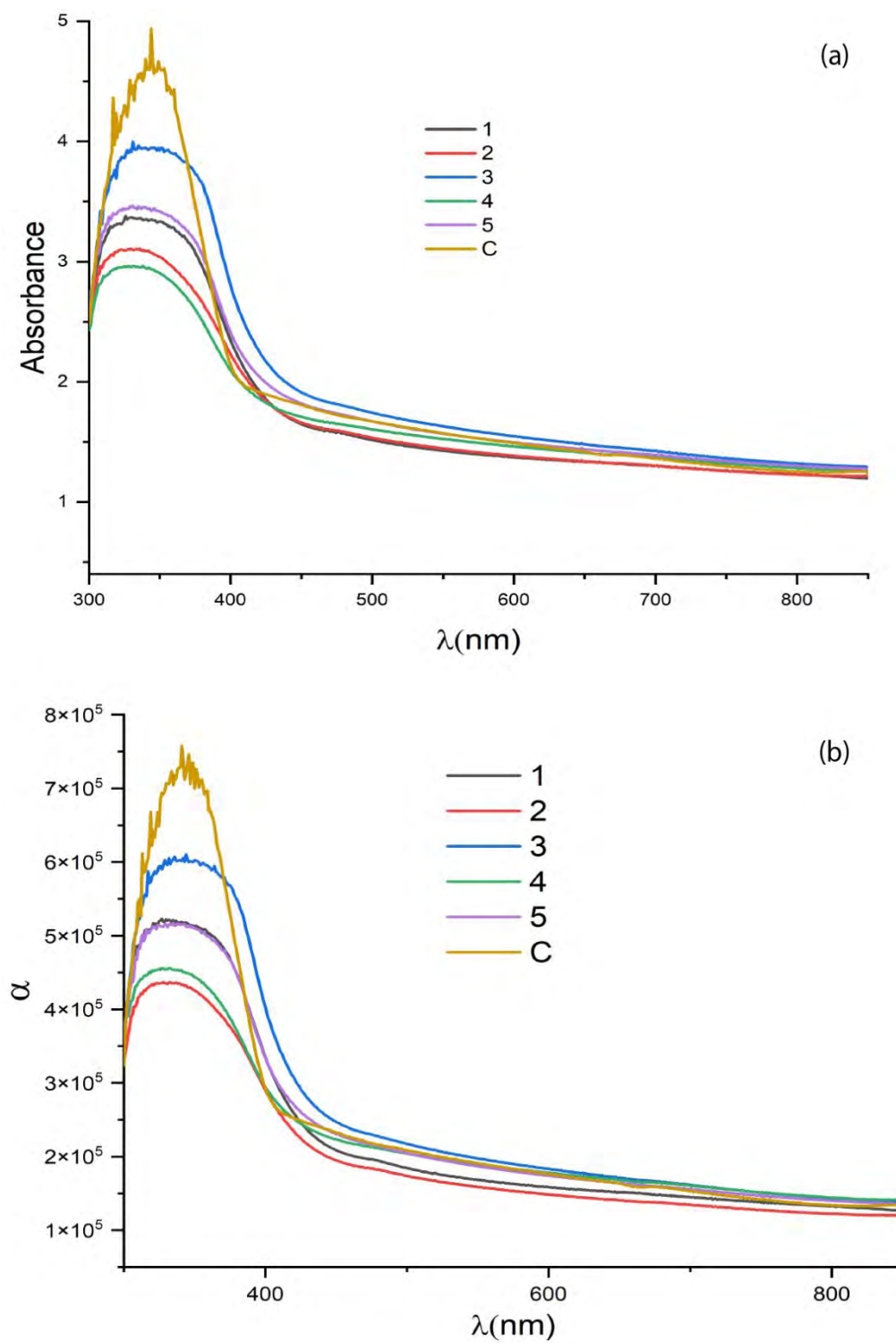
**Figure 4-23:** %Transmittance vs wavelength plot of film sample 1,2,3,4,5 and purchased anatase (C)

Figure 4.23 shows the change of transmittance with wavelength, and Table 4.14 shows the calculated average value of transmittance% in visible spectrum and whole range. Transmittance % of sample 3 and 5 in visible and whole spectrum was lower than that of the film prepared by purchased anatase (C- sigma Aldrich, >99%, 21nm particle size). Sample 3 has the lowest loss of incident light by transmittance.

**Table 4-14:** Average transmittance comparison of films of upgraded (S1, S2, S3, S4, S5) and commercial titania >99.5% TiO<sub>2</sub> P21nm (C)

	S1	S2	S3	S4	S5	C
<b>Average %T (400-700nm)</b>	10.90	10.61	7.10	9.15	8.15	8.51
<b>Average %T (250-850nm)</b>	14.49	14.02	10.82	12.51	11.69	12.44





**Figure 4-24:** (a) The UV-vis absorbance vs wavelength plot. (b) absorption coefficient vs wavelength of sample 1,2,3,4,5 and commercial anatase film (C).

**Table 4-15:** Average absorbance comparison of upgraded titania films

	<b>S1</b>	<b>S2</b>	<b>S3</b>	<b>S4</b>	<b>S5</b>	<b>C</b>
Average absorbance in visible range (400-700nm)	1.0036	1.0093	<b>1.2151</b>	1.0646	1.1340	1.1063
Average absorbance in (250-850nm)	1.156	1.121	<b>1.382</b>	1.142	1.261	1.327

From the Figure 4.24 and the tabulated average value (Table 4.15), it can be observed that, though in UV region the absorbance of the similar film of purchased anatase (C) is highest, but the response to visible spectrum is higher for sample 3 and 5, even higher than purchased one. Absorbance of sample 1,2 was well below than C, while sample 4 was closer.

#### **4.5 Characterization of Assembled Solar Cell**

Figure 4.25 shows the I-V and P-V curve of DSSC assembled with film of sample 1,2,3,4,5 and commercial anatase as photo anode.

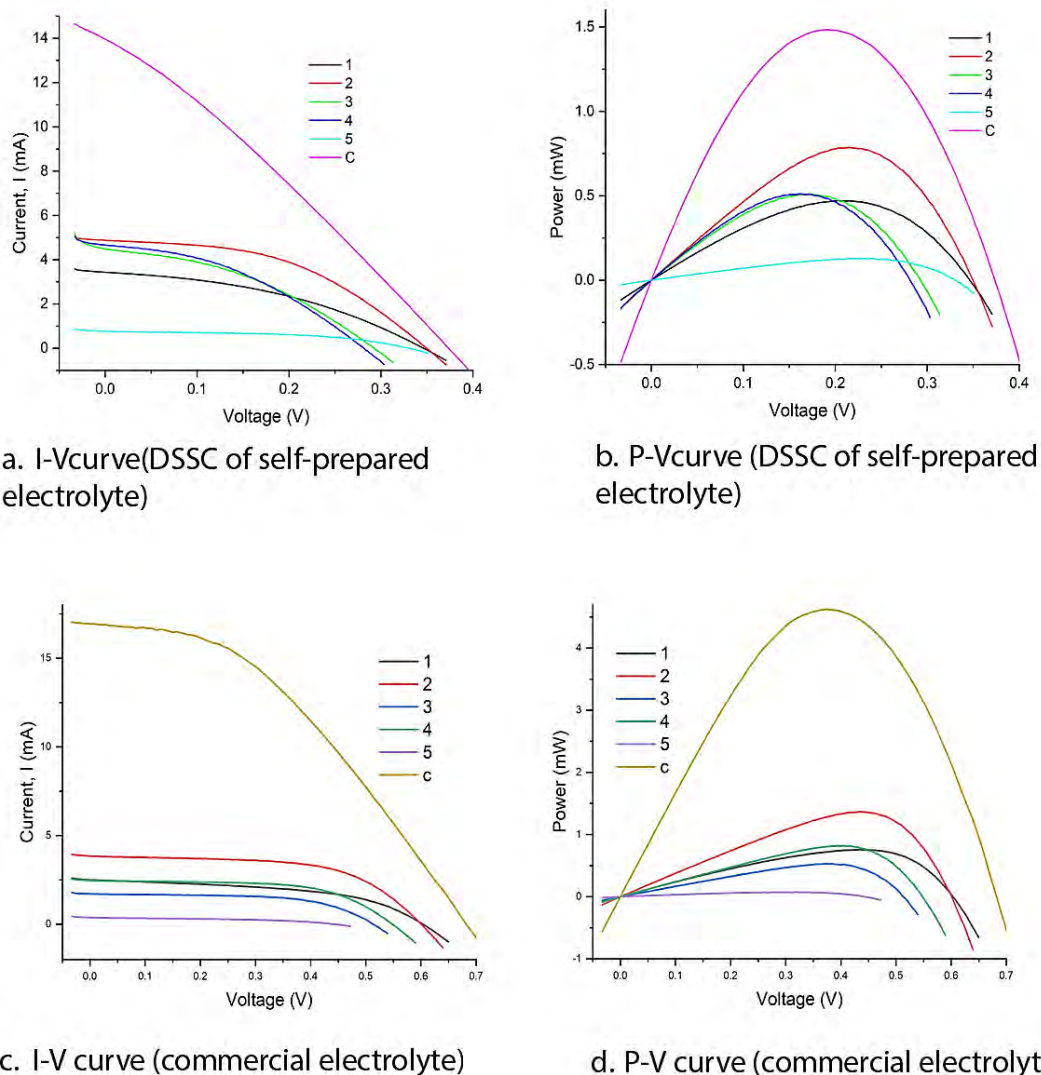


**Figure 4-25:** Performance variation of assembled DSSC (a,b) with self-prepared and (c,d) commercial electrolyte

**Table 4-16:** Experimental parameters of DSSC prepared using sample 1, 2, 3, 4, 5, commercial anatase film as photoanode and lab-prepared electrolyte, under AM 1.5 G Class AAA Solar Simulator.

	$J_{sc}$ (mA/cm <sup>2</sup> )	$V_{oc}$ (V)	$FF$	$\eta$ (%)
<b>S1</b>	1.526	0.3464	39.58772	0.209243
<b>S2</b>	2.167	0.3498	46.08474	0.349394
<b>S3</b>	1.994	0.2926	38.83182	0.226618
<b>S4</b>	2.074	0.2813	38.93811	0.227155
<b>S5</b>	0.342	0.3307	50.70605	0.057401
<b>C</b>	6.205	0.3736	28.45028	0.659449

The active area of all sample photoanodes were  $2.25\text{cm}^2$ . In table,  $J_{sc}$  is short circuit current density,  $V_{oc}$  is open circuit voltage, FF is the fill factor and  $\eta$  is photon conversion efficiency.

**Table 4-17:** Experimental parameters of DSSC prepared using sample 1, 2, 3, 4, 5, commercial anatase film as photoanode and commercial electrolyte, under AM 1.5 G Class AAA Solar Simulator.

	$J_{sc} (mA/cm^2)$	$V_{oc} (V)$	$FF$	$\eta (%)$
<b>S1</b>	1.112	0.6035	50.23817	0.33726
<b>S2</b>	1.71	0.6007	59.12763	0.607502
<b>S3</b>	0.76	0.5132	60.47481	0.235817
<b>S4</b>	1.097	0.5481	60.51499	0.364018
<b>S5</b>	0.167	0.4412	44.2718	0.032551
<b>C</b>	7.53	0.6823	40.00586	2.055245

As we can see from Table 4.16 and Table 4.17, highest efficiency was achieved for sample 2, its conversion efficiency is  $\sim 53\%$  of that of the commercial anatase film for the lab-prepared electrolyte. However, response to commercial electrolyte was higher for the commercial anatase film compared to the response of extracted powder sample films. For this batch, sample 2 (S-2) showed highest efficiency among the five samples, which is  $\sim 30\%$  of that of commercial one. As the cell efficiency is influenced by numerous factors including film composition (impurity element) and structure (well crystallinity), film thickness and mesoporous morphology, uniformity, efficient charge transfer, defects in film, efficient dye loading etc., the results shown in Table 4.16 and 4.17 cannot be directly related to the upgradation efficiency of titania. Rather it supports the possibility of effective application of extracted titania in solar cell photoanode.

## 5. CONCLUSION

### 5.1 Findings of this Work

To summarize the findings of the present research work, the whole work can be divided into three steps.

1. Characterization and Upgradation of sand
2. Preparation of mesoporous film with upgraded titania and purchased anatase (Particle size 21nm, Sigma-Aldrich, >99%)
3. Fabrication of dye sensitized solar cell using titania films as anode.

#### 5.1.1 Characterization and upgradation of sand

- >80% of the particles of as-received sand were distributed within 100-200 $\mu$ , became distributed more widely after 5minutes mechanical milling. After 15mins milling, 68% of particles became tightly distributed in 53-75 $\mu$ .
- Presence of rutile, garnet, silica, hornblende, zircon, monazite, tourmaline, chloritoid, staurolite were identified. Based on composition, total 21.4% of TiO<sub>2</sub> is present in the sample, distributed in rutile (15-25%) and ilmenite (22%).
- In the upgradation route of *HCl leaching-H<sub>2</sub>SO<sub>4</sub> decomposition- water leaching- repeated condensation & dilution- drying-calcination*, variation of acid decomposition time effects the single or mixed phase formation of rutile and titania, also the elemental ratio of the product. For this route 90min decomposed sample resulted in upgradation up to 98% TiO<sub>2</sub>.
- In the upgradation route of *HCl leaching-H<sub>2</sub>SO<sub>4</sub> decomposition- water leaching- hydrolysis- drying-calcination*, change of acid concentration and temperature of decomposition influenced the purity and mixed rutile-titania formation. For this route extraction up to 98.4% was possible for 900°C calcining temperatures and up to 87.8% was obtained for 500°C calcining temperatures. Among the 500°C calcined samples prepared by varying acid concentration, sample from 80% acid solution gave better crystallographic properties and closer to ideal-elemental ratio, though highest purity was

obtained for the sample from 70% acid solution. Particle size and agglomerate size after annealing increased with increasing acid concentration.

- Based on the optical properties, band gap up to 3.18eV was obtained for sample 3 (80% acid decomposition).

### **5.1.2 Preparation of mesoporous film with upgraded and purchased anatase**

- Among doctor blade, spin coating and screen-printing film preparation method, screen printed film showed better film uniformity, stability. Single layer screen printed film, slowly dried, and annealed after preparation gave uniform, mesoporous and least crack containing morphology.
- The thickness of the screen- printed films ranged from 12- 16 $\mu$ , more uniform thickness and smaller aggregate achieved for sample 1,2,4.
- Film sample was measured to have carrier density of  $10^{12}/\text{cm}^3$  and resistance of about  $10^8$  ohms.
- Based on the optical properties, response to visible spectrum obtained for sample 3 and 5 was higher than film of purchased anatase.

### **5.1.3 Fabrication of dye sensitized solar cell**

- To find the effectiveness of the films of upgraded titania as solar cell photoanode, a simple DSSC cell was fabricated only containing the basic components of the state-of-the-art high efficiency DSSC. Maximum photoconversion efficiency was achieved about 53% of that of the film of purchased anatase. Use of commercial electrolyte instead of self-prepared electrolyte increased the efficiency of each sample films. For both cases, the maximum efficiency was obtained for sample 2.
- In conclusion, the upgraded titania from local beach sand sample has very good potential to be used in applications of solar cell electrode.

## **5.2 Scope for Further Investigation**

The aim of this study was to upgrade titania in local sand and to find its potential to be used as solar cell electrode. Based on the conducted characterizations, the work

suggests a lower energy intensive, environment friendly upgradation route of the sand, and high potential of the extracted titania to be effectively used in solar cell application. The endeavor should be continued to increase purity level of titania.

The following recommendations may be suggested.

- a. In this work, 60min decomposition time was selected for preparing samples used in DSSC. Further experiments may be performed to optimize the sulfuric acid decomposition time.
- b. The decomposition temperature used in this work was only 150°C, which can be varied up to 180°C to find optimum temperature.
- c. This work selected 4-hour long hydrolysis to ensure complete hydrolysis. The time of hydrolysis can be optimized to ensure complete hydrolysis while preventing the ripening of the titania particles.
- d. In this work, the 500°C calcined samples (lower crystallinity and higher impurity) were used for film preparation and DSSC fabrication. Calcination temperature of the extracted powder can be optimized to ensure high crystallinity with high surface area.

## REFERENCES

- [1] J. Gambogi, "Titanium mineral concentrates," *U.S. Geol. Surv. Miner. Commod. Summ.*, no. 703, 2022, [Online]. Available: <https://pubs.usgs.gov/periodicals/mcs2022/mcs2022-titanium-minerals.pdf>.
- [2] E. Akon, "Mineralogy, geochemistry and economic potentialities of heavy mineral sand resources of Bangladesh," *J. Nepal Geol. Soc.*, vol. 59, pp. 1–8, 2019, doi: 10.3126/jngs.v59i0.24981.
- [3] W. Hoecker, "Process for the production of synthetic rutile," 1997.
- [4] H. N. Sinha, "Murso Process for Producing Rutile Substitute," in *Titanium Science and Technology*, R. I. Jaffee and H. M. Burte, Eds. Boston, MA.: Springer, 1973, pp. 233–245.
- [5] M. Robinson, F. Clamp, D. Aberdeen, and D. Barry Mobbs, "Beneficiation of Ilmenite Ores," 3897537, 1975.
- [6] E. A. Walpole and D. Winter, "The Austpac ERMS and EARS Processes for the Manufacture of High-Grade Synthetic Rutile by the Hydrochloric Acid Leaching of Ilmenite," in *International Conference on the Practice and Theory of Chloride/Metal Interaction*, 2002, no. October 2002, pp. 1–14, [Online]. Available: [https://www.austpacresources.com/pdfs/techpub/EJW\\_Paper\\_Oct\\_2002.pdf](https://www.austpacresources.com/pdfs/techpub/EJW_Paper_Oct_2002.pdf).
- [7] J. A. Kahn, "Non-Rutile Feedstocks for the Production of Titanium," *JOM*, vol. 36, pp. 33–38, 1984, doi: <https://doi.org/10.1007/BF03338498>.
- [8] S. Kataoka and S. Yamada, "Acid leaching upgrades ilmenite to synthetic rutile," *Chem. Eng.*, vol. 80, no. 7, pp. 92–93, 1973, [Online]. Available: [https://www.researchgate.net/publication/284686886\\_Acid\\_leaching\\_upgrades\\_ilmenite\\_to\\_synthetic\\_rutile/stats](https://www.researchgate.net/publication/284686886_Acid_leaching_upgrades_ilmenite_to_synthetic_rutile/stats).
- [9] T. H. Nguyen and M. S. Lee, "A review on the recovery of titanium dioxide from Ilmenite ores by direct leaching technologies," *Miner. Process. Extr. Metall. Rev.*, vol. 00, no. 00, pp. 1–17, 2018, doi: 10.1080/08827508.2018.1502668.
- [10] E. G. Roche, A. D. Stuart, and P. E. Grazier, "Production of Titania,"



WO2004035841 A1, 2004.

- [11] E. G. Roche, A. D. Stuart, P. E. Grazier, and S. Nicholson, "Production of Titania," WO2005038060-A1, 2005.
- [12] A. D. Stuart, J. A. Lawson, C. B. Ward, and H. Peng, "A sulphate process," WO Patent 2010034083-A1, 2010.
- [13] D. Verhulst, B. Sabacky, T. Spitler, and W. Duyvesteyn, "The Altair TiO<sub>2</sub> pigment process and its extension into the field of nanomaterials," *CIM Bull.*, vol. 95, no. 1065, pp. 89–94, 2002, [Online]. Available: [https://www.researchgate.net/publication/283878971\\_The\\_Altair\\_TiO<sub>2</sub>\\_pigment\\_process\\_and\\_its\\_extension\\_into\\_the\\_field\\_of\\_nanomaterials](https://www.researchgate.net/publication/283878971_The_Altair_TiO2_pigment_process_and_its_extension_into_the_field_of_nanomaterials).
- [14] D. Verhulst, B. Sabacky, T. Spitler, and W. Duyvesteyn, "New developments in the Altair hydrochloride TiO<sub>2</sub> pigment process," *Hydrometallurgy 2003, 5th Int. Conf. Honor Profr. Ritchie, Vancouver, August 2003*, vol. 1, pp. 565–575, 2003, [Online]. Available: [https://www.researchgate.net/publication/237307472\\_New\\_developments\\_in\\_the\\_Altair\\_TiO<sub>2</sub>\\_hydrochloride\\_pigment\\_process](https://www.researchgate.net/publication/237307472_New_developments_in_the_Altair_TiO2_hydrochloride_pigment_process).
- [15] A. A. Nayl, N. S. Awwad, and H. F. Aly, "Kinetics of acid leaching of ilmenite decomposed by KOH. Part 2. Leaching by H<sub>2</sub>SO<sub>4</sub> and C<sub>2</sub>H<sub>2</sub>O<sub>4</sub>," *J. Hazard. Mater.*, vol. 168, pp. 793–799, 2009, doi: 10.1016/j.jhazmat.2009.02.076.
- [16] G. Editorial, "Titanium and iron dissolutions from ilmenite by acid leaching and microbiological oxidation techniques," *ASIA-PACIFIC J. Chem. Eng.*, vol. 8, pp. 323–330, 2013, doi: 10.1002/apj.1663.
- [17] C. Sima\*, W. Waldhauser, J. Lackner, M. Kahn, and A. M. , I. Nicolae, C. Viespe, C. Grigoriu, "Properties of TiO<sub>2</sub> thin films deposited by RF magnetron sputtering," *J. Optoelectron. Adv. Mater.*, vol. 9, no. 5, pp. 1446–1449, 2007.
- [18] X.-S. Zhou, Y.-H. Lin, and B. Li, "Processing and characterization of TiO<sub>2</sub> film prepared on glass via pulsed laser deposition," *J. Phys. D. Appl. Phys.*, vol. 39, no. 3, p. 558, 2006, doi: <https://doi.org/10.1088/0022-3727/39/3/021>.
- [19] L. Bedikyan, S. Zakhariyev, and M. Zakhariyeva, "Titanium dioxide thin films:

- Preparation and optical properties,” *J. Chem. Technol. Metall.*, vol. 48, no. 6, pp. 555–558, 2013.
- [20] S. K. Kim, K. M. Kim, D. S. Jeong, and W. Jeon, “Titanium dioxide thin films for next-generation memory devices,” *J. Mater. Res.*, vol. 28, no. 3, pp. 313–325, 2012, doi: 10.1557/jmr.2012.231.
- [21] Negishi, N., K. Takeuchi, and T. Ibusuki, “Preparation of the TiO<sub>2</sub> Thin Film Photocatalyst by the Dip-Coating Process,” *J. Sol-Gel Sci. Technol.*, vol. 13, pp. 691–694, 1998, doi: <https://doi.org/10.1023/A:1008640905357>.
- [22] A. Verma, A. Basu, and A. K. Bakhshi, “Structural, optical and electrochemical properties of sol–gel derived TiO<sub>2</sub> films: Annealing effects,” *Solid State Ionics*, vol. 176, no. 29–30, pp. 2285–2295, 2005, doi: <https://doi.org/10.1016/j.ssi.2005.06.011>.
- [23] Z. Dongshe, I. Seigo, W. Yuji, K. Takayuki, and Y. Shozo, “Nanocrystalline TiO<sub>2</sub> Electrodes Prepared by Water-Medium Screen Printing Technique,” *Chem. Lett.*, vol. 30, no. 10, pp. 1042–1043, 2001, doi: <https://doi.org/10.1246/cl.2001.1042>.
- [24] H. Zhang, W. Wang, H. Liu, R. Wang, Y. Chen, and Z. Wang, “Effects of TiO<sub>2</sub> film thickness on photovoltaic properties of dye-sensitized solar cell and its enhanced performance by graphene combination,” *Mater. Res. Bull.*, vol. 49, no. 1, pp. 126–131, 2014, doi: 10.1016/j.materresbull.2013.08.058.
- [25] S. Santhaveesuk, “Synthesis TiO<sub>2</sub> with doctor blade technique for dye sensitized solar cell,” 2014, [Online]. Available: <http://iseec2014.udru.ac.th>.
- [26] T. P. Huynh, T. T. Hoanq, P. H. Nguyen, T. N. Tran, and T. V. Nguyen, “Preparation of TiO<sub>2</sub> thin film using modified doctor-blade method for improvement of dye-sensitized solar cell,” in *Conference Record of the IEEE Photovoltaic Specialists Conference*, 2009, pp. 002168–002171, doi: 10.1109/PVSC.2009.5411405.
- [27] N. Ali *et al.*, “Advances in nanostructured thin film materials for solar cell applications,” *Renew. Sustain. Energy Rev.*, vol. 59, pp. 726–737, 2016, doi: 10.1016/j.rser.2015.12.268.

- [28] B. O'Regan and M. Grätzel, "A low-cost, high-efficiency solar cell based on dye-sensitized colloidal TiO<sub>2</sub> film," *Nature*, vol. 368, pp. 444–446, 1991.
- [29] C. S. Karthikeyan, M. Thelakkat, and M. Willert-Porada, "Different mesoporous titania films for solid-state dye sensitised solar cells," *Thin Solid Films*, vol. 511–512, pp. 187–194, 2006, doi: 10.1016/j.tsf.2005.12.152.
- [30] A. Hagfeldt, G. Boschloo, L. Sun, L. Kloo, and H. Pettersson, "Dye-Sensitized Solar Cells," *Chem. Rev.*, vol. 110, no. 11, pp. 6595–6663, 2010, doi: 10.1021/cr900356p.
- [31] W. Zhang, Z. Zhu, and C. Y. Cheng, "A literature review of titanium metallurgical processes," *Hydrometallurgy*, vol. 108, pp. 177–188, 2011, doi: 10.1016/j.hydromet.2011.04.005.
- [32] J. Gambogi, "Titanium Mineral Concentrates," *U.S. Geol. Surv. Miner. Commod. Summ.*, no. 703, 2020, [Online]. Available: <https://www.usgs.gov/centers/national-minerals-information-center/titanium-statistics-and-information>.
- [33] J. Gambogi, "Titanium and titanium dioxide," *U.S. Geol. Surv. Mineral Commod. Summ.*, no. 703, 2022, [Online]. Available: <https://pubs.usgs.gov/periodicals/mcs2022/mcs2022-titanium.pdf>.
- [34] H. Zhang and J. F. Banfield, "Structural characteristics and mechanical and thermodynamic properties of nanocrystalline TiO<sub>2</sub>," *Chem. Rev.*, vol. 114, no. 19, pp. 9613–9644, 2014, doi: 10.1021/cr500072j.
- [35] N. Rahimi, R. A. Pax, and E. M. A. Gray, "Review of functional titanium oxides. I: TiO<sub>2</sub> and its modifications," *Prog. Solid State Chem.*, vol. 44, no. 3, pp. 86–105, 2016, doi: 10.1016/j.progsolidstchem.2016.07.002.
- [36] R. A. Young, *The Rietveld Method*. Oxford University Press, 1995.
- [37] R. G. Breckenridge and W. R. Hosler, "Electrical properties of titanium dioxide semiconductors," *Phys. Rev.*, vol. 91, no. 4, pp. 793–802, 1953, doi: 10.1103/PhysRev.91.793.
- [38] G. M. Bedinger, "2017 Minerals Yearbook," 2017.

- [39] N. A. Jabit, *Chemical and Electrochemical Leaching Studies Of Synthetic And Natural Ilmenite In Hydrochloric Acid Solutions*. 2017.
- [40] S. M. Gupta and M. Tripathi, "A review of TiO<sub>2</sub> nanoparticles," *Chinese Sci. Bull.*, vol. 56, no. 16, pp. 1639–1657, 2011, doi: 10.1007/s11434-011-4476-1.
- [41] H. Han and R. Bai, "Buoyant photocatalyst with greatly enhanced visible-light activity prepared through a low temperature hydrothermal method," *Ind. Eng. Chem. Res.*, vol. 48, no. 6, pp. 2891–2898, 2009, doi: 10.1021/ie801362a.
- [42] M. R. Hoffmann, S. T. Martin, W. Choi, and D. W. Bahnemann, "Environmental Applications of Semiconductor Photocatalysis," *Chem. Rev.*, vol. 95, pp. 69–96, 1995, doi: 10.1021/cr00033a004.
- [43] A. Mills and S. LeHunte, "An overview of semiconductor photocatalysis," *J. Photochem. Photobiol. A Chem*, vol. 108, pp. 1–35, 1997, doi: 10.1126/science.12.296.346-a.
- [44] I. P. Parkin and R. G. Palgrave, "Self-cleaning coatings," *J. Mater. Chem.*, vol. 15, no. 15, pp. 1689–1695, 2005, doi: 10.1039/b412803f.
- [45] A. Mills, S. Hodgen, and S. K. Lee, "Self-cleaning titania films: An overview of direct, lateral and remote photo-oxidation processes," *Res. Chem. Intermed.*, vol. 31, no. 4–6, pp. 295–308, 2005, doi: 10.1163/1568567053956644.
- [46] Y. Sekiguchi *et al.*, "Self-sterilizing catheters with titanium dioxide photocatalyst thin films for clean intermittent catheterization: Basis and study of clinical use," *Int. J. Urol.*, vol. 14, pp. 426–430, 2007, doi: 10.1111/j.1442-2042.2007.01743.x.
- [47] B. Xin, Z. Ren, P. Wang, J. Liu, L. Jing, and H. Fu, "Study on the mechanisms of photoinduced carriers separation and recombination for Fe<sup>3+</sup>-TiO<sub>2</sub> photocatalysts," *Appl. Surf. Sci.*, vol. 253, no. 9, pp. 4390–4395, 2007, doi: 10.1016/j.apsusc.2006.09.049.
- [48] R. W. Matthews and S. R. McEvoy, "Photocatalytic degradation of phenol in the presence of near-UV illuminated titanium dioxide," *J. Photochem. Photobiol. A Chem.*, vol. 64, no. 2, pp. 231–246, 1992, doi: 10.1016/1010-6030(92)85110-G.

- [49] K. Dai, T. Peng, H. Chen, J. Liu, and L. Zan, "Photocatalytic degradation of commercial phoxim over la-doped TiO<sub>2</sub> nanoparticles in aqueous suspension," *Environ. Sci. Technol.*, vol. 43, pp. 1540–1545, 2009, doi: 10.1021/es802724q.
- [50] K. Dai, T. Peng, H. Chen, R. Zhang, and Y. Zhang, "Photocatalytic degradation and mineralization of commercial methamidophos in aqueous titania suspension," *Environ. Sci. Technol.*, vol. 42, pp. 1505–1510, 2008, doi: 10.1021/es702268p.
- [51] R. Ali and S. H. Hassan, "Degradation Studies on Paraquat and Malathion Using TiO<sub>2</sub>/ ZnO Based Photocatalyst," *Malaysian J. Anal. Sci.*, vol. 12, no. 1, pp. 77–87, 2008.
- [52] H. Yoshida *et al.*, "Hydrogen production from methane and water on platinum loaded titanium oxide photocatalysts," *J. Phys. Chem. C*, vol. 112, no. 14, pp. 5542–5551, 2008, doi: 10.1021/jp077314u.
- [53] B. Seger and P. V. Kamat, "Fuel cell geared in reverse: Photocatalytic hydrogen production using a TiO<sub>2</sub>/Nafion/Pt membrane assembly with no applied bias," *J. Phys. Chem. C*, vol. 113, pp. 18946–18952, 2009, doi: 10.1021/jp907367k.
- [54] K. Fujihara, T. Ohno, and M. Matsumura, "Splitting of water by electrochemical combination of two photocatalytic reactions on TiO<sub>2</sub> particles," *J. Chem. Soc. - Faraday Trans.*, vol. 94, no. 24, pp. 3705–3709, 1998, doi: 10.1039/a806398b.
- [55] C. V. Jagtap, V. S. Kadam, M. A. Mahadik, J. S. Jang, N. B. Chaure, and H. M. Pathan, "Effect of Binder Concentration and Dye Loading Time on Titania Based Photoanode in Dye Sensitized Solar Cell Application," *Eng. Sci.*, vol. 17, pp. 133–141, 2022, doi: 10.30919/es8d581.
- [56] A. AliQureshi, H. Muhammad, A. Javed, and S. Javed, "Incorporation of Zr-doped TiO<sub>2</sub> nanoparticles in electron transport layer for efficient planar perovskite solar cells," *Surfaces and Interfaces*, vol. 25, no. 101299, 2021, doi: <https://doi.org/10.1016/j.surfin.2021.101299>.
- [57] C. V. Jagtap, V. S. Kadam, S. R. Jadkar, and H. M. Pathan, "Performance of N3 Sensitized Titania Solar Cell under Artificial Light Ambience," *ES Energy Environ.*, vol. 3, pp. 60–67, 2019, doi: 10.30919/ese8c220.

- [58] A. E. Shalan, M. M. Rashad, Y. Yu, M. Lira-Cantú, and M. S. A. Abdel-Mottaleb, "Controlling the microstructure and properties of titania nanopowders for high efficiency dye sensitized solar cells," *Electrochim. Acta*, vol. 89, pp. 469–478, 2013, doi: 10.1016/j.electacta.2012.11.091.
- [59] M. Yeoh, "Recent advances in photo-anode for dye-sensitized solar cells : a review," 2017, doi: 10.1002/er.3764.
- [60] W. Quizzes, R. Links, H. G. Photovoltaic, A. Advanced, and B. Principles, "Performance Analysis of Calcium-Doped Titania (TiO<sub>2</sub>) as an Effective Electron Transport Layer (ETL) for Perovskite Solar Cells," *Energies*, vol. 15, no. 1408, pp. 1–15, 2022, doi: <https://www.mdpi.com/1996-1073/15/4/1408>.
- [61] E. J. Juarez-Perez *et al.*, "Role of the selective contacts in the performance of lead halide perovskite solar cells," *J. Phys. Chem. Lett.*, vol. 5, no. 4, pp. 680–685, 2014, doi: 10.1021/jz500059v.
- [62] J. Liu, D. Choi, Z. Yang, and D. Wang, "Lithium ion batteries with titania/graphene anodes," US8450014B2, 2013.
- [63] M. J. Gázquez, J. P. Bolívar, R. Garcia-tenorio, and F. Vaca, "A Review of the Production Cycle of Titanium Dioxide Pigment," *Mater. Sci. Appl.*, vol. 5, pp. 441–458, 2014, doi: <http://dx.doi.org/10.4236/msa.2014.57048>.
- [64] X. Wang *et al.*, "Microwave-Absorbing of Carbothermic Reduced Products of Ilmenite and Oxidized Ilmenite," *J. Microw. Power Electromagn. Energy*, vol. 48, no. 3, pp. 192–202, 2014, doi: 10.1080/08327823.2014.11689883.
- [65] H. Run, L. Pengsheng, Y. Yuehui, and Z. Jinzhu, "Vacuum Carbothermic Reduction of Panzhihua Ilmenite Concentrate: A Thermodynamic Study," *Miner. Process. Extr. Metall. Rev.*, vol. 38, pp. 193–198, 2017, doi: 10.1080/08827508.2017.1281129.
- [66] Q. Zhu, J. Zhang, and H. Li, "Influence of phase and microstructure on the rate of hydrochloric acid leaching in pretreated Panzhihua ilmenite," *Particuology*, vol. 14, pp. 83–90, 2014, doi: 10.1016/j.partic.2013.08.002.
- [67] M. K. Sarker, A. K. M. B. Rashid, and A. S. W. Kurny, "Kinetics of leaching of

- oxidized and reduced ilmenite in dilute hydrochloric acid solutions,” *Int. J. Miner. Process.*, vol. 80, no. 2–4, pp. 223–228, Sep. 2006, doi: 10.1016/j.minpro.2006.04.005.
- [68] L. Zhang, H. Hu, Z. Liao, Q. Chen, and J. Tan, “Hydrochloric acid leaching behavior of different treated Panxi ilmenite concentrations,” *Hydrometallurgy*, vol. 107, no. 1–2, pp. 40–47, 2011, doi: 10.1016/j.hydromet.2011.01.006.
- [69] L. Wei, H. Hu, Q. Chen, and J. Tan, “Effects of mechanical activation on the HCl leaching behavior of plagioclase, ilmenite and their mixtures,” *Hydrometallurgy*, vol. 99, pp. 39–44, 2009, doi: 10.1016/j.hydromet.2009.06.003.
- [70] V. Shojaei, M. Schaffie, A. Mohebbi, and M. Ranjbar, “Upgrading of ilmenite using KOH sub-molten salt process assisted by mechanical activation,” *Mater. Manuf. Process.*, vol. 29, no. 10, pp. 1284–1288, 2014, doi: 10.1080/10426914.2014.941485.
- [71] C. Li, B. Liang, H. Song, J. qiang Xu, and X. qing Wang, “Preparation of porous rutile titania from ilmenite by mechanical activation and subsequent sulfuric acid leaching,” *Microporous Mesoporous Mater.*, vol. 115, pp. 293–300, 2008, doi: 10.1016/j.micromeso.2008.01.045.
- [72] C. Li, B. Liang, and H. Y. Wang, “Preparation of synthetic rutile by hydrochloric acid leaching of mechanically activated Panzhihua ilmenite,” *Hydrometallurgy*, vol. 91, pp. 121–129, 2008, doi: 10.1016/j.hydromet.2007.11.013.
- [73] C. Sasikumar, D. S. Rao, S. Srikanth, N. K. Mukhopadhyay, and S. P. Mehrotra, “Dissolution studies of mechanically activated Manavalakurichi ilmenite with HCl and H<sub>2</sub>SO<sub>4</sub>,” *Hydrometallurgy*, vol. 88, pp. 154–169, 2007, doi: 10.1016/j.hydromet.2007.03.013.
- [74] A. A. Baba, S. Swaroopa, M. K. Ghosh, and F. A. Adekola, “Mineralogical characterization and leaching behavior of Nigerian ilmenite ore,” *Trans. Nonferrous Met. Soc. China (English Ed.)*, vol. 23, no. 9, pp. 2743–2750, 2013, doi: 10.1016/S1003-6326(13)62792-2.
- [75] A. V. Dubenko, M. V. Nikolenko, A. Kostyniuk, and B. Likozar, “Sulfuric acid

- leaching of altered ilmenite using thermal, mechanical and chemical activation,” *Minerals*, vol. 10, no. 6, pp. 1–21, 2020, doi: 10.3390/min10060538.
- [76] W. Liu *et al.*, “Preparation of synthetic rutile via selective sulfation of ilmenite with (NH<sub>4</sub>)<sub>2</sub>SO<sub>4</sub> followed by targeted removal of impurities,” *Chinese J. Chem. Eng.*, vol. 25, no. 6, pp. 821–828, 2016, doi: 10.1016/j.cjche.2016.10.007.
- [77] P. C. Pistorius, “Ilmenite smelting: The basics,” *J. South. African Inst. Min. Metall.*, vol. 108, no. 1, pp. 35–43, 2008.
- [78] R. Subagja and A. Royani, “Titanium dissolution from decomposed Ilmenite using NaOH into the aqueous sulphuric acid solutions,” in *IOP Conference Series: Materials Science and Engineering*, 2019, vol. 541, p. 1, doi: 10.1088/1757-899X/541/1/012041.
- [79] B. Liang, C. Li, C. Zhang, and Y. Zhang, “Leaching kinetics of Panzhihua ilmenite in sulfuric acid,” *Hydrometallurgy*, vol. 76, no. 3–4, pp. 173–179, 2005, doi: 10.1016/j.hydromet.2004.10.006.
- [80] C. Li, B. Liang, and L. hong Guo, “Dissolution of mechanically activated Panzhihua ilmenites in dilute solutions of sulphuric acid,” *Hydrometallurgy*, vol. 89, no. 1–2, pp. 1–10, 2007, doi: 10.1016/j.hydromet.2007.04.002.
- [81] Y. Guo, S. Liu, T. Jiang, G. Qiu, and F. Chen, “A process for producing synthetic rutile from Panzhihua titanium slag,” *Hydrometallurgy*, vol. 147–148, pp. 134–141, 2014, doi: 10.1016/j.hydromet.2014.05.009.
- [82] L. Jia *et al.*, “Beneficiation of titania by sulfuric acid pressure leaching of Panzhihua ilmenite,” *Hydrometallurgy*, vol. 150, pp. 92–98, 2014, doi: 10.1016/j.hydromet.2014.09.016.
- [83] X. Xiong, Z. Wang, F. Wu, X. Li, and H. Guo, “Preparation of TiO<sub>2</sub> from ilmenite using sulfuric acid decomposition of the titania residue combined with separation of Fe<sup>3+</sup> with EDTA during hydrolysis,” *Adv. Powder Technol.*, vol. 24, pp. 60–67, 2013, doi: 10.1016/j.appt.2012.02.002.
- [84] Z. Li, Z. Wang, and G. Li, “Preparation of nano-titanium dioxide from ilmenite using sulfuric acid-decomposition by liquid phase method,” *Powder Technol.*,



- vol. 287, pp. 256–263, 2016, doi: 10.1016/j.powtec.2015.09.008.
- [85] A. M. Ramadan, M. Farghaly, W. M. Fathy, and M. M. Ahmed, “Leaching and Kinetics Studies on Processing of Abu-Ghalaga Ilmenite Ore,” *Int. Res. J. Eng. Technol.*, vol. 3, no. 10, pp. 46–53, 2016.
- [86] J. P. Van Dyk, N. M. Vegter, and P. C. Pistorius, “Kinetics of ilmenite dissolution in hydrochloric acid,” *Hydrometallurgy*, vol. 65, no. 1, pp. 31–36, 2002, doi: 10.1016/S0304-386X(02)00063-4.
- [87] E. A. Walpole and D. Winter, “The Austpac ERMS and EARS Processes for the Manufacture of High-Grade Synthetic Rutile by the Hydrochloric Acid Leaching of Ilmenite,” in *International Conference on the Practice and Theory of Chloride/Metal Interaction*, 2000, no. October 2002, pp. 1–14.
- [88] T. Xue, L. Wang, T. Qi, J. Chu, J. Qu, and C. Liu, “Decomposition kinetics of titanium slag in sodium hydroxide system,” *Hydrometallurgy*, vol. 95, no. 1–2, pp. 22–27, 2009, doi: 10.1016/j.hydromet.2008.04.004.
- [89] Y. Zhang, T. Qi, and Y. Zhang, “A novel preparation of titanium dioxide from titanium slag,” *Hydrometallurgy*, vol. 96, no. 1–2, pp. 52–56, 2009, doi: 10.1016/j.hydromet.2008.08.002.
- [90] Y. Liu, T. Qi, J. Chu, Q. Tong, and Y. Zhang, “Decomposition of ilmenite by concentrated KOH solution under atmospheric pressure,” *Int. J. Miner. Process.*, vol. 81, pp. 79–84, 2006, doi: 10.1016/j.minpro.2006.07.003.
- [91] T. A. Lasheen, “Soda ash roasting of titania slag product from Rosetta ilmenite,” *Hydrometallurgy*, vol. 93, pp. 124–128, 2008, doi: 10.1016/j.hydromet.2008.02.020.
- [92] S. Middlemas, Z. Z. Fang, and P. Fan, “A new method for production of titanium dioxide pigment,” *Hydrometallurgy*, vol. 131–132, pp. 107–113, 2013, doi: 10.1016/j.hydromet.2012.11.002.
- [93] L. Wu *et al.*, “A novel process for producing synthetic rutile and LiFePO<sub>4</sub> cathode material from ilmenite,” *J. Alloys Compd.*, vol. 506, pp. 271–278, 2010, doi: 10.1016/j.jallcom.2010.07.003.

- [94] A. Mehdilo and M. Irannajad, "Iron removing from titanium slag for synthetic rutile production," *Physicochem. Probl. Miner. Process.*, vol. 48, no. 2, pp. 425–439, 2012, doi: 10.5277/ppmp120209.
- [95] M. H. H. Mahmoud, A. A. I. Afifi, and I. A. Ibrahim, "Reductive leaching of ilmenite ore in hydrochloric acid for preparation of synthetic rutile," *Hydrometallurgy*, vol. 73, no. 1–2, pp. 99–109, 2004, doi: 10.1016/j.hydromet.2003.08.001.
- [96] T. A. I. Lasheen, "Chemical beneficiation of Rosetta ilmenite by direct reduction leaching," *Hydrometallurgy*, vol. 76, pp. 123–129, 2005, doi: 10.1016/j.hydromet.2004.10.002.
- [97] A. Berni, M. Mennig, and H. Schmidt, "Doctor Blade," in *Sol-Gel Technologies for Glass Producers and Users*, M. A. et al. Aegerter, Ed. Springer Science+Business Media New York, 2004, pp. 89–92.
- [98] D. Kuscer, "Screen printing," in *Encyclopedia of Materials: Technical Ceramics and Glasses*, Elsevier Ltd, 2020.
- [99] A. Power *et al.*, "Dye-Sensitized Solar Cells Employing a," *ACS Nano*, vol. 4, no. 8, pp. 4420–4425, 2010.
- [100] F. Xu, K. Zhu, and Y. Zhao, "The layer boundary effect on multi-layer mesoporous TiO<sub>2</sub> film based dye sensitized solar cells," *RSC Adv.*, vol. 6, pp. 98167–98170, 2016, doi: 10.1039/c6ra18830c.
- [101] J. G. Lee, J. H. Cheon, H. S. Yang, D. K. Lee, and J. H. Kim, "Enhancement of photovoltaic performance in dye-sensitized solar cells with the spin-coated TiO<sub>2</sub> blocking layer," *J. Nanosci. Nanotechnol.*, vol. 12, pp. 6026–6030, 2012, doi: 10.1166/jnn.2012.6410.
- [102] B. Grzmil, B. Kic, and M. Rabe, "Inhibition of the Anatase — Rutile Phase Transformation with Addition of K<sub>2</sub>O, P<sub>2</sub>O<sub>5</sub>, and Li<sub>2</sub>O," *Chem. Pap.*, vol. 58, no. 6, pp. 410–414, 2004.
- [103] J. Zhang, M. Li, Z. Feng, J. Chen, and C. Li, "UV raman spectroscopic study on TiO<sub>2</sub>- I. phase transformation at the surface and in the bulk," *J. Phys. Chem. B*,

- vol. 110, no. 2, pp. 927–935, 2006, doi: 10.1021/jp0552473.
- [104] N. N. Ilkhechi, A. R. Aghjehkohal, E. F. TanourAghaj, and M. Mozammel, “Enhanced optical and hydrophilic properties of Si and Cd co-doped TiO<sub>2</sub> thin films,” *J. Mater. Sci. Mater. Electron.*, vol. 28, no. 6, pp. 4598–4605, 2016, doi: 10.1007/s10854-016-6097-6.
- [105] B. K. Kaleji and N. Hosseinabadi, “Enhanced photoinduced super-hydrophilicity in sol-gel TiO<sub>2</sub> thin films with co-doped Sn/Nb,” *J. Sol-Gel Sci. Technol.*, vol. 69, no. 2, pp. 412–417, 2014, doi: 10.1007/s10971-013-3235-y.
- [106] U. Diebold, “Structure and properties of TiO<sub>2</sub> surfaces: A brief review,” *Appl. Phys. A Mater. Sci. Process.*, vol. 76, no. 5, pp. 681–687, 2003, doi: 10.1007/s00339-002-2004-5.
- [107] N. S. Lewis *et al.*, “Basic Research Needs for Solar Energy Utilization: Report of the Basic Energy Sciences Workshop on Solar Energy Utilization,” United States, 2005. doi: <https://doi.org/10.2172/899136>.
- [108] P. Niu, T. Wu, L. Wen, J. Tan, Y. Yang, and S. Zheng, “Substitutional Carbon-Modified Anatase TiO<sub>2</sub> Decahedral Plates Directly Derived from Titanium Oxalate Crystals via Topotactic Transition,” *Adv. Mater.*, vol. 30, no. 20, p. e1705999, 2018, doi: <https://doi.org/10.1002/adma.201705999>.
- [109] R. Asahi, T. Morikawa, H. Irie, and T. Ohwaki, “Nitrogen-Doped Titanium Dioxide as Visible-Light-Sensitive Photocatalyst: Designs, Developments, and Prospects,” *Chem. Rev.*, vol. 114, no. 19, pp. 9824–9852, 2014, doi: <https://doi.org/10.1021/cr5000738>.
- [110] J. Choi, H. Park, and M. R. Hoffmann, “Effects of Single Metal-Ion Doping on the Visible-Light Photoreactivity of TiO<sub>2</sub>,” *J. Phys. Chem. C*, vol. 114, no. 2, pp. 783–792, 2010, doi: <https://doi.org/10.1021/jp908088x>.
- [111] H. Song, C. Li, Z. Lou, Z. Ye, and L. Zhu, “Effective Formation of Oxygen Vacancies in Black TiO<sub>2</sub> Nanostructures with Efficient Solar-Driven Water Splitting,” *ACS Sustain. Chem. Eng.*, vol. 5, no. 10, pp. 8982–8987, 2017, doi: <https://doi.org/10.1021/acssuschemeng.7b01774>.

- [112] W. Zhang, Z. Zhu, and C. Y. Cheng, "Hydrometallurgy A literature review of titanium metallurgical processes," *Hydrometallurgy*, vol. 108, no. 3–4, pp. 177–188, 2011, doi: 10.1016/j.hydromet.2011.04.005.
- [113] A. Michel-Lévy and A. Lacroix, *Les Minéraux des Roches*. Librairie Polytechnique Paris, 1888.
- [114] M. A. Mange and H. F.W. Maurer, *Heavy minerals in colour.*, 1st ed. Chapman & Hall, 1992.
- [115] B. . Warren, *X-Ray Diffraction*. New York: Dover Publications Inc, 1990.
- [116] S. Sen, S. K. Halder, and G. S. P. Sen, "An X-Ray Line Broadening Analysis in the Vacuum-Evaporated Silver Films," *J. Phys. Soc. Japan*, vol. 38, no. 6, pp. 1641–1647, 1975, doi: 10.1143/JPSJ.38.1641.
- [117] C. S. Nehru, L .C., V. Swaminathan, "Photoluminescence Studies on Nanocrystalline Tin Oxide Powder for Optoelectronic Device," *J. Mater. Sci.*, vol. 2, no. 2, pp. 6–10, 2006.
- [118] J. Tauc, R. Grigorovici, and A. Vancu, "Optical Properties and Electronic Structure of Amorphous Germanium," *Phys. Status Solidi B.*, vol. 15, pp. 627–637, 1966, doi: 10.1002/9781118437865.ch16.
- [119] J. I. Pankove, *Optical Processes in Semiconductors*. Courier Corporation, 1971.
- [120] P. . Kubelka and F. Munk, "A Contribution to the Optics of Pigments," *Z. Technol. Phys*, vol. 12, pp. 593–599, 1931.
- [121] P. Makuła, M. Pacia, and W. Macyk, "How To Correctly Determine the Band Gap Energy of Modified Semiconductor Photocatalysts Based on UV-Vis Spectra," *J. Phys. Chem. Lett.*, vol. 9, pp. 6814–6817, 2018, doi: 10.1021/acs.jpcclett.8b02892.
- [122] R. Zhang, A. A. Elzatahry, S. S. Al-Deyab, and D. Zhao, "Mesoporous titania: From synthesis to application," *Nano Today*, vol. 7, pp. 344–366, 2012, doi: 10.1016/j.nantod.2012.06.012.
- [123] T. Ohno, ã. T. Mitsui, and M. Matsumura, "Photocatalytic Activity of S-doped TiO<sub>2</sub> Photocatalyst under Visible Light," *Chem. Lett.*, vol. 32, no. 4, pp. 364–

365, 2003, doi: <https://doi.org/10.1246/cl.2003.364>.

- [124] A. Kompa, C. U. D. Kekuda, and M. Rao K, “Investigation on structural, optical and electrical properties of Nd doped titania films and application of optical model,” *Mater. Sci. Semicond. Process.*, vol. 121, no. March 2020, pp. 1–8, 2021, doi: 10.1016/j.mssp.2020.105293.
- [125] T. Archana, K. Vijayakumar, M. Arivanandhan, and R. Jayavel, “TiO<sub>2</sub> nanostructures with controlled morphology for improved electrical properties of photoanodes and quantum dot sensitized solar cell characteristics,” *Surfaces and Interfaces*, vol. 17, no. July, pp. 3–11, 2019, doi: 10.1016/j.surfin.2019.100350.
- [126] R. Bel Hadj Tahar, T. Ban, Y. Ohya, and Y. Takahashi, “Tin doped indium oxide thin films: Electrical properties,” *J. Appl. Phys.*, vol. 83, no. 5, pp. 2631–2645, 1998, doi: 10.1063/1.367025.